

# **Counterion Distribution around a Macroion in Polyelectrolytes Probed by Anomalous Small- Angle X-Ray Scattering**

DISSERTATION

zur Erlangung des akademischen Grades eines

Doktors der Naturwissenschaften (Dr. rer. nat.)

in Fach Chemie der Fakultät für Biologie, Chemie und Geowissenschaften

der Universität Bayreuth

vorgelegt von

**Mushtaq Patel**

Aus Pune, Indien

Bayreuth, 2005

Die vorliegende Arbeit wurde in der Zeit von Januar 2001 bis November 2003 am Polymer-Institut der Universität Karlsruhe(TH) durchgeführt und von Dezember 2003 bis Dezember 2004 am Lehrstuhl für Physikalische Chemie I der Universität Bayreuth fortgesetzt.

Vollständiger Abdruck der von der Fakultät für Biologie, Chemie und Geowissenschaften der Universität Bayreuth genehmigten Dissertation zur Erlangung des akademischen Grades eines Doktors der Naturwissenschaften (Dr. rer. nat.)

Dissertation eingereicht am: 08.04.2005

Wissenschaftliches Kolloquium am: 12.07.2005

Prüfungsausschuß

Prof. Dr. M. Ballauff (Erstgutachter)

Prof. Dr. J. Senker (Zweitgutachter)

Prof. Dr. A. H. E. Müller

Prof. Dr. K. Seifert (Vorsitzender)

Dekan: Prof. Dr. O. Meyer

## **Acknowledgements**

I take this opportunity to thank Prof. Dr. Matthias Ballauff, for providing me with an interesting theme for my Ph.D thesis and for his valuable guidance and constant encouragement.

I would like to express my gratitude to Dr. Nico Dingenouts for his immense help in introducing me to the field of small angle x-ray scattering and the numerous fruitful scientific discussions in the interpretation of the scattering data.

I would like to specially thank my colleagues Dr. Sabine Rosenfeldt and Dr. Diego Pontoni, for helping me in the acquisition of the scattering data at the ESRF, Grenoble. Special thanks are also due to Dr. T. Narayanan, who has been of immense help at the ESRF, Grenoble.

I would also like to specially thank Dr. Horwath for the fruitful discussions. Special thanks are also due to Dr. Jürgen Blaul, who guided me in the synthesis of rod-like polyelectrolytes. His great experience in this field helped me a lot.

My sincere thanks are due to Dr. Xuhong Guo for providing the samples of spherical polyelectrolyte brushes and Mr. Felix Plamper for providing the samples of star-shaped polyelectrolytes for SAXS studies.

I am also thankful to my colleagues Dr. Alexander Wittemann, Dr. Arben Jusufi, Björn Haupt, Yu Mei, Li Li, Jerome Crassous and all the other colleagues for their kind cooperation and lively working atmosphere during my Ph.D work.

I would take this opportunity to thank Ms. Manuela Winkler, Ms. Ilona Deger, Ms. Ute Meyer and Ms. Christine Thunig for helping me with the paperwork required during my stay in Germany.

My thanks are also due to Mr. Wolfgang Arbogast, Mr. Hans Kühn, Ms. Helena Hörig, Mr. Karl Heinz Lauterbach and Ms. Christa Bächer for their technical help in daily lab work. Special thanks are also due to Geeta Sharma for careful reading of this thesis and the numerous scientific arguments.

I express my gratitude to my family and friends for their constant moral support during the course of my Ph.D work.



# Table of Contents

<b>1 Introduction .....</b>	<b>1</b>
1.1 Rod-like Polyelectrolytes .....	3
1.2 Spherical Polyelectrolyte Brushes.....	5
1.3 Star-shaped Polyelectrolytes .....	8
<b>2 Theory .....</b>	<b>11</b>
2.1 Osmotic Pressure.....	11
2.2 Osmotic Coefficient .....	14
2.3 Counterion Condensation .....	16
2.4 Poisson-Boltzmann Equation for Salt Free Polyelectrolyte Solutions.....	18
2.5 Small Angle X-Ray Scattering.....	24
2.5.1 Introduction.....	24
2.5.2 Scattering Theory .....	25
2.5.3 Scattering Intensity .....	28
2.5.4 Moving Particles.....	31
2.5.5 Radius of Gyration .....	33
2.5.6 Contrast.....	34
2.6 Scattering by Particles .....	36
2.6.1 Particles with radial symmetry (Spheres) .....	36
2.6.2 Particles with cylindrical geometry (Rod-like particles) .....	38
2.7 Anomalous Small Angle X-ray Scattering (ASAXS).....	40
<b>3 Measurements and Analysis .....</b>	<b>44</b>
3.1 Rod-Like Polyelectrolytes .....	44
3.1.1 Data Treatment.....	44
3.1.2 Background Subtraction .....	45
3.2 Spherical Polyelectrolyte Brushes.....	46
3.2.1 Data Treatment.....	46
3.2.2 Background Subtraction .....	46
3.2.3 Desmearing .....	48
3.2.4 Setting together the 2m and 10m scattering intensities .....	49
3.2.5 Fluorescence Subtraction .....	50

3.2.6 Edge Localization.....	53
3.2.7 Effective scattering factors $f'_{eff}$ and $f''_{eff}$ .....	54
<b>4 Results and Discussion .....</b>	<b>55</b>
4.1 Rod-like Polyelectrolytes .....	55
4.1.1 Osmotic Coefficient of Rod-like Polyelectrolytes .....	57
4.2 Anomalous Small Angle X-ray Scattering (ASAXS).....	61
4.2.1 Rod-like Polyelectrolytes.....	61
4.2.2 Comparison with the Poisson-Boltzmann Cell Model .....	71
4.3 ASAXS Studies of Spherical Polyelectrolyte Brushes.....	73
4.3.1 Contrast of macroion .....	74
4.3.2 Complex contrast of counterions.....	74
4.3.3 Calculation of $I_0(q)$ and of $v(q)$ .....	75
4.3.4 Model calculation .....	76
4.3.5 ASAXS Results for Spherical Polyelectrolyte Brushes .....	78
4.4 Effect of pH on Polyelectrolyte Brushes .....	83
4.5 Star-Shaped Polyelectrolytes .....	85
4.5.1 SAXS Studies of Star-shaped Polyelectrolytes.....	85
4.5.2 ASAXS Studies of Star-shaped Polyelectrolytes .....	91
<b>5 Summary .....</b>	<b>96</b>
<b>5 Zusammenfassung.....</b>	<b>98</b>
<b>6 References .....</b>	<b>100</b>
<b>Appendix .....</b>	<b>107</b>
<b>7 Synthesis .....</b>	<b>107</b>
7.1 Synthesis of Rod-like Polyelectrolytes.....	107
7.2 Polymerization .....	114
7.2.1 Synthesis of Polymer Precursor .....	114
7.2.2 Characterisation of the Precursor .....	116
7.3 Polyelectrolyte Synthesis.....	116
7.3.1 Deprotection of the Ether Groups .....	116
7.3.2 Synthesis of Polyelectrolyte.....	117
7.3.3 Sample Preparation for Osmotic Coefficient Measurements.....	119

7.4 Synthesis of Spherical Polyelectrolyte Brushes.....	120
7.5 Synthesis of Star Polyelectrolytes.....	121
<b>8 Experimental Section.....</b>	<b>122</b>
8.1 Membrane Osmometer.....	122
8.2 Calibration of Osmometer.....	122
8.3 Density Measurements.....	123
8.4 Anomalous Small Angle X-ray Scattering (ASAXS).....	124





## **1 Introduction**

Polyelectrolytes are charged macromolecules, which in the presence of polar solvents dissociate completely into a 'macro ion' or 'polyions' and counterions. The charge on these polyions is neutralised by an equivalent number of oppositely charged 'counter ions' which are present in the neighbourhood of the macro ion. Polyelectrolytes are often classified depending on their nature as natural macromolecules or synthetic macromolecules. They are also classified depending on electrochemical properties such as polyacids or polybases. A special group of polyelectrolytes carrying both negative and positive charges are known as 'polyampholytes' (e.g., proteins, nucleic acids, polysaccharides). Polyelectrolytes are also distinguished depending upon their conformations such as flexible, rod-like etc. Flexible polyelectrolytes i.e., polyelectrolytes bearing a macro ion which can undergo conformational changes exhibit complex behaviour resulting from intramolecular forces as well as strong intermolecular electrostatic interactions. Since both these interactions occur almost simultaneously it is rather difficult to study these systems. Rigid rod-like polyelectrolytes i.e., those bearing a macro ion which does not undergo any conformational changes due to steric constraints on such systems. Only the intermolecular coulombic interactions determine the solution properties of these polyelectrolytes. There are many examples of biologically occurring rigid rod-like polyelectrolytes such as DNA, RNA and the Tobacco-mosaic virus.

Polyelectrolytes also find importance industrially in the field of paper-making, waste-water treatment, phase separation, super absorbers and as binders in tablets. The wide ranged applications of polyelectrolytes for industrial purpose combined with their presence in all forms of life have made them a great topic of interest.

As early as in 1938, experimental evidence was found to suggest that polyelectrolytes exhibit different thermodynamic properties as compared to the low molecular weight electrolytes [Kern et al.1938; Huizenga et al.1950]. The obvious challenge was therefore to develop a theory which would explain such behaviour of polyelectrolytes in polar solutions.

In the early 50's, researchers [Fuoss et al. 1951; Alfrey et al. 1951; Katchalsky 1951] calculated the analytical solution based on the Poisson-Boltzmann Cell Model in order to explain the thermodynamic properties of polyelectrolytes in solution. Manning later introduced the concept of 'counter ion condensation' which treats the counter ions to be in strong correlation with the macro ion in case of strong polyelectrolytes. [Manning 1965].

Later many models were developed by various researchers like the “worm-like chain” theory [Odijk 1977] for highly charged polyelectrolytes and the “blob” Model based on the scaling-concept for weak polyelectrolytes [*de Gennes* 1976].

During the past few decades, extensive research has been carried out in the field of polyelectrolytes and a number of studies have been performed on flexible polyelectrolytes such as polystyrene sulfonate, poly(diallyldimethyl-ammonium chloride) etc as well as on rod-like polyelectrolytes such as DNA [Okubu, Ise 1969; Mandel 1980; Mandel 1989; Mordmeier 1995; Kassapidou et al. 1997] or xanthanes [Sato et al. 1984; Gamini, Mandel 1994; Milas et al 1995; Berth et al 1996] and Tobacco-Mosaic Virus [Lauffer 1958; Maier et al. 1988,1992 ]. However, studies on DNA have been problematic largely due to their sensitivity towards temperature and ionic strength changes. DNA tends to lose its helical conformation at very low ionic strengths and high temperatures [Alexandrowicz et al. 1969].

Polyelectrolytes of varying architecture like spherical polyelectrolyte brushes and star-shaped polyelectrolytes are also of great interest. The counterions in such systems are mostly confined within the polyelectrolyte brushes. This property is very advantageous for various applications like, the adsorption of proteins [Witte mann et al. 2003], enzyme immobilization [Haupt et al. 2004] and the generation of metal nanoparticles [Sharma et al. 2004].

In the following thesis a systematic study of three different polyelectrolytes namely: Rigid rod-like polyelectrolytes, spherical polyelectrolyte brushes and star-shaped polyelectrolytes using Anomalous Small Angle X-ray Scattering (ASAXS) has been carried out. The experimental results obtained by ASAXS are compared with the theoretical predictions.

## 1.1 Rod-like Polyelectrolytes

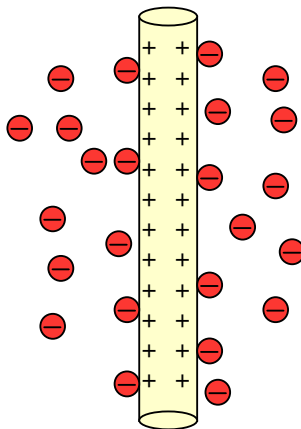


*Fig. 1.1 shows the schematic representation of a typical rigid rod-like polyelectrolyte. The macroion comprises of a stiff poly (*p*-phenylene) backbone having two *n*-hexyl spacer groups per monomer unit. Each of these side chains bears two charged groups with bromine counterions*

Rod-like polyelectrolytes are defined as polyelectrolytes which do not undergo in conformational changes depending on the ionic strength, pH etc., largely due to the steric constraints imposed by the chemical nature of such systems. Fig.1.1 demonstrates a schematic representation of rigid rod-like polyelectrolytes.

The first synthesis of rigid rod-like polyelectrolytes was reported based on poly [1,4-phenylbenzobisoxazoles] and poly [1,4-phenylenebenzobisthiazoles] [Berry et al. 1983]. In the last decade several researchers [Rehahn et al. 1993; Rehahn et al. 1996; Wegner et al. 1994; Wegner et al 1996] following different precursor routes developed rod-like poly[*p*-phenylene] PPP polyelectrolytes. The synthesis proceeds through a number of synthetic steps and finally via an aryl-aryl coupling Suzuki reaction yields the uncharged rod-like polymer with a rigid aryl backbone and two *n*-hexyl side chains per repeating unit. Subsequent reaction steps lead to the formation of rod-like polyelectrolytes. Each monomer has two or four ionic units attached to the *n*-hexyl side chains. Such PPP's are thermally as well as chemically stable and provide a convenient and efficient way to study rod-like polyelectrolytes in aqueous solutions.

Owing to their persistence length of approximately 21 nm [Galda 1994] PPP's provide an ideal system to be compared against the theoretical treatment of these rod-like polyelectrolytes. The most widely used theoretical model for the treatment of rod-like polyelectrolytes is based on the Cylindrical Cell Model [Fuoss et al. 1951]. The analytical solution of this model namely, the Poisson-Boltzmann Equation for salt-free solutions [Fuoss et al. 1951; Alfrey et al. 1951; Katchalsky 1971] is being widely applied to rod-like polyelectrolytes. This model treats the polyelectrolyte solution to be divided into cylinders whereby each cylinder corresponds to a single polyelectrolyte molecule placed in the centre of the cylinder surrounded by counter ions.

The concept of 'counter ion condensation' was put forth by Manning [Manning 1969]. According to this concept, when the ratio of electrostatic interactions between the macro ion and its counter ions is no longer small as compared to  $k_B T$  counter ions tend have a strong correlation with the macro ion such counter ions were termed as 'condensed' and the phenomenon termed as 'counter ion condensation'. [Manning 1969; Oosawa 1971; Le Bret, Zimm 1984].

Recently stiff chain polyelectrolytes were studied in the framework of PB-Cell model. The osmotic coefficient was experimentally measured and compared with the PB-theory [Blaul et al. 2001]. Although no information regarding the distribution of these counter ions can be obtained by this method. However, the osmotic coefficient provides valuable information about the number of counter ions present at the cell boundary. The distribution of stiff-chain polyelectrolytes was studied by scattering methods recently [Guillaume et al. 2001, 2002]. Recently Anomalous Small Angle X-Ray Scattering (ASAXS) studies were also carried out on DNA in aqueous solutions [Das et al. 2002].

Computer Simulations of rod-like polyelectrolytes seem to be in good agreement with the experimental results obtained for the osmotic coefficient of rigid rod-like polyelectrolytes. [Deserno et al. 2001]. In the course of this thesis, rod-like polyelectrolytes having a poly (p-phenylene) rigid backbone with two charge groups per monomer unit bearing bromine counterions were investigated using the Anomalous Small X-Ray Scattering method. As it is demonstrated in this thesis, ASAXS provides a very efficient tool in the investigation of the correlation of counterions to the macroion.

## 1.2 Spherical Polyelectrolyte Brushes

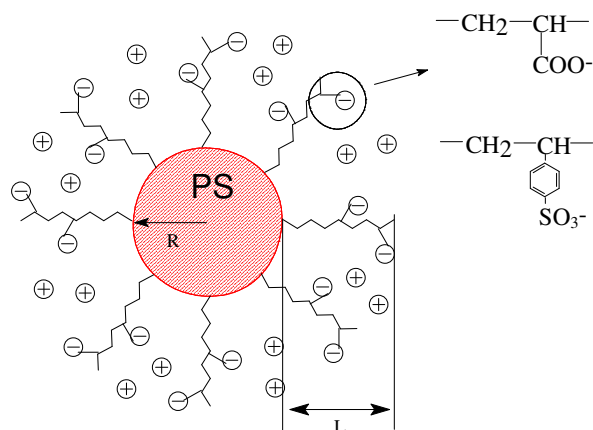


Fig. 1.2 shows the schematic representation of a spherical polyelectrolyte brush. The particles consist of a poly(styrene) core, onto which linear poly(acrylic acid) (PAA) are attached chemically. Since the distance between the chains on the surface of the core particle is much smaller than the linear dimensions of the poly(acrylic acid) chains. Therefore, the PAA chains for a spherical brush in which the counterions are confined.

Polyelectrolyte brushes are formed when linear polyelectrolytes are affixed on a surface either planar or curved. When polyelectrolytes are affixed on a spherical surface such systems are termed as Spherical Polyelectrolyte Brushes. A polyelectrolyte chain can be either 'grafted to' or 'grafted from' a substrate.

The radial structure of a brush-like polyelectrolyte is depicted schematically in Fig.1.2. Each composed of a polystyrene core and polyelectrolyte ( polyacrylic acid, polystyrene sulfonate etc.,) chains chemically grafted onto the core surface.

Spherical polyelectrolyte brushes have been prepared by adsorption of block copolymers on the surface of latex particles [Russel et al. 1997, 1998; Wesley et al. 2000] and by formation of micelles from suitable block copolymers [Eisenberg et al. 1996, 1999; Guenoun et al. 2000, 2001; Förster et al. 2002]. Micelles formed from block copolymers have recently been the subject of detailed studies employing neutron scattering [van der Maarel et al. 2000]. More recently SANS combined with electron microscopy and dynamic light scattering was also used to study micelles having a corona of polyelectrolyte chains [Förster et al. 2002].

Spherical polyelectrolyte brushes are distinguished in two types: annealed brushes and quenched brushes. Brushes which are made up of weakly ionizing groups as e.g. poly(acrylic acid) (PAA). The charge of such brushes depends on the local electrostatic conditions and the system is classified as annealed brush. On the other hand, grafting of strong polyelectrolyte chains to surfaces leads to quenched brushes in which the chains are charged under arbitrary conditions. When immersed in water or a polar solvent, such a brush is swollen. The degree of swelling along the layer results from a balance of the electrostatic repulsion that stretch the chains and the retracting force due to the configurational elasticity of the polymer chains [Fleer et al. 1993, Guenon et al. 2001; Pincus 1991]. Since the electrostatic repulsion can be tuned by added salt, the degree of swelling of polyelectrolyte brushes can be varied within a wide range.

Polyelectrolyte brushes have been the subject of a large number of theoretical studies recently [Pincus et al. 1991; Borisov et al. 1991, 1994, 1998; Zhulina et al. 1992, 1995, 1996, 1999, 2000; Muthukumar et al. 1995; Tirrell et al. 1992]. Two different regimes have been identified in the case of spherical polyelectrolyte brushes: If no salt is added the osmotic limit is reached where the osmotic pressure of the counterions leads to a strong stretching of the chains. Such a brush is termed as ‘osmotic brush’. At high concentrations of added salt, the electrostatic interaction is strongly screened. In this limit termed ‘salted brush’, the thickness of the brush is determined by the mutual interactions of the chains and the overall structure resembles to that of an uncharged system. The main predictions of theory compare favourably with the experimental data obtained from planar brushes and seem to be rather well-understood by now [Förster et al. 1997, 1998; Penfold et al. 1999; Rühle et al. 1999, 2002, 2004; Tran et al. 1999, 2001; Tamashiro et al. 2001].

Strongly curved polyelectrolyte brushes, however, are much less understood. These systems are generated by attaching polyelectrolyte chains to colloidal particles of radius  $R$ . Fig.1.2 displays schematically such a particle that consists of a solid polymer core and a shell of densely grafted polyelectrolyte chains. In the following thesis, these systems will be termed spherical polyelectrolyte brushes. If  $R$  exceeds the contour length  $L_c$  of the chains by far, the planar limit is recovered. If, on the other hand,  $R \ll L_c$ , such a spherical polyelectrolyte will resemble charged star polymers.

A most important question in the understanding of spherical polyelectrolyte brushes is the correlation of the counterions to the macroion. Recently, this problem has been studied theoretically for the case of polyelectrolyte stars [Jusufi et al. 2002]. In the course of this work it has been shown that the counterions can be subdivided into three classes: i) Counterions

which are condensed to the polyelectrolyte chains because of their strong electric charge ("Manning condensation") ii); counterions that are trapped within the brush but can move freely inside the brush, and iii) counterions that are free to move through the brush into the bulk system. Only the last fraction of the counterions leads to a measurable osmotic pressure. Very recently, this work has also been extended to include the spherical polyelectrolyte brushes under consideration here [Jusufi et al. 2004].

Spherical polyelectrolyte brushes (Fig.1.2) prepared by photo emulsion polymerization [Guo et al. 1999, 2000] present a nearly ideal model system to check these predictions. PAA-chains are grafted densely on a mono disperse solid poly(styrene) core having a diameter between 80 and 120 *nm*. The chains have been generated directly on the surface of the core particles by the photo initiated radical polymerization of the water-soluble monomer acrylic acid. The contour length  $L_c$  as well as the grafting density  $\sigma$  can be determined.

Up to now, these systems have been studied comprehensively by dynamic light scattering in highly diluted aqueous solutions as a function of *pH* and salinity [Guo et al. 2000, 2001] and by SAXS [de Robillard et al. 2000]. Dynamic light scattering gives the overall dimensions of the particles but gives no information on the location of the counterions. Osmometry of salt-free suspensions of the spherical polyelectrolyte brushes shows that the concentration of free counterions is of the order of a few percent only. Hence, the counterions are trapped within the brush to a large extend as predicted by the theory [Jusufi et al. 2002]. The aim of this thesis is to study the correlation of counterions in spherical polyelectrolyte brushes.

### 1.3 Star-shaped Polyelectrolytes

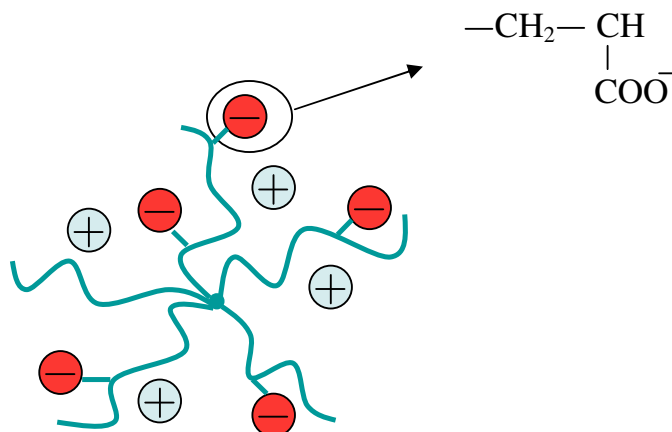


*Fig. 1.3 demonstrates the schematic representation of a star-shaped polyelectrolyte consisting of a very small core with linear polyelectrolyte chains attached chemically using the core-first technique. The number of arms attached can be varied depending on the initiator molecule.*

Star polymers are branched macromolecules bearing a small central core from where emerge several linear chains (charged or uncharged) [Marques et al. 1998]. Star polyelectrolytes differ from spherical polyelectrolyte brushes. Unlike brushes, where the core is of significant size and the linear chains are grafted on the surface, in the case of star-shaped polyelectrolytes the core is considerably small. Fig. 1.3 shows a schematic representation of a typical star-shaped polyelectrolyte. Due to the high segment density and the structure of star polymers, they have gained a lot of interest recently. Star polymers are interesting topic for theoretical studies and as discussed in the case of spherical polyelectrolyte brushes, the counterion correlation to the macroion has been a major topic of research [Jusufi et al. 2002, 2004]. Star polymers also have technical applications in lubricant additives and paints [Storey et al. 1997].

Star polymers are usually synthesized by using various living polymerization techniques. In the core-first technique, a multifunctional initiator is used and the number of arms depend on the initiator sites present [Matyjasewski 1996]. The other method is the arm-first technique in which first the arms of the polymer are synthesized first and then linked together employing a multifunctional linking agent [Hadjichristidis 1999]. The behaviour of star polymers is changed dramatically when converted to their corresponding polyelectrolytes.



According to theoretical predictions for quenched polyelectrolyte stars, most of the counterions are confined within the stars [Pincus 1991].

Borisov and Zhulina have used scaling theory and self-consistent field theory (SCF) to study stars, where a maxima is observed if the number of arms or the salt concentration is increased. The salt concentration where such a maxima appears was shown to be related to the internal charge density [Borisov et al. 2002]. Borisov et al. have also applied mean-field calculations for hetero-arms block copolymer micelles. Recently Molecular Dynamics (MD) simulations have also confirmed the extended nature of the polyelectrolyte chains in PE stars with the confinement of counterions [Jusufi et al. 2002].

Recently SAXS measurements carried out on star-shaped polyelectrolytes have shown some interesting results pertaining to the position of the peak related to the interstar structure factor. [Heinrich et al. 2001, Borsali et al. 2003]. In the case of polystyrene stars an ordering phenomenon was observed in the immediate vicinity of the overlap concentration  $c^*$ . Moreover it was also found that the degree of ordering was not maximum at  $c^*$  but actually increased as the concentration decreased. In case of scattering experiments such ordering gives rise to a maxima at any scattering vector  $q^*$ . This maxima corresponds to a position vector for many-arm stars and the inter-star distance can be determined through  $d = \frac{2\pi}{q^*}$ .

This maximum at  $q^*$  scales with the polymer concentration  $C_p^{1/2}$  in the semi-dilute regime and as  $C_p^{1/3}$  in the dilute regime. Long range electrostatic interactions impose a preferential distance between the charged particles that leads to a certain degree of ordering. This ordering is of a cubic arrangement in the dilute regime and a cylindrical or hexagonal packing in the semi dilute regime. While in the case of added salt, the maxima tends to vanish with increasing salt concentration due to the screening of the electrostatic interactions [Borsali et al. 2003]. In the case of aqueous solutions of sodium polystyrene sulfonate (NaPSS) star polyelectrolytes unusual scattering patterns were observed similar to the broad scattering peak seen in the case of semidilute solutions of NaPSS linear polyelectrolytes. These scattering patterns are related to the electrostatic correlation hole [Heinrich et al 2001]. In the dilute regime, where ( $\phi < \phi^*$ ) only the intramolecular repulsions play a significant role. As the concentration is increased gradually to semi-dilute regime ( $\phi > \phi^*$ ), the intermolecular repulsion between the stars also become quite significant giving rise to the interpenetration of stars. So as the concentration increases the size of the stars is also expected to decrease. This ordering phenomenon is known to be related to  $f$  linear chains attached to a comparably small core.

Functional PEO stars investigated using SAXS for ( $f > 72$ ) formed a bcc structure near the overlap concentration and charged PEO stars ( $f > 37$ ) formed a bcc lattice below the overlap concentration. The nearest-neighbor distance of the spheres decreased with an exponential function with increasing polymer concentration [Ishizu et al. 2003].

Ordered packing arrangements in the case of diblock copolymer micelles has already been studied [Thomas et al. 1986; McConnell et al. 1995]. Recently SANS was also used to study the osmotic brushes [Guenoun et al. 1998]. SANS studies from a single arm labelled polybutadiene star polymers in dilute solutions have shown that the radius of gyration has a dependence on star functionality [Hutchings et al. 2001] in agreement with the predictions of Daoud and Cotton. The aim of this work is to study the star-shaped polyelectrolytes with the help of SAXS and ASAXS and compare the experimental results with the theoretical predictions.

## 2 Theory

### 2.1 Osmotic Pressure

The osmotic pressure is a colligative property. When a pure solvent (water) and a solution are separated through a semi permeable membrane which allows the solvent molecules to pass but prevent the solute molecules (polymer molecules). The different concentrations on the two sides of the membrane tend to cause an initial difference in chemical potential. At equilibrium this difference in potential is compensated by an effective pressure across the membrane. As shown in Fig. 2.1 the solvent molecules pass from the chamber containing pure solvent to the solution chamber. At equilibrium the chemical potential in the solution becomes equal to the chemical potential of the pure solvent. The excess height in the column of liquid above the solution side is known as the osmotic pressure and can be written as  $\Pi = \rho g \Delta h$ , where  $\Pi$  is the osmotic pressure,  $\rho$  is the density of the solution,  $h$  is the height of the column of liquid and  $g$  is ( $9.81 \text{ m/sec}^2$ ).

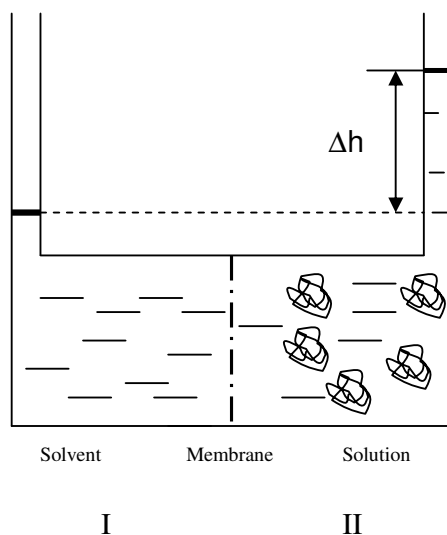


Fig. 2.1 shows a scheme of a typical osmosis cell where the solvent (Compartment I) and solution (Compartment II) are separated through a semi-permeable membrane which restricts the flow of the solute, but allows only the solvent to pass through it.

On the side of the pure solvent, where the pressure is  $p$ , the chemical potential is given as  $\mu_A^0(p)$ . On the solution side, the chemical potential is lowered due to the presence of the solute (polymer) which reduces the mole fraction of the solvent from 1 to  $X_A$ , where  $X_A$  is the mole fraction of the solution. However, the chemical potential of A is raised due to a greater pressure  $p + \Pi$  [Atkins]. At equilibrium the chemical potential of A is the same in both the compartments, therefore:

$$\mu_A^0(p) = \mu_A(X_A, p + \Pi) \quad (2.1)$$

In compartment I, the chemical potential is only due to the pure solvent. Due to the presence of solute in compartment II, the chemical potential can then be written as:

$$\mu_A(X_A, p + \Pi) = \mu_A^0(p + \Pi) + RT \ln X_A \quad (2.2)$$

By taking the effect of pressure into account

$$\mu_A^0(p + \Pi) = \mu_A^0(p) + \int_p^{p+\Pi} V_m dp \quad (2.3)$$

where,  $V_m$  is the molar volume of the pure solvent A. Combining the above three equations, we get:

$$-RT \ln X_A = \int_p^{p+\Pi} V_m dp \quad (2.4)$$

For, dilute solutions,  $\ln X_A$  can be replaced by  $\ln(1 - X_B) \approx -X_B$ . It can also be assumed that the pressure range in the integration is so small that the molar volume of the solvent is nearly a constant and hence  $V_m$  can be taken outside of the integral.

Equation (2.4) can then be rewritten as:

$$-RT \ln X_A = V_m \Pi \quad (2.5)$$

The mole fraction of the dissolved solute (polymer) is  $\frac{n_B}{(n_A + n_B)} \approx \frac{n_B}{n_A}$  and the volume of the solvent can be given by  $n_A V_m = V$ . Substituting these terms in equation (2.5), we obtain van't Hoff equation:

$$\Pi V = n_B RT \quad (2.6)$$

By adjusting  $\frac{n_B}{V}$ , which is the molar concentration of the solute (polymer) with the molecular weight  $M$  and replacing it with concentration  $c$  (grams/litre). A relationship between the molecular weight  $M$  and  $\frac{\Pi}{c}$  is obtained. The deviation from ideal behavior is taken into account by the virial coefficient  $A_2, A_3$  [Atkins]:

$$\frac{\Pi}{c} = RT(1/M + RTA_2c + RTA_3c^2 + \dots) \quad (2.7)$$

Experimentally by measuring the osmotic pressure for a series of concentrations of polymer at a certain temperature and by plotting  $\frac{\Pi}{c}$  versus  $c$  and extrapolating it to zero concentration. we obtain  $RT/M$  which gives the molecular weight of the polymer. The slope gives the second virial coefficient  $A_2$  which is the measure of the interaction of two particles in solution which is a deviation from the ideal behaviour.

## 2.2 Osmotic Coefficient

Osmotic Coefficient in the case of polyelectrolyte solution can be defined as ( $\phi = \Pi/\Pi_{ideal}$ ) i.e., the ratio of the osmotic pressure measured to the calculated osmotic pressure expected in the case of an 'ideal gas' behaviour of the counterions. In other words, the osmotic pressure that would be expected in the absence of any type of interactions.

Consider a solution of polyelectrolyte molecules  $N_p$  having a degree of polymerization  $P_n$  dissolved in water with volume  $V$ , the polymer concentration can then be given as:

$$n_p = N_p/V \quad (2.8)$$

and the monomolar concentration as:

$$n_m = n_p P_n \quad (2.9)$$

If each monomeric unit carries an ionisable group and if  $\nu$  of the  $P_n$  ionisable groups are ionized, then the degree of ionization would be given as:

$$\alpha = \nu/P_n \quad (2.10)$$

If the ionisable groups are neutralized by monovalent counterions then concentration of the counterions can then given by:

$$n_c = n_p \nu = n_m \alpha \quad (2.11)$$

In case of an ideal behaviour, the osmotic pressure ( $\Pi$ ) would be dependent on the macroion as well as the counterion contribution and can be written as:

$$\Pi_{ideal} = (n_p + n_p \nu)kT = n_m \left( \frac{1}{P_n} + \alpha \right) kT \quad (2.12)$$

For high molecular polymers and for non-vanishing degrees of ionization  $\alpha$ , the degree of ionization is much larger than  $1/P_n$  then

$$\Pi_{ideal} = n_m \alpha kT \quad (2.13)$$

The term osmotic coefficient  $\phi$  is then introduced to take into account the non-ideal behaviour of polyelectrolytes.

The osmotic pressure  $\Pi$  can then be expressed as:

$$\Pi = (n_p + n_p \nu \phi) kT = n_m \left( \frac{1}{P_n} + \alpha \phi \right) kT \quad (2.14)$$

Although  $\phi$  is always smaller than 1,  $\phi \alpha$  is much larger than  $1/P_n$  therefore

$$\Pi \approx \alpha \phi n_m kT \quad (2.15)$$

Comparing the above equations (2.13) and (2.15) it is evident that the osmotic coefficient is a ratio of the ideal osmotic pressure and the real osmotic pressure observed. Hence:

$$\frac{\Pi}{\Pi_{ideal}} = \frac{(n_p + \phi n_p \nu) kT}{(n_p + n_p \nu) kT} \approx \phi \quad (2.16)$$

The experimental data on the osmotic coefficient ( $\phi$ ) [Kern 1938; Nagasawa et al. 1957, Alexandrowicz 1959,1960; Blaul et al. 2000 ] is generally found to be dependent on the linear charge density of the polyelectrolyte and does not vary strongly with the chemical nature of the polymeric chain. The stiff chain polyelectrolytes tend to have a larger osmotic coefficient as compared to the flexible polyelectrolytes. The osmotic coefficient is largely independent of the molecular weight and is fully determined by the local electrochemical properties of the polyelectrolytes.

The dilution of the polyelectrolytes does not lead to an increase in osmotic coefficient with stronger ‘dissociation’ of the counterions but a decrease in the osmotic coefficient is observed. This observation suggests a stronger interaction of the counterions with the polyion and thus a decrease in their osmotic activity. The nature of the counterions does not seem to affect the osmotic activity. An increase in the degree of ionization ( $\alpha$ ) decreases the osmotic coefficient [Katchalsky 1966].

## 2.3 Counterion Condensation

Based on the studies done on rod-like charges employing Poisson-Boltzmann equation [Imai, Onishi and Oosawa 1959, 1960, 1961] Manning through a series of publications in 1969 introduced the term ‘Counterion Condensation’. The theory of counterion condensation is based on the following assumptions:

1. The polyion is an infinitely long line charge having a maximum extension.
2. The two polyions have no interactions between each other.
3. The dielectric constant ( $\epsilon$ ) is same as that of the pure bulk solvent.

Based on these assumptions Manning’s counterion condensation theory for extremely dilute solutions predicts that, if the charge parameter  $\xi = \frac{\lambda_B}{b}$  of a polyelectrolyte solution is  $> 1$  then

the counterions present around the polyion would condense on the polyion to reduce the charge-density. The charge parameter  $\xi$  is lowered to unity or less than unity. This follows from the concept that polyelectrolytes dissociate into polyions and counterions in presence of a polar solvent. The counterions largely experience two forces. (i) The entropy of mixing which drives the counterions to distribute uniformly in the given volume. (ii) The electrostatic interactions which attract the counterions to oppositely charged polyions. Counterions are thus divided on the basis of two state model: uncondensed counterions and condensed counterions. The counterions which do not experience any electrostatic interactions and which are driven far away from the polyions are termed as ‘uncondensed’. On the other hand, counterions whose entropy of mixing has been overcome by the electrostatic interactions are correlated to the macroion and termed as ‘condensed’ [Nyquist et al. 1999]. The important conclusion of this theory is that the fraction of condensed counterions  $f_\xi$  for polyelectrolytes depends only on the charge parameter  $\xi$ .

For polyelectrolytes with unit charge and having a charge-density parameter  $\xi > 1$ ,  $f_\xi$  is given as:

$$f_\xi = \left(1 - \frac{1}{\xi}\right) \quad (2.17)$$

$f_\xi$  also known as the Manning-Fraction is predicted to be independent of the concentration and remains a constant at very high dilutions. Manning’s theory can be used to estimate the



thermodynamic properties of polyelectrolytes such as electrophoretic mobility, diffusion coefficient and electrical conductivity.

In the framework of the Manning counterion condensation theory, for an infinitely dilution solution and for charge parameter  $>1$ , the osmotic coefficient is described as:

$$\phi = \frac{1}{2\xi} \quad (2.18)$$

In contrast to the free counterions (Oosawa-Model), the uncondensed counterions of Manning Theory are subject to the Debye-Hückel potential of the polyion.

Comparing the condensed fraction (Equation 2.17) with the uncondensed fraction (Equation 2.18) it is evident that the fraction of condensed counterions is not equal to the fraction of uncondensed counterions.

$$f_{\xi} \neq 1 - \phi \quad (2.19)$$

The Manning theory describes the counterion distribution by a step function. The Poisson-Boltzmann Cell model describes the counterion distribution by a continuous function  $n(r)$  without differentiating between the condensed and the uncondensed counterions. The Poisson-Boltzmann treatment also describes a fraction of condensed counterions given by the integration constant  $R_M$  described previously [Le Bret, Zimm 1984; Deserno 2000].

## 2.4 Poisson-Boltzmann Equation for Salt Free Polyelectrolyte Solutions

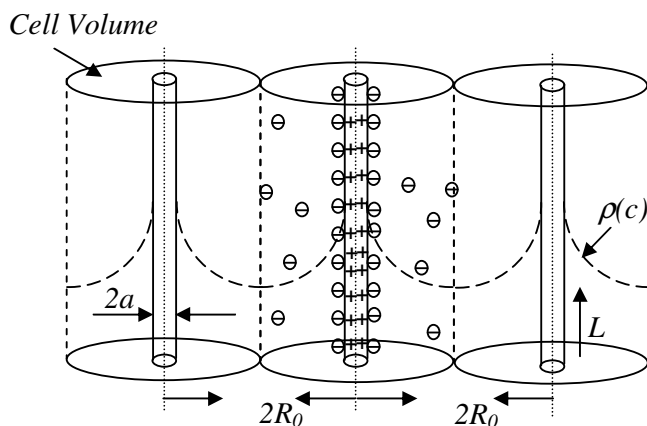


Fig. 2.2 shows the assumptions of a cell model. The infinitely long rod-like polyelectrolyte with radius ‘ $a$ ’, occupies the centre of the cylinder having a radius  $R_0$ . The charge on the macroion is neutralized by the counterions in the vicinity of the macroion.

The Poisson-Boltzmann equation can be solved for rod-like polyelectrolytes. Based on the assumption that the charged polyelectrolyte is situated in the axis of a coaxial electroneutral cylinder containing counterions equivalent to the charges on the polyion. The cylinder containing the polyion and its counterions is thus considered to be an uncharged entity in an electrically neutral environment i.e., the solvent. The model assumes that the electrostatic repulsion between the polyions leads to a homogenous distribution of the macroions where  $2R_0$  is the distance between two macroions. The model also considers the macroion to be an infinitely long rod. The rods are placed in an array parallel to each other confined within cylindrical cells where the rods are placed in the centre of the cylinder [Katchalsky 1971]. The height of the cylinder is given by  $h$ , where  $h$  is equal to the average length of the macroion,  $R_0$  being the radius of the cylinder and for a solution of polyelectrolyte containing  $n_p$  macroions per unit volume:

$$n_p \pi R_0^2 h = 1 \quad (2.20)$$

if the average cross section of the macroion is  $\pi a^2$  the volume  $V_p$  is given by:

$$V_p = a^2 / R_0^2 \quad (2.21)$$

The local potential is given through the Poisson-Equation:

$$\nabla^2 \psi(r) = -\frac{\rho(r)}{\varepsilon} \quad (2.22)$$

Where  $\rho(r)$  is the charge density distribution  $\varepsilon$  is the dielectric constant of the medium. In order to calculate the electrostatic potential  $\psi(r)$ , it is necessary to know the local charge density distribution  $\rho(r)$ , which is given by the Boltzmann equation:

$$\rho(r) = zn(r)e \quad (2.23)$$

where  $ze$  is the ionic charge and  $n(r)$  the counterion distribution. The counterion density distribution  $n(r)$  can be related to the electrostatic potential by the Boltzmann factor in the form:

$$n(r) = n(R_0)e^{(-e\Psi(r)/k_B T)} \quad (2.24)$$

The electric field vanishes at the cell boundary of the cylinder.  $n(R_0)$  is only the monovalent counterion density in the region close to the cylindrical cell boundary. It is not the mean or analytical concentration of the counterions in the bulk solution.

The Poisson equation in cylindrical coordinates is given by:

$$\left( \frac{d^2}{dr^2} + \frac{1}{r} \frac{d}{dr} \right) \Psi(r) = -\frac{en(r)}{\varepsilon} \quad (2.25)$$

In order to solve the Poisson Equation we need to define the screening constant  $K$ , Bjerrum length  $\lambda_B$ , the charge parameter  $\xi$  and the reduced electrostatic potential  $y$ .

The screening potential  $K$  can be written as:

$$K^2 = 8\pi\lambda_B n(R_0) \quad (2.26)$$

$n(R_0)$  is the concentration of the monovalent counterions in the region close to the cylindrical cell boundary and  $\lambda_B$  is the Bjerrum length:

$$\lambda_B = \frac{e^2}{4\pi\epsilon k_B T} \quad (2.27)$$

The charge parameter also known as the Manning parameter is a measure of the charges on the surface of the macroions:

$$\xi = \frac{\lambda_B}{b} \quad (2.28)$$

where  $\lambda_B$  is the Bjerrum length and  $b$  is the distance between the two ionic groups.

Using the above defined parameters the reduced electrostatic potential  $y$  is defined as:

$$y = -\frac{e\Psi(r)}{k_B T} \quad (2.29)$$

Combining the Poisson Equation with the Boltzmann factor and multiplying both sides by  $e/k_B T$ , the Poisson-Boltzmann Equation can then be written as:

$$\left( \frac{d^2}{dr^2} + \frac{1}{r} \frac{d}{dr} \right) y(r) = K^2 e^{(y)} \quad (2.30)$$

Equation (2.30) is non-linear differential equation of second order. The solution for this Equation can be obtained by introducing two boundary conditions:

The electrostatic potential decreases with the distance  $(d\Psi/dr)_{R_0} = 0$  from the macroion and vanishes to zero at the cell boundary  $\Psi_{R_0} = 0$ .

$$\left( \frac{dy}{dr} \right)_{r=R} = 0 \quad (2.31)$$

The second condition is based on the electroneutrality of each solution cell. For a cylinder with diameter  $2a$ , the electric field on the surface at  $r=a$  is given by: [Vogel 1999]

$$\left(\frac{d\Psi}{dr}\right)_{r=a} = -\frac{\sigma}{\epsilon_0\epsilon_r} \quad (2.32)$$

Since the polyion is a cylinder of radius  $a$ , length  $N_p b$ , and is uniformly charged then the surface charge density is given as: [LeBret, Zimm 1984]

$$\sigma = \frac{1}{(2\pi ab)} \quad (2.33)$$

Using the reduced electrostatic potential  $y$  the Bjerrum length  $\lambda_B$  and the Manning-Parameter  $\xi$  Equation (2.32) is given as:

$$\left(\frac{dy}{dr}\right)_{r=a} = -\frac{2\xi}{a} \quad (2.34)$$

The exact solution for Equation (2.30) was given by [Fuoss et al. 1951; Alfrey et al. 1951; Le Bret, Zimm 1984; Deserno et al. 2000]

$$y(r) = \ln \left[ \left\{ \frac{2|\beta|}{\kappa r \cos\left(\beta \ln\left(\frac{r}{R_M}\right)\right)} \right\}^2 \right] \quad (2.35)$$

$\beta$  and  $R_M$  are the two integration constants. By solving the exact solution of the PB-Equation for the two boundary conditions, two coupled equations for  $\beta$  and  $R_M$  can be obtained: [Le Bret, Zimm 1984; Deserno 2000]

$$\beta \tan \left[ \beta \ln \left( \frac{a}{R_M} \right) \right] = 1 - \xi \quad (2.36)$$

$$\beta \tan \left[ \beta \ln \left( \frac{R_0}{R_M} \right) \right] = 1 \quad (2.37)$$

Subtracting Equation (2.36) from Equation (2.47) eliminates  $R_M$  and the integration constant  $\beta$  can be calculated as:

$$\arctan \left( \frac{\xi - 1}{\beta} \right) + \arctan \left( \frac{1}{\beta} \right) - \beta \ln \left( \frac{R_0}{a} \right) = 0 \quad (2.38)$$

The second integration constant follows as:

$$R_M = a \exp \left\{ \frac{1}{\beta} \arctan \left( \frac{\xi - 1}{\beta} \right) \right\} \quad (2.39)$$

where  $R_M$  is the measure of the condensed counterions and is also termed as the Manning radius [Le Bret, Zimm 1984].

The screening potential  $K^2 = 8\pi\lambda_b n(R_0)$  can then be written as:

$$K = \frac{4(1 + \beta^2)}{R_0^2} \quad (2.40)$$

Substituting  $y(r)$  in the Boltzmann factor, the number of ions per unit volume at  $(r)$  can then be given as:

$$n(r) = \left[ \left\{ \frac{2|\beta|}{\kappa r \cos \left[ \beta \ln \left( \frac{r}{R_M} \right) \right]} \right\}^2 \right] n(R_0) \quad (2.41)$$

For salt-free polyelectrolyte solutions without added salt, the PB-cell model was solved exactly to yield the osmotic coefficient for finite concentrations of polyelectrolyte solutions [Fuoss et al. 1951; Alfrey et al. 1951; Katchalsky et al. 1961]. The above solutions allow us

to calculate important thermodynamic quantities such as osmotic coefficient of polyelectrolytes. [Alexandrowicz et al. 1966; Katchalsky et al. 1971].

Within the framework of the PB-Cell model the osmotic coefficient  $\phi$  of a system having monovalent counterions and charge parameter  $\xi > 1$  is given through [Lifson, Katchalsky 1954]:

$$\phi = \frac{1 - \beta^2}{2\xi} \quad (2.42)$$

In the limit of infinite dilution, where  $R_0 \rightarrow \infty$ , then  $\beta \rightarrow 0$ , therefore from the Poisson-Boltzmann Cell model the well-known Manning limit is recovered  $\phi_\infty = \frac{1}{2\xi}$ .

Both the Poisson-Boltzmann Cell Model and Manning's laws have been extensively used by researchers to study rod-like polyelectrolytes in aqueous solutions as eg. DNA, poly(paraphenylene) [Alexandrowicz et al. 1969; Blaul et al. 2000].

The treatment of flexible polyelectrolytes within the framework of the Cell Model has been a matter of great debate. Flexible polyelectrolytes undergo conformational changes and are not always in a maximum extended conformation. The assumptions of Cell Model require the polyelectrolyte chains to be in maximum extended conformation.

The experimental and theoretical values obtained from the PB-theory for monovalent ions are in good agreement if the charge parameter  $\xi$  is treated as an adjustable parameter [Alexandrowicz et al. 1969; Blaul et al. 2000].

Computer simulations have shown that the experimental results of the osmotic coefficient measurements of rod-like polyelectrolytes are in good agreement if the ion correlations and the finite size of the rod is taken in account [Deserno 2001]. These computer simulations allow the osmotic coefficient to be treated as an adjustable parameter unlike the PB Cell Model, where the osmotic coefficient is a non-adjustable parameter.

## 2.5 Small Angle X-Ray Scattering

### 2.5.1 Introduction

Small angle x-ray scattering (SAXS) is an analytical X-ray application in which the incident radiation is elastically scattered by a sample. The resulting scattering pattern is used to analyse and to extract information about the size, shape, orientation as well as the inter-particle interactions of the scattering entity. X-rays are electromagnetic waves having wavelengths between 0.01-1 nm. SAXS experiments are mostly carried out within a wavelength range of 0.05-0.25 nm. SAXS is sensitive to the electron density differences, since X-rays interact mainly with the electrons in the sample.

SAXS can be used for structural investigations of particles having a typical length scale (1-300 nm). SAXS does not require the scattering particles to be crystalline in nature. Hence this technique is ideal to investigate soft matter like macromolecules or colloids. Using SAXS, both monodisperse and polydisperse systems can be studied. In the case of monodisperse systems size, shape and internal structure of the particles can be determined. However, for polydisperse systems of the same shape, the size distribution of such systems can be studied. At very small angles, the shape of the scattering in the so-called Guinier region is used to obtain information about the radius of gyration of the scattering particles. In case of very dilution mono-disperse solutions, at higher angles, broad peaks can be observed which provide information on the shape of the particles. At very higher angles, i.e., the Porod region, the shape of the curve is used to obtain information on the dimensions of the scattering particles.

Small-angle scattering methods are a very effective tool to investigate the correlation of the counter ions to macro ions. In small-angle neutron scattering experiments, the partial contribution to the measured intensity  $I(q)$ , where  $q = \frac{4\pi}{\lambda} \sin(\theta/2)$ ; ( $\lambda$ = wavelength of radiation,  $\theta$  the scattering angle) can be determined by adjusting the contrast of the solution by appropriate mixtures of H<sub>2</sub>O and D<sub>2</sub>O. This requirements of deuterated counter ions makes the application of SANS to systems with usual counter ions impossible. Recently studies on DNA and cylindrical micelles have been carried out using SAXS methods [Wu et al. 1988; Chang et al. 1990]. SAXS generally requires the exchange of counter ions as e.g., exchange of chloride ions with iodide ions to obtain information on the distribution of the counter ions around the macro ion [Guilleaume et al. 2000, 2002]. The analysis by SAXS leads to a combination of partial scattering function depending on the contrast of the counter ion and the



macro ion. Hence the experimental difficulties encountered during exchange of counter ions and the use of deuterated ions make the interpretation of the data relatively difficult.

Anomalous small angle x-ray scattering (ASAXS), on the other hand circumvents these problems related to other scattering methods in a very efficient manner [Stuhrmann 1985, 1991]. ASAXS exploits the dependence of the scattering factor  $f$  in the immediate vicinity of the absorption edge. Decomposition of the scattering intensities obtained through an ASAXS experiment leads to three partial intensities: a] A non-resonant term that originates from non-resonant part of the scattering length density; b] a cross term and c] a self-term related to the resonant part of the scattering length density [Stuhrmann 1985]. In general, using ASAXS it is possible to retrieve information pertaining to the distribution of the counter ions from the resonant part of the scattering length density.

### 2.5.2 Scattering Theory

The theory of SAXS follows from the considerations:

1. The refractive index of x-rays is of the order of  $1-10^{-6}$  and therefore very close to unity. Refraction can therefore be neglected in the interaction of x-rays with matter.
2. X-rays interacting with matter scatter in two different ways: elastic scattering and Compton scattering. Only elastic scattering is considered, i.e., Compton radiation is negligible in case of X-rays because the relationship between elastic scattering and Compton scattering is dependent on the scattering angles. At zero scattering angles, the Compton scattering is equal to zero. At very small scattering angles it increases proportional to  $\sin^2\theta$  [Guinier 1963]. At the angles used in SAXS the Compton scattering can be neglected in good approximation.
3. The dimensions of the scattering entity are much smaller than the distances between the object and the detector.

The electrons present in matter interact with the incident radiations and emit secondary waves with identical frequency. These secondary waves contribute to the 'scattering intensity' of the system [Guiner 1963].

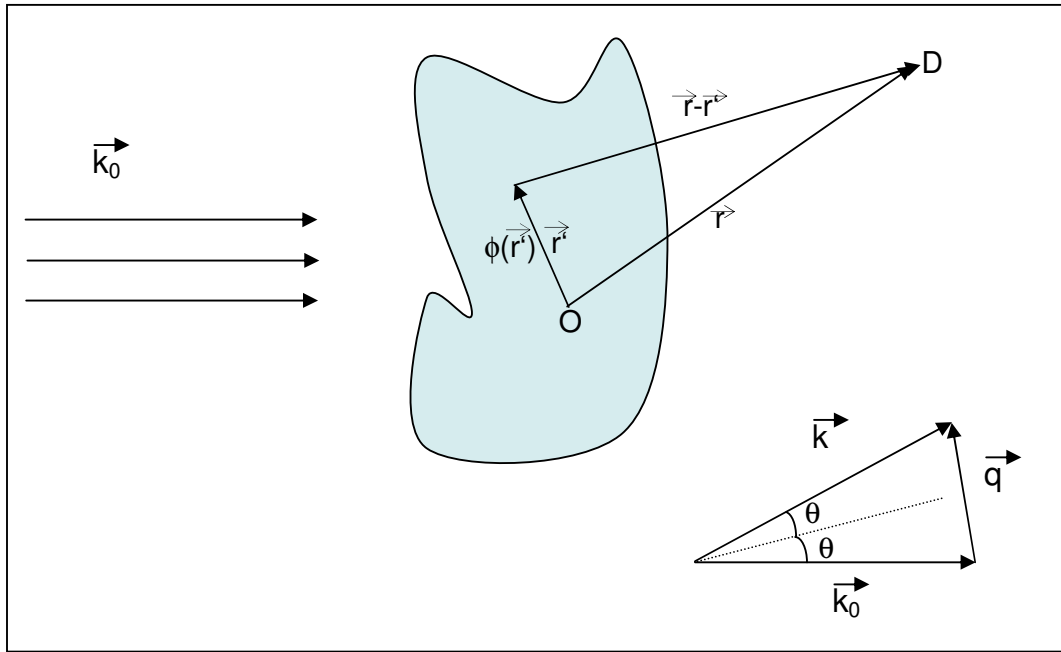


Fig. 2.3: Scattering of a plane wave by a point scatterer O, where  $k_0$  is the wave number of the incident radiation, point  $\vec{r}'$  is the origin of a spherical wave and the amplitude of the radiation observed at point  $\vec{r}$ , is the superposition of all these waves.

Fig. 2.3 shows a monochromatic wave incident at any point scattering center O, which generates spherical secondary waves.

At some observation point D i.e., at the detector the resulting wave can be described as: [Cowley 1975]

$$A_0 \exp(i\vec{k}_0 \vec{r}) + \left( A_0 \frac{b}{r} \right) \exp(i\vec{k} \vec{r}) \quad (2.43)$$

where  $k_0$  and  $k$  are the incident and scattering wave vectors with  $|\vec{k}_0| = |\vec{k}| = \frac{2\pi}{\lambda}$ ,  $\lambda$  is the wavelength,  $A_0$  and  $A_0 \frac{b}{r}$  are the scattering amplitudes and ' $r$ ' is the vector which determines an observation point D corresponding to the scattering center O. ' $b$ ' is the scattering length or the scattering amplitude of the scattering center and is dependent on the interaction between the incident wave and the point O [Svergun 1987].

The scattering of a radiation by three-dimensional object can be considered as an interaction of particles with the potential field  $\phi(\vec{r})$  [Cowley 1990].

The wave  $\varphi(\vec{r})$  scattered by the field  $\phi(\vec{r})$  is then sought as a solution of the wave equation:

$$\left[ \Delta^2 + k_0^2 + v\phi(\vec{r}) \right] \varphi(\vec{r}) = 0 \quad (2.44)$$

where  $k_0$  is the wave number of the incident radiation in free space and  $v$  is a parameter characterizing the strength of interaction with the potential field.

The solution of Equation (2.44) is given in the form of first Born approximation, i.e., the scattering amplitude is then equal to the sum of two components at a point D:

$$\varphi^{(0)}(\vec{r}) + \varphi^{(1)}(\vec{r}) = A_0 \exp(i\vec{k}_0 \vec{r}) + \frac{A_0 v}{4\pi} \int \frac{\exp[ik(\vec{r} - \vec{r}')] }{|\vec{r} - \vec{r}'|} \phi(\vec{r}') \exp(i\vec{k}_0 \vec{r}') d\vec{r}' \quad (2.45)$$

Since the detector position  $D$  is placed far away from the scattering object,  $|r - r'|$  is very large compared to the dimensions of the scattering area.

Hence it is equivalent to Fraunhofer diffraction and the asymptotic form of the scattering wave is given in the form:

$$\varphi^{(0)}(\vec{r}) + \varphi^{(1)}(\vec{r}) = A_0 \exp(i\vec{k}_0 \vec{r}) + \frac{A_0 v}{4\pi} \int \frac{\exp[ik_0 r]}{r} \phi(\vec{r}') \exp(i\vec{q} \vec{r}') d\vec{r}' \quad (2.46)$$

where the scattering vector  $\vec{q}$  is defined through

$$\vec{q} = \vec{k} - \vec{k}_0 \quad \text{and} \quad |\vec{q}| = \frac{4\pi}{\lambda} \sin\left(\frac{\theta}{2}\right) \quad (2.47)$$

The scattering amplitude  $F(\vec{q})$  through the potential field  $\phi(\vec{r}')$  is given by:

$$F(\vec{q}) = \frac{v}{4\pi} \int \phi(\vec{r}') \exp(i\vec{q} \vec{r}') dr \quad (2.48)$$

The scattering amplitude  $F(\vec{q})$  from Equation (2.48) is resulting from the first Born approximation and can be calculated from the Fourier-transform of the potential field  $\phi(\vec{r}')$ .

### 2.5.3 Scattering Intensity

The intensity of the scattered radiation follows as the square of the modulus of the scattering amplitude. In an experiment the scattering amplitude cannot be measured but only the flow of scattering energy or the number of scattered particles proportional to the square of the scattering amplitude. [Svergun 1987]

$$I(\vec{q}) = \frac{A_0}{r^2} F(\vec{q}) F^*(\vec{q}) = \frac{A_0}{r^2} I_0(\vec{q}) \quad (2.49)$$

The intensity termed as  $I_0(\vec{q})$  is the absolute scattering intensity of a single particle normalized by the factor  $\frac{A_0}{r^2}$ , which is the factor related to the experimental conditions.

For SAXS-experiments the potential field  $\phi(\vec{r})$  is described as the spatial distribution of scattering elements. Due to the large number of electrons of the scattering objects, the spatial distribution can therefore be described as a continuous density  $\rho(\vec{r})$  of the scattering centers. Therefore every volume element delivers a scattering amplitude proportional to the scattering amplitude  $F_{el}$  of each scattering center i.e., of each electron. The proportionality factor being the number of electrons in each volume element [Guinier, Fournet 1955].

The scattering amplitude now can be given as:

$$F(\vec{q}) = F_{el} \int_V \rho(\vec{r}) \exp(i\vec{q}\vec{r}) d\vec{r} \quad (2.50)$$

the scattering intensity which is the square of the modulus of the scattering amplitude can thus be described as:

$$I(\vec{q}) = F(\vec{q}) F^*(\vec{q}) = I_{el} \int_V \int_{V'} \rho(\vec{r}) \rho(\vec{r}') \exp i\vec{q}(\vec{r} - \vec{r}') d\vec{r} d\vec{r}' \quad (2.51)$$

The intensity  $I_{el}$ , which is the intensity of the secondary wave of an electron needs to be known in order to calculate the scattering intensity quantitatively.

$I_{el}$  can be calculated from the Thomson formula for the scattering intensity of free electrons [Laue 1960]:

$$I_{el}(\Theta) = I_p \frac{r_{el}^2}{d^2} \left( \frac{1 + \cos^2(2\Theta)}{2} \right) \quad (2.52)$$

$r_{el}$  is the electron radius  $r_{el} = \frac{e^2}{mc^2} = 2.82 * 10^{-13} \text{ cm}$ , 'd' the distance between the scattering object and the detector and  $I_p$  the primary beam intensity.

$I_{el}$  is the summation of elastic scattering intensity as well as Compton scattering [Guinier 1963] and since Compton scattering can be neglected at small angles, Equation (2.52) can also be used for bound electrons. Since the term arising from the Polarization factor

$\left( \frac{1 + \cos^2(2\Theta)}{2} \right)$  can be taken as unity for small angles,  $I_{el}$  can then be described to be a constant term. [Laue 1960]

Equation (2.51) shows that the measured intensity  $I(\vec{q})$  is derived from the Fourier transformation of the spatial distribution  $\rho(\vec{r})$ . The integration of which follows through the definition of vector ( $\vec{R} = \vec{r} - \vec{r}'$ ).

The scattering intensity can then be represented as:

$$I(\vec{q}) = \int P(\vec{R}) \exp[i\vec{q}\vec{R}] d\vec{R} \quad (2.53)$$

where the function  $P(\vec{R})$  is the convolution square of the scattering length distribution  $\rho(\vec{r})$

$$P(\vec{R}) = \int \rho(\vec{r}) \rho(\vec{r} + \vec{R}) d\vec{r} \quad (2.54)$$

Equation (2.53) provides a relationship between  $I(\vec{q})$  and  $P(\vec{R})$  through a Fourier transformation. Therefore

$$P(\vec{R}) = FT^{-1}[I(\vec{q})] = FT^{-1}[F(\vec{q})] * FT^{-1}[F^*(\vec{q})] \quad (2.55)$$

Since absorption has been excluded the distribution function  $\rho(\vec{r})$  is the real function and therefore:

$$FT^{-1} [F^*(\vec{q})] = \rho(-\vec{r}) \quad (2.56)$$

The Patterson function is given as:

$$P(\vec{R}) = \rho(\vec{r}) * \rho(-\vec{r}) = \int \rho(\vec{r})\rho(\vec{r} + \vec{R})d\vec{r} \quad (2.57)$$

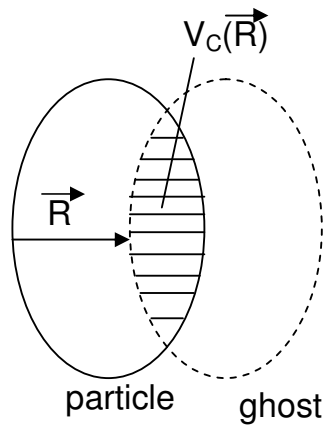


Fig 2.4 shows the Distance distribution function: Particle and “Ghost”

$P(\vec{R})$  is the convolution square of the scattering length distribution  $\rho(\vec{r})$  i.e.,  $P(\vec{R})$  is the convolution-square of the distribution function  $\rho(\vec{r})$  with itself inverted through the origin. The Patterson-function is described by the Particle-Ghost-Concept shown in Fig. 2.4. Thus the Patterson-Function finds interpretation through the common volume  $V_C(\vec{R})$  of the particle and its ‘ghost’. The function  $P(\vec{R})$  has non-zero values only if  $(\vec{r})$  and  $(\vec{r} + \vec{R})$  are inside the particle. Since the scattering Intensity  $I(\vec{q})$  is the Fourier-transformation of the Patterson function  $P(\vec{R})$ , such a convolution leads to the loss of the information about the phase. This is well known as the phase-problem.

## 2.5.4 Moving Particles

Up to now, all relationships were concluded assuming single particles in vacuum fixed in an incident radiation at a certain position and orientation. However, SAXS experiments are carried out on particles which are in motion i.e., particles which undergo Brownian motion. Translational motions give a constant phase factor for all scattering centres of an object. However, it keeps the scattering intensity unchanged, since the shift of a particle by a constant vector  $\vec{R}_0$  gives only an additional factor  $\exp[i\vec{q}\vec{R}_0]$  in front of scattering amplitude in Equation (2.50). This phase factor vanishes upon the calculation of  $I_0(\vec{q})$  and thus the scattering intensity remains unchanged. However rotational motion does play an important role, where the scattering objects have the identical probability of all possible orientations [Guinier; Fournet 1955]. Therefore rotation severely affects the phase factor  $\exp[i\vec{q}\vec{R}_0]$  because the angle between  $\vec{q}$  and  $\vec{R}$ , ( $\vec{R} = \vec{r} - \vec{r}'$ ) varies at random. The observed scattering intensity  $I_0(\vec{q})$  is thus given by an average over the solid angle  $\Omega$  of  $I_0(\vec{q})$ .

$$I_0(\vec{q}) = \frac{1}{4\pi} \int I_0(\vec{q}) d\Omega_q \quad (2.58)$$

Here the subscript  $\vec{q}$  means that the object is kept in a fixed position in spaces but the direction of  $\vec{q}$  is varied over  $4\pi$ .

The averaged scattering intensity of a scattering particle can be calculated through the Patterson function averaged over all orientations, denoted as  $\gamma(R)$ .

$$\gamma(R) = \frac{1}{4\pi} \int P(\vec{R}) d\Omega = \overline{P(\vec{R})} \quad (2.59)$$

The function  $\gamma(R)$  is then used to calculate the averaged scattering intensity:

$$\overline{I_0(\vec{q})} = \int \gamma(R) \exp[i\vec{q}\vec{R}] d\vec{R} = \iint \gamma(R) \cos(\vec{q}\vec{R}) R^2 d\Omega dR \quad (2.60)$$

The scattering intensity for an object with maximum dimensions is then finally obtained as:

$$I_0(\vec{q}) = 4\pi \int_0^{\infty} \gamma(R) \frac{\sin(qR)}{qR} R^2 dR \quad (2.61)$$

Equation (2.61) shows us that the scattering intensity  $I_0(\vec{q})$  measured for an ensemble of unoriented particles is related to the correlation function  $\gamma(R)$  by the sine-Fourier transformation. Thus by inverting the Equation (2.61) and changing the order of consecutive integrations keeping  $\vec{q}$  constant and varying the direction of  $\vec{R}$  over  $4\pi$  results:

$$\gamma(R) = \frac{1}{2\pi^2} \int I(q) \frac{\sin(qR)}{qR} q^2 dq \quad (2.62)$$

Equation (2.62) is an important result which provides the means of obtaining the distance distribution function  $\gamma(R)$  from the experimental SAXS data.

The average distance distribution function  $\gamma(R)$  consists of all information about any scattering object which can be extracted through any scattering experiment. For  $R=0$ , the average distance function can be written as:

$$\gamma(0) = \int \rho^2(\vec{r}) d\vec{r} \quad (2.63)$$

For homogenous particles the correlation function  $\gamma(R)$  is given by the product  $\rho^2 V_p$ , where  $V_p$  is the volume of a single particle. Similar result can also be obtained from the Particle-Ghost Construction shown in Fig 2.4, where the overlap volume at  $R=0$  is the particle volume.

The characteristic function  $\gamma_0(R)$  is then given as:

$$\gamma_0(R) = \frac{\gamma(R)}{\gamma(0)} = \frac{1}{\rho^2 V_p} \gamma(R) \quad (2.64)$$



The characteristic function thus defined depends on the shape of the particle but not on its size or scattering length density. The function  $\gamma_0(R)$  decreases monotonously as a function of  $R$  and vanishes for  $R$  greater than the largest dimension of the particle.

### 2.5.5 Radius of Gyration

For very small scattering vector ( $qR \ll 1$ ) the spatially averaged phase factor

$\frac{\sin(qR)}{(qR)} \cong 1 - \frac{(qR)^2}{3!} + \dots$  when introduced in Equation (2.61) leads to:

$$I_0(q) = 4\pi \int \gamma(R) \left( 1 - \frac{(qR)^2}{6} + \dots \right) R^2 dR \cong I_0(0) \left( 1 - \frac{q^2 R_g^2}{3} \right) \quad (2.65)$$

$$R_g^2 = \frac{\int_0^\infty \gamma_0(R) R^4 dR}{2 \cdot \int_0^\infty \gamma_0(R) R^2 dR} \quad (2.66)$$

Because  $e^{-x} \cong 1 - x$ ,  $I_0(q)$  can then be expressed through:

$$I_0(q) \cong I_0(0) \exp \left[ -\frac{R_g^2}{3} \right] \quad (2.67)$$

Equation (2.67) is the well-known Guinier law [Guinier 1939]. The above stated equations allow to obtain  $R_g^2$  and  $I_0(0)$  from the scattering data in the region of smallest angles. The limitations being that the product of  $qR_g$  for most of the systems must be smaller than unity for spheres  $qR_g < 1.4$  [Kirste, Oberthür 1982].

Another important derivation of the Guinier-law [Guinier, Fournet 1955] is related to the gyration radius with the electron density of the scattering object:

$$R_g^2 = \frac{\int \Delta\rho(\vec{s}) s^2 d\vec{s}}{\int \Delta\rho(\vec{s}) d\vec{s}} \quad (2.68)$$

where  $\vec{s}$  is the vector taken from the center of gravity of  $\rho(\vec{r})$ . The Equation (2.68) gives a relationship between the radius of gyration and the scattering length density  $\rho(\vec{r})$ . Radius of gyration is the longest average length scale which measures the spatial extension of particles. It does not depend on the rotation of the scattering particle.

### 2.5.6 Contrast

SAXS experiments are usually conducted using suspension of particles in a medium of a scattering length  $\rho_m$ . The measured scattering intensity depends on the influence of the medium and the interference of the scattering amplitudes originating from different particles in the system. Since the contribution due to surrounding medium is an additive, the contribution emanating from the medium can be subtracted from the measured scattering intensity [Müller 1982]. In solution, the scattering particles are described through the electron density  $\rho(\vec{r})$  suspended in a medium  $\rho_m$ . In order to calculate the scattering intensity of the complete system we need to define the contrast.

The contrast is the difference in the electron density of the particle and the surrounding medium. It is also known as the excess electron density and given as:

$$\Delta\rho(\vec{r}) = \rho(\vec{r}) - \rho_m \quad (2.69)$$

Using the contrast term, Equation (2.51) for the complete system can then be written as:

$$I(\vec{q}) = \int_V \int_{V'} [\Delta\rho_m + \Delta\rho(\vec{r}')] \cdot [\Delta\rho_m + \Delta\rho(\vec{r})] \exp i\vec{q} \cdot (\vec{r} - \vec{r}') d\vec{r} d\vec{r}' \quad (2.70)$$

Because of the large scattering volume  $V$  the scattering function of the total system is very high and decreases rapidly with decreasing  $q$  because of the high radius of gyration. If  $D_0$  is the average dimension of volume  $V$  then the scattering  $I(\vec{q})$  of the entire volume is negligible beyond  $q_0 = 2\pi / D_0$  and can be neglected [Guinier, Fournet 1955]. The scattering intensity for a single particle can then be obtained as:

$$I_0(\vec{q}) = \int_{V_p} \int_{V'_p} \Delta\rho(\vec{r}) \Delta\rho(\vec{r}') \exp[i\vec{q} \cdot (\vec{r} - \vec{r}')] d\vec{r} d\vec{r}' \quad (2.71)$$

The method of *contrast variation* [Kirste; Stuhrmann 1965] has been very widely used for the analysis of colloidal particles. In this method the scattering length density of either the particle or the surrounding medium is varied which allows us to obtain independent scattering intensities for the system under consideration. Hence it is possible by using contrast variation technique to obtain more detailed information about the scattering entities.

There are two different conditions: (i) At infinitely high contrast the inner structure of the particle does not contribute to the small angle scattering. (ii) At vanishing contrast the intramolecular density distribution and the details of the internal structure are visible. Hence by varying the contrast of surroundings (SANS) or by variation of the energy of the incident variation (ASAXS) it becomes possible to extract more detailed information about the scattering particles.

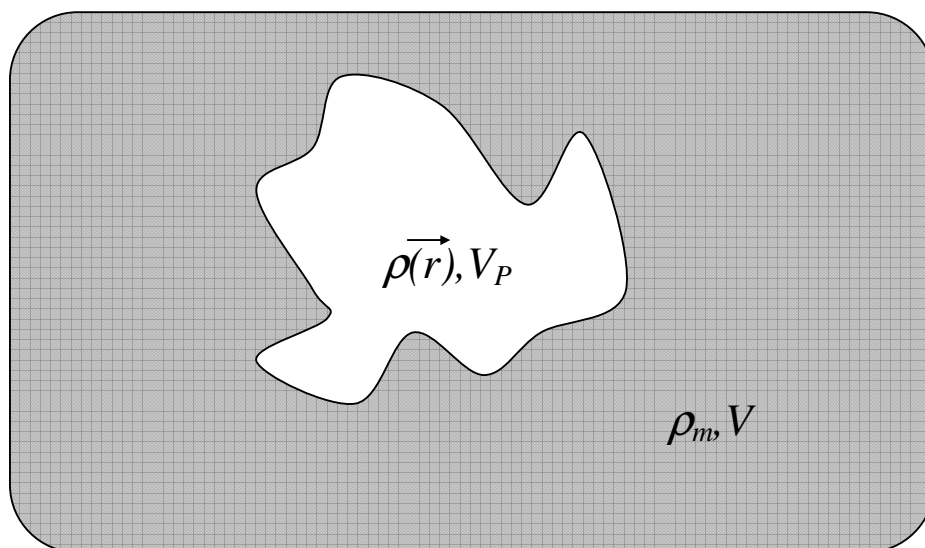


Fig. 2.5: Colloidal particles with Electron density  $\rho(\vec{r})$  and Volume  $V_P$  in a homogenous medium with electron density  $\rho_m$  and Volume  $V$ .

## 2.6 Scattering by Particles

### 2.6.1 Particles with radial symmetry (Spheres)

The scattering function  $I_0(q)$  of a single particle results from a spatial average of the squared amplitude; thus  $I_0(q) = \langle |F(\vec{q})|^2 \rangle$  is different from  $I_0(q) = \langle |F(\vec{q})| \rangle^2$ . In case of particles with radial symmetry the angular averaging Equation (2.58) is inconsequential and hence  $\langle |F(\vec{q})|^2 \rangle = \langle |F(\vec{q})| \rangle^2$ . Due to the centrosymmetric nature, the scattering amplitude of such an object is real and can be gives as:

$$F(q) = 4\pi \int_0^{R_0} \rho(R) \frac{\sin qR}{qR} R^2 dR \quad (2.72)$$

where  $R$  is the distance from the center of the sphere and  $R_0$  is radius.

For a homogenous sphere, by substituting  $u=q.R_0$  the integral can be obtained analytically.

The scattering intensity follows as

$$\begin{aligned} I_0(q) &= \rho^2 V_p^2 P(q) = \rho^2 V_s^2 \left[ \frac{3(\sin u - u \cos u)}{u^3} \right]^2 \\ &= \rho^2 V_s^2 \left[ \left( \frac{9\pi}{2u^3} \right)^{1/2} J_{3/2}(u) \right]^2 \end{aligned} \quad (2.73)$$

where  $J_{3/2}(u)$  is the Bessel function of order 3/2 and  $V_s$ , the volume of the sphere and  $P(q)$  is the 'Form factor'. This function is normalized to unity at  $q=0$  by division through the particles volume  $V_p$  and  $\rho^2$  embodies the angular dependence of  $I_0(q)$ .

From the above two Equations (2.72) and (2.73), the scattering length density  $\rho(r)$  can be obtained from the square root of the scattering intensity:

$$\rho(r) = \frac{1}{2\pi^2} \int_0^\infty [I_0(q)]^{1/2} q^2 \frac{\sin qr}{qr} dq \quad (2.74)$$

The scattering amplitude of a homogenous sphere can be derived as shown in Fig 2.6.

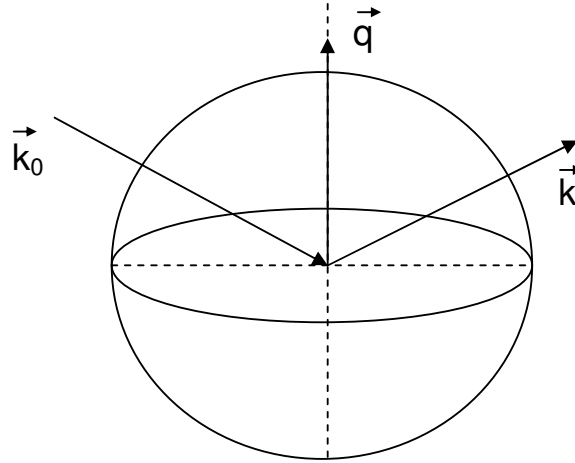


Fig 2.6 : Calculation of  $P(q)$  of a homogenous sphere.

The scattered amplitude originating from all points located in a given slice have the same phase and hence the scattered amplitude originating from all points can be calculated through integration over all slices. By assuming  $z=x/R_0$ , where the x-axis is taken along the direction of  $(\vec{q})$ , we obtain with  $u=q.R_0$ .

$$\begin{aligned}
 F(q) &= \int_{-1}^{+1} \cos(qzR_0) \pi R_0^2 (1-z^2) R_0 dz \\
 &= V_K \left( \frac{9\pi}{2u^3} \right)^{1/2} J_{3/2}(u) \quad (2.75)
 \end{aligned}$$

Hence the total amplitude results from the interference of waves reflected on planes perpendicular to the scattering vector  $(\vec{q})$ .

## 2.6.2 Particles with cylindrical geometry (Rod-like particles)

In case of strongly anisometric particles as rods. Consider a long cylindrical object of length  $L$  for which the internal coordinate  $\vec{R}$  may be defined in terms of an axial component  $\vec{z}$  and a radial component  $\vec{r}_c$  as shown in Fig. 2.7. Assuming that the scattering length density per unit length is characterized by a distribution  $\rho_c(\vec{r})$  which does not depend on  $z$ .

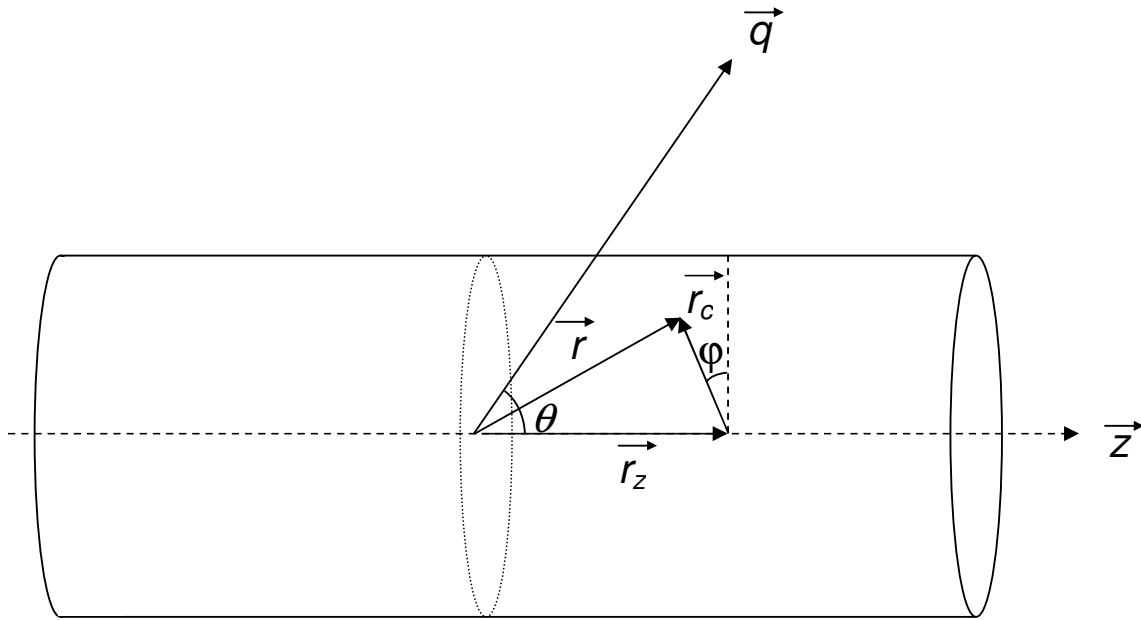


Fig 2.7: shows definition of coordinates in a cylindrical object.

For calculating the scattering function, the decoupling of  $F(\vec{q})$  into an axial factor and a factor related to the cross section is to be considered. [Fournet 1951].

The scattering amplitude  $F(\vec{q})$  can be given by:

$$F(\vec{q}) = \int_{-L/2}^{+L/2} 2\pi dz \int_0^{R_0} \rho(r_c) r_c dr_c \frac{1}{2\pi} \int_0^{2\pi} \exp[i(qr_z \cos(\theta) + qr_c \cos(\phi) \sin(\theta))] d\phi \quad (2.76)$$

After integration over angle  $\varphi$  and  $r_z$  we obtain the scattering amplitude  $F(q, \alpha)$  for a cylindrical object with orientation  $\alpha$ , where  $\alpha$  is the cosine of the angle between the scattering vector  $\vec{q}$  and the long-axis  $\vec{z}$  of the molecule.

$$F(q, \alpha) = L \frac{\sin(q\alpha L/2)}{q\alpha L/2} \int_0^\infty \Delta\rho(r_c) J_0 \left[ qr_c (1 - \alpha^2)^{1/2} \right] 2\pi r_c dr_c \quad (2.77)$$

$$= L \frac{\sin(q\alpha L/2)}{q\alpha L/2} F_{cr} [\Delta\rho(r_c), q, \alpha] \quad (2.78)$$

where the amplitude  $F_{cr} [\Delta\rho(r_c), q, \alpha]$  of the cross-section of the molecules is a function of radial distance  $r_c$ . Here  $\Delta\rho(r_c)$  is the radial excess scattering length density and  $J_0(x)$  is the Bessel-function of zeroth order.

The amplitude of the cross section of the molecules  $F_{cr} [\Delta\rho(r_c), q, \alpha]$  follows as:

$$F_{cr} [\Delta\rho(r_c), q, \alpha] = \int_0^\infty \Delta\rho(r_c) J_0 \left[ qr_c (1 - \alpha^2)^{1/2} \right] 2\pi r_c dr_c \quad (2.79)$$

The scattering intensity  $I_0(\vec{q})$  of a cylindrical object can then be obtained by averaging over all orientation of the scattering vector ( $\vec{q}$ ).

The scattering intensity is given by:

$$I_0(\vec{q}) = \int_0^1 F(q, \alpha) F^*(q, \alpha) d\alpha = \left\langle F(q, \alpha) F^*(q, \alpha) \right\rangle_\Omega \quad (2.80)$$

where  $F^*(q, \alpha)$  is the complex conjugate of the scattering amplitude.

If  $q \gg \frac{2\pi}{L}$ , then the rod gives only a contribution to the measured intensity if  $q$  is perpendicular to the long axis [Guilleaume et al. 2002]. The intensity thus measured at higher scattering angles is directly related to the Hankel-Transform of the excess electron density  $\Delta\rho(r_c)$ . Therefore  $I_0(\vec{q})$  probes the variation of the excess electron density along  $q_\perp$  i.e., along the radial direction and when  $\alpha = 0$ .

Thus,

$$I_0(\vec{q}) \approx L \frac{\pi}{q} F_{cr}(\Delta\rho(r_c), q_{\perp}, \alpha = 0) F_{cr}^*(\Delta\rho(r_c), q_{\perp}, \alpha = 0) \quad (2.81)$$

From Equation (2.81) it is evident that a scattering experiment performed on a cylindrical object delivers direct information over the cross-sectional distribution of the cylinder.

## 2.7 Anomalous Small Angle X-ray Scattering (ASAXS)

Anomalous small-angle X-ray scattering (ASAXS) is a method in which a series of small-angle X-ray scattering measurements are carried out at different energies. These measurements with energy variation bring a variation in the contrast of the scattering particle. This systematic variation in contrast yields the partial scattering functions of the atomic species. Anomalous small angle X-ray scattering (ASAXS) is the standard SAXS experiment in which the energy of the incident X-rays are adjusted near the absorption edge of an element in the sample.

The basic requirement of ASAXS is an x-ray source with variable photon energy, the intensity of such a source must remain largely constant as a function of photon energy over the required photon energy range.

When the incident x-ray energy is close to the binding energy of the core electron of an atom, there is a significant lowering of atomic scattering factor. This sharp decrease in the scattering factor is a result of the resonance effects on the X-ray photon by the bound core electron and termed as ASAXS. As the energy of the X-ray photons is increased above the binding energy, there is a sharp increase in the scattering factor of the element which is described through the imaginary part  $f''(E)$ . This discontinuity in the vicinity of the binding energy of the electron of an element is termed as the absorption edge for the element. With the recent advances in the synchrotron radiation, it has become practically possible to carry out ASAXS experiments due to the high intensity across a broad X-ray spectrum.

In the following thesis, the measurements were carried out at the K-absorption edge of bromine for stiff chain polyelectrolytes and rubidium in the case of spherical polyelectrolyte brushes and star-shaped polyelectrolytes. In the course of this thesis, it would be demonstrated that ASAXS indeed is a powerful tool to investigate the structural properties pertaining to the counterion correlation to the macroion in polyelectrolytes.



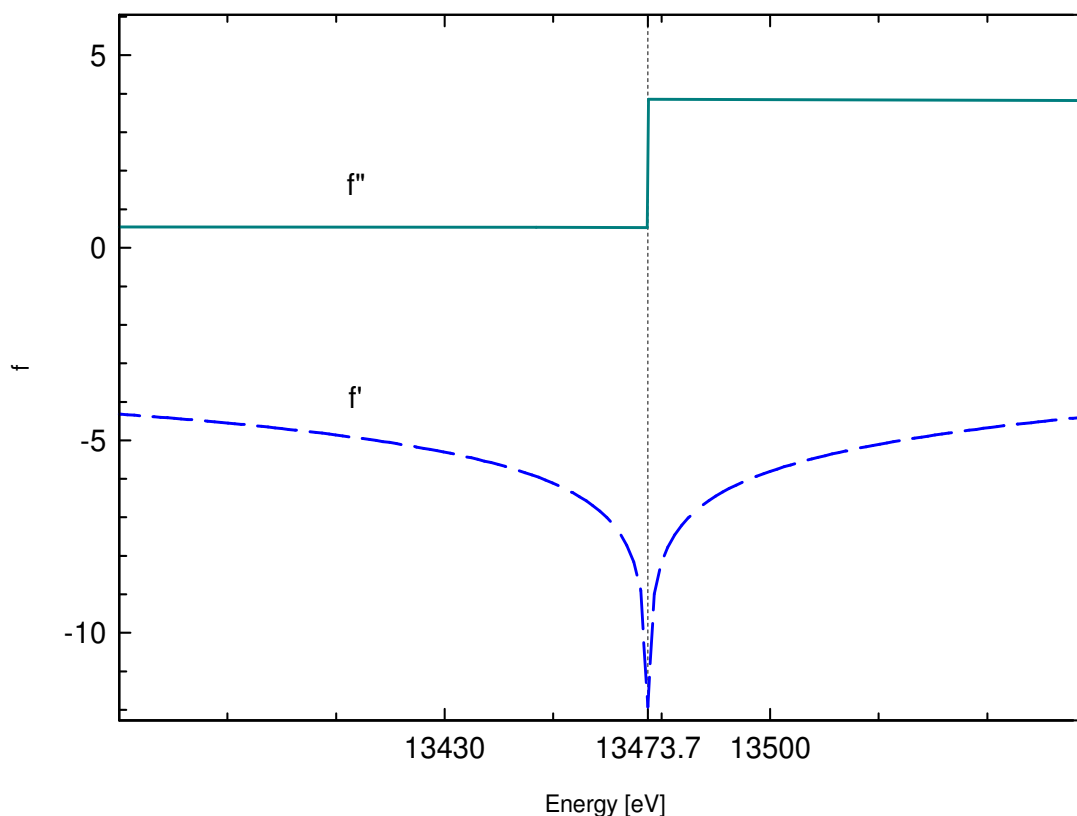


Fig 2.8 below depicts the dispersion of Bromine near the K-edge: the real and imaginary parts of  $f'$  and  $f''$  as a function of the energy of the incident radiation. The solid line shows the data for  $f''$  values and the long dashed lines are the values for  $f'$ . The solid vertical line marks the energy of the  $K_{\alpha}$ -edge of Bromine.

When the wavelength of the incident radiation is close to the absorption edge of an atom, the atomic scattering factor  $f$  becomes complex and is represented as (Fig 2.8) [James 1967]:

$$f_{ion} = f_0 + f'(E) + \tilde{i}f''(E) \quad (2.82)$$

where  $f_0$  is the energy-independent part of the scattering factor and is given through the atomic number of the atom,  $\tilde{i}$  is the imaginary unit and  $f'$  and  $f''$  are the real and imaginary terms of the energy-dependent part of the scattering factor and given through: [James 1967]

$$f'(\omega) = \frac{\omega_s^2(\omega^2 - \omega_s^2)}{(\omega^2 - \omega_s^2) + k^2\omega^2} \quad (2.83)$$

$$f''(\omega) = \frac{k\omega^3}{(\omega^2 - \omega_s^2) + k^2\omega^2}$$

The imaginary terms  $f'$  and  $f''$  are related to each other with the Kramers-Krönig-Transformation: [James 1967]

$$f'(\omega_0) = \frac{2}{\pi} \int_0^{\infty} \frac{\omega f''(\omega)}{(\omega_0^2 - \omega^2)} d\omega \quad (2.84)$$

The resonance absorption is also known as photoelectric absorption and given through the optical theorem as [Stuhrmann 1985]:

$$\sigma_p = 2\lambda \frac{e^2}{mc^2} f''(0) \quad (2.85)$$

Both the photoelectric absorption  $\sigma_p$  and  $f''(0)$  exist only on the short wavelength region of the absorption edge [Stuhrmann 1985].

The imaginary part  $f''$  is related with the linear absorption coefficient  $\mu$  through the following equation: [James 1967]

$$\mu(\omega) = \frac{4\pi e^2 N}{mc\omega} f'' \quad (2.86)$$

Considering an assembly of  $M$  atoms having fixed coordinates  $r$  with respect to an origin of which  $N$  atoms are assumed to have strong resonance scattering and all the strongly resonant scatterers have the same dispersion.

$$\begin{aligned} \rho(r) &= \sum_{n=1}^M f_{0,n} \delta(r - r_n) + (f' + f'') \sum_{n=1}^N \delta(r - r_n) \\ &= u(r) + (f' + f'')v(r) \end{aligned} \quad (2.87)$$

If  $U(r)$  and  $V(r)$  are the real and imaginary part of  $\rho(r)$  respectively then the scattering amplitude and its complex conjugate can be given as: [Stuhrmann 1985]

$$\begin{aligned}
 F(\vec{q}) &= \int [U(\vec{r}) + iV(\vec{r})] e^{i\vec{q}\vec{r}} d^3\vec{r} \\
 F^*(\vec{q}) &= \int [U(\vec{r}) - iV(\vec{r})] e^{-i\vec{q}\vec{r}} d^3\vec{r}
 \end{aligned}
 \tag{2.88}$$

The Equation 2.88 leads to the most important equation as: [Stuhrmann 1985]

$$I(\vec{q}) = I_u(\vec{q}) + f' I_w(\vec{q}) + (f'^2 + f''^2) I_v(\vec{q}) + f'' \varphi(\vec{q})
 \tag{2.89}$$

In the case of x-ray crystallography, apart from the Friedel pair, depending on the symmetry, there are also additional (mirror) symmetry elements. Two reflections related by a mirror plane in reciprocal space are known as a Bijvoet pair. The Bijvoet pairs are a result of the resonance effect of x-rays. These were later used to determine the absolute configuration of crystals [Bijvoet 1954, 1956]. The phase problem for the protein structure determination was previously solved by using the isomorphous replacement method. Isomorphous replacement method is the introduction of heavy atoms to form its corresponding derivative [Okaya et al. 1955]. The drawback of this method is, it requires chemical modifications to vary the contrast of the system and this may lead to the inconsistency between the parent system and its derivative. Equation (2.89) now allows an alternative method to circumvent the phase problem by a physical method rather than a chemical method. Hence, the problem of inconsistency of the system under study can be eliminated. From Equation (2.89) it is evident that, the effect of resonant scattering results in the breakdown of Friedel's law and renders the Bijvoet pairs of reflections  $I(\vec{q})$  and  $I(-\vec{q})$  unequal. The difference between the two terms is given by  $2f''\varphi(\vec{q})$  and is used to determine the absolute configuration of crystal structure and proteins [Fischer 1981, Bartunik et al. 1982, Stuhrmann 1985].

However in our case, we consider centrosymmetric particles. Therefore the integration of the phase over all angles is zero. Using Equation (2.88) and Equation (2.89) and  $\langle \varphi(\vec{q}) \rangle_{\Omega} = 0$ , the decomposition of the scattering intensity leads us to:

$$I(\vec{q}) = u^2(\vec{q}) + 2f' u(\vec{q})v(\vec{q}) + [f'^2 + f''^2] v^2(\vec{q})
 \tag{2.90}$$

Equation (2.90) allows us to separate different contributions to the scattering intensity and provides more detailed insight about the scattering particles.

## 3 Measurements and Analysis

### 3.1 Rod-Like Polyelectrolytes

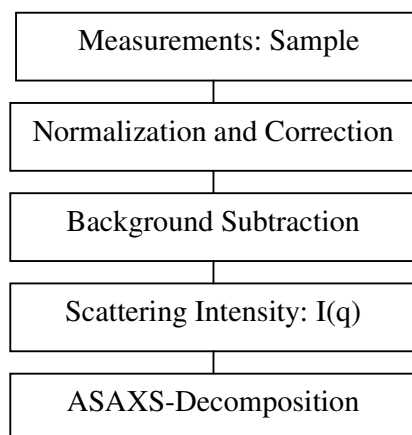


Chart 3.1 shows the steps followed in the treatment of the scattering data obtained from the ASAXS experiments carried out on rod-like polyelectrolytes

#### 3.1.1 Data Treatment

ASAXS measurements of rod-like polyelectrolytes bearing bromide counterions (6.7 g/l) were carried out at ID02 beamline at ESRF, Grenoble France. All data was determined using an image-intensified CCD detector. The 2D-data were circularly averaged with the software supplied at the beamline by the ESRF and normalized to the intensity of the primary beam. The change of the wavelength in the course of an ASAXS-experiment leads also to a shift of the  $q$ -value assigned to a given pixel of the detector. For evaluation of the data the intensity must be compared for the same  $q$  but for different energies of the incident beam. In order to correct for this effect, the scattering curves were interpolated to give a set of intensities for a given single set of  $q$ . This procedure however did not involve any smoothing of the acquired data [Bösecke et al. 1997; Narayanan et al. 2001].

### 3.1.2 Background Subtraction

For the background subtraction a constant at very high  $q$  values,  $q = 3.2-3.5$  was subtracted from the scattering intensities. This procedure removes all possible parasitic contributions resulting from the empty capillary, water and the fluorescence which sets in as the absorption edge of the ion is approached. This method also removes the contribution to scattering resulting from the longitudinal fluctuations of the counterions. These fluctuations come into play for highly charged macroions and give an additional contribution to the measured intensity [Guilleaume et al. 2002]. A detailed explanation for this method is given in the discussion section for rod-like polyelectrolytes.

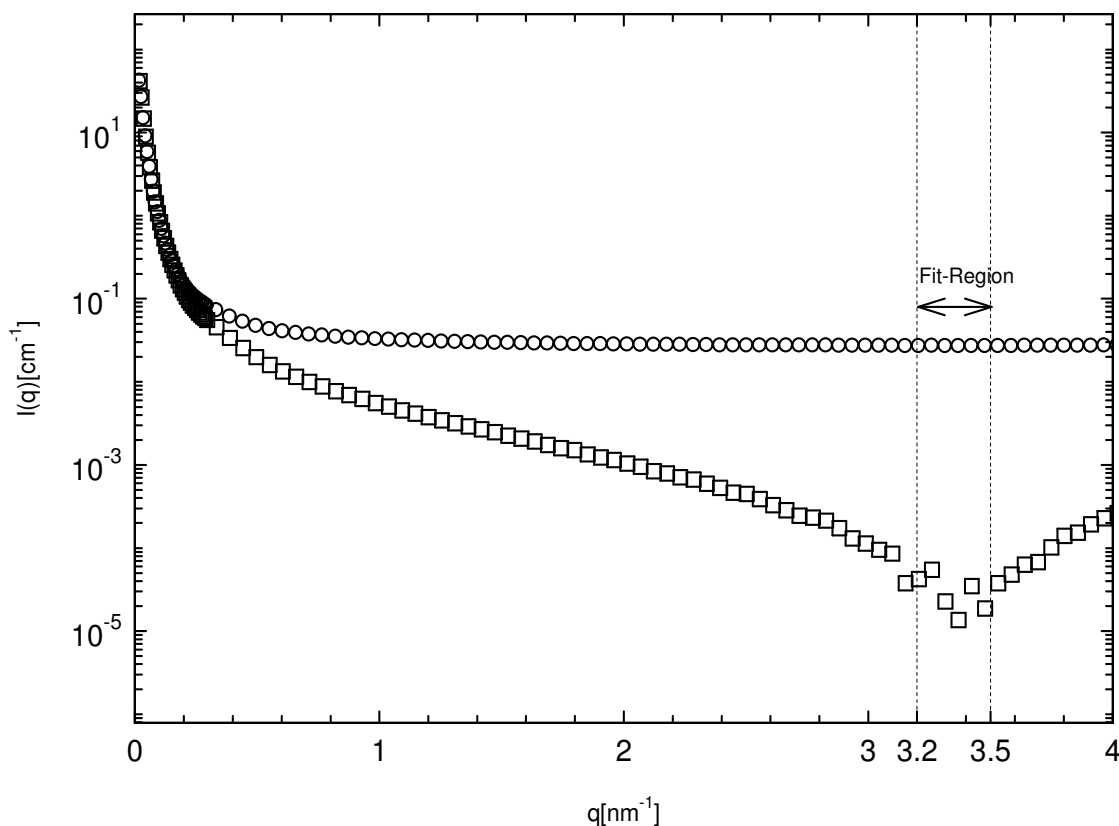


Fig. 3.1 shows an example of the background subtraction procedure carried out for rod-like polyelectrolytes. A constant was first determined in the region  $q = 3.2-3.5$ , for the parasitic contributions due to empty capillary, solvent (water) and fluorescence. Circles depict the scattering intensity before the subtraction; Squares depict the scattering intensity after the background subtraction procedure.

## 3.2 Spherical Polyelectrolyte Brushes

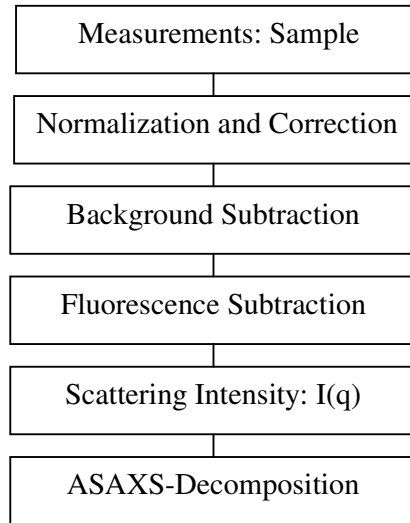


Chart 3.2 shows the steps followed in the treatment of the scattering data obtained from the ASAXS experiments carried out on spherical polyelectrolyte brushes.

### 3.2.1 Data Treatment

The normalization and correction of all data acquired for spherical polyelectrolyte brushes is done in the same manner as described in the Section. 3.1.1.

### 3.2.2 Background Subtraction

The scattering intensity  $I_{Tot}$  is the scattering intensity of the spherical polyelectrolyte brushes along with parasitic contributions due to the empty capillary and water. The scattering contribution emanating only due to the latex is separated from the parasitic contribution using the following formula [Müller 1982]

$$I_L = I_{Tot} - (1-\phi) I_{Bg} - \phi I_{Cap} \quad (3.1)$$

where  $I_L$  is the scattering intensity of the latex.  $I_{Tot}$  is the total scattering intensity obtained from any scattering experiment.  $I_{Bg}$  is the scattering contribution due to the dispersion medium (in this case water).  $I_{Cap}$  is the scattering due to the empty capillary and  $\phi$  is the

volume fraction. The computer program [Dingenouts Dissertation 1999] used for the background correction uses the approximated cubic splines method [Engeln-Müllges 1991] which allows the smoothing of the background scattering intensity if necessary.

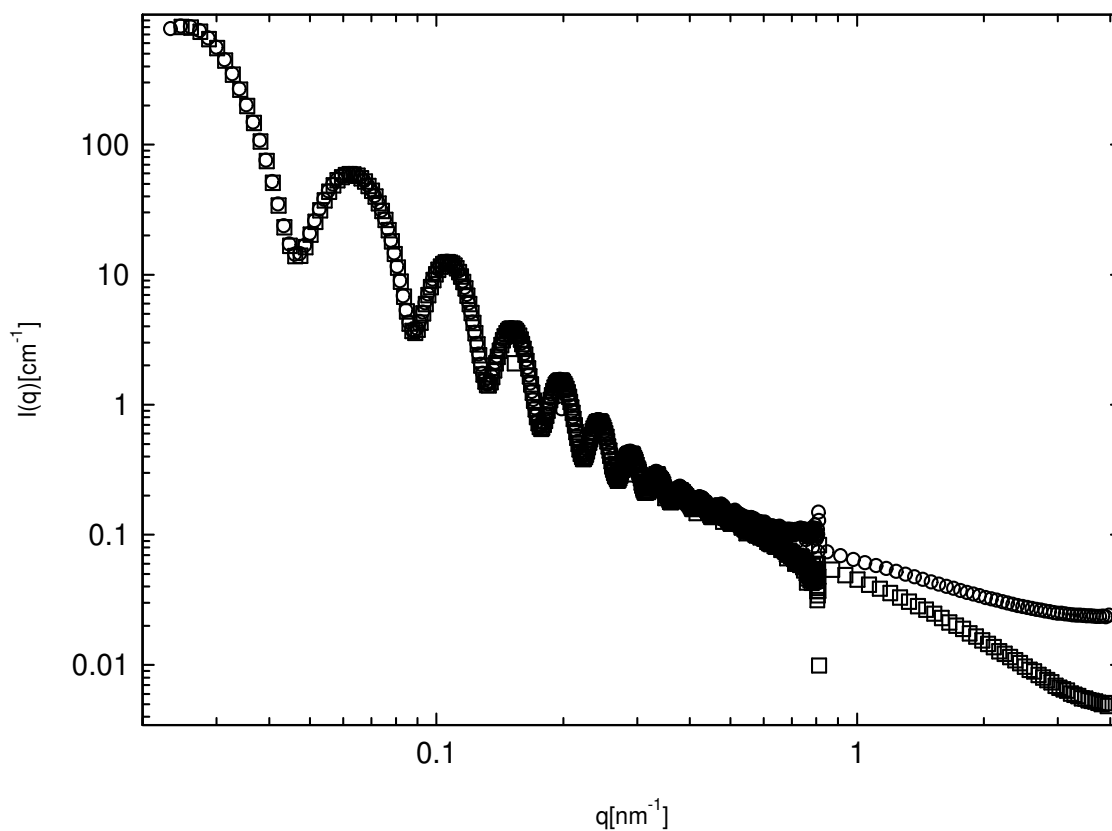


Fig. 3.2 shows an example of the background subtraction procedure carried out for spherical polyelectrolyte brushes. Circles depict the scattering intensity before the subtraction; Squares depict the scattering intensity after the background subtraction procedure.

### 3.2.3 Desmearing

Due to the finite beam size of the x-ray beam, small-angle scattering experiments carried out using slit-collimation systems result in the ‘slit-smearred’ scattering curve. Such curves show a loss of resolution in the structure of the measured curves and hence are required to be corrected for the same. The data acquired at 2m and 10m detector position are shown in Fig. 3.2 after normalization and background correction. The scattering curves at 2m position required to be deconvoluted for smearing. It is done using a module in the analysis program based on the deconvolution algorithm with the help of cubic splines [Beniaminy et al. 1980] and the approximated cubic splines used for the background correction [Engeln-Müllges 1991]. Such type of correction is not necessary for structureless scattering curves [Hickl 1996], hence such a procedure was not carried out for stiff chain polyelectrolytes. No such desmearing is necessary for the data acquired at 10m detector position.

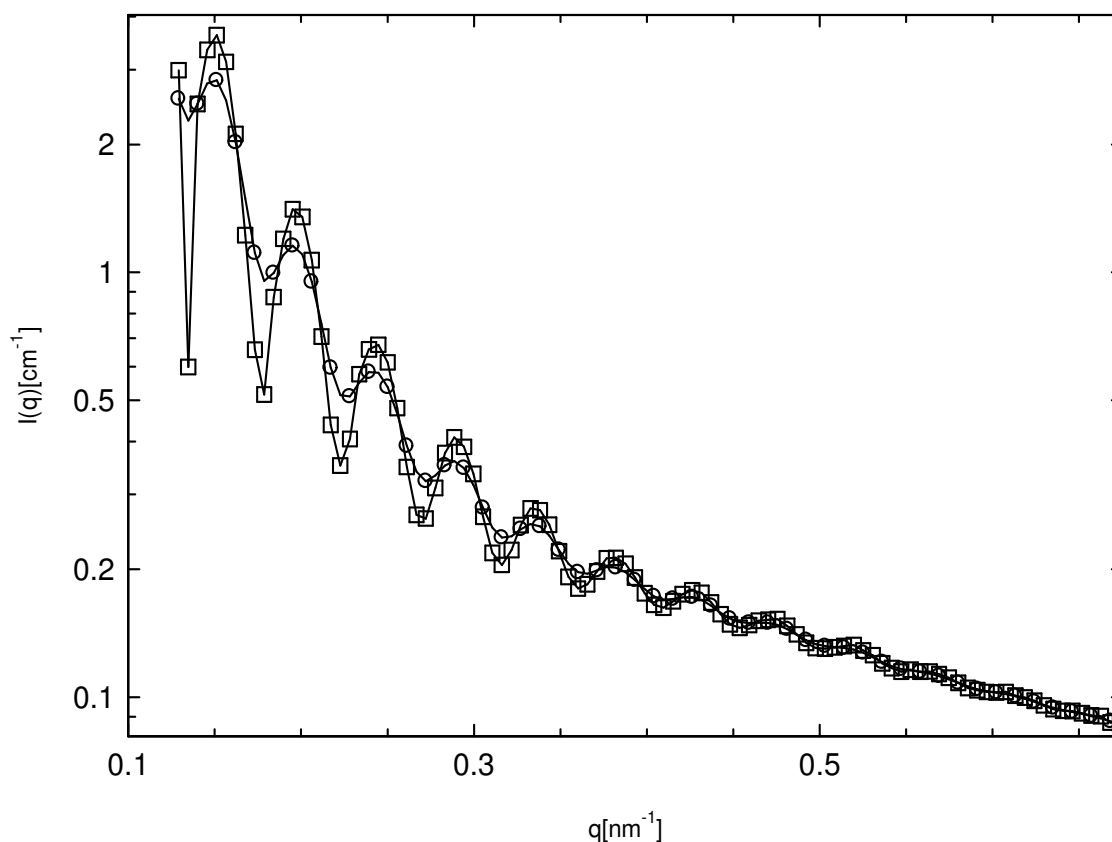


Fig. 3.2 shows an example of the desmearing procedure carried out for Spherical polyelectrolyte brushes. The Circles depict the scattering intensity acquired at the detector position 2m before the desmearing procedure; Squares depict the scattering intensity after the desmearing procedure.



### 3.2.4 Setting together the 2m and 10m scattering intensities

After the correction for background and deconvolution of data at 2m detector position it can be seen that the data acquired at 2m position and 10m position do not fit together in terms of the height of the scattering curves. This can arise due to a number of factors like the CCD-correction or the background correction. The data acquired at 2m position is reliable, as the background correction does not play a significant role here. The data at 10m position was therefore shifted to match the data obtained at 2m position. The 10m position data needs to be corrected by about 5-10% in order to obtain a good fit for both positions to deliver a complete  $q$ -range from 0-4  $\text{nm}^{-1}$ . Differences such as this occur due to calibration errors. Such a relative difference of 10% between the intensities obtained at 10m and 1m was also found to exist for the scattering curve of a calibration sample Lupolen at the ID02 beamline of ESRF, Grenoble [Bösecke et al. 1997].

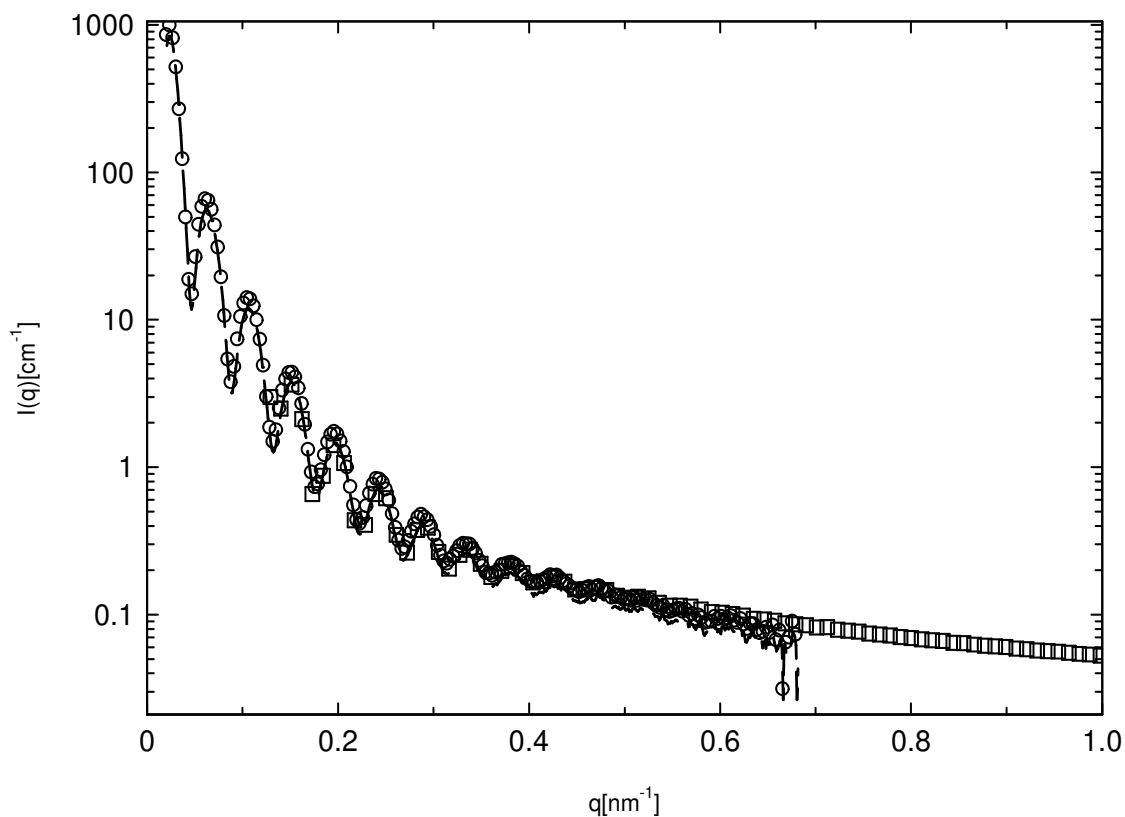


Fig. 3.3 shows an example of the setting procedure carried out for Spherical polyelectrolyte brushes for 2m and 10 m . The Circles depict the scattering intensity acquired at the detector position 10m at an energy 12460 eV; dashed line shows the 10m curve after 5% correction of the scattering intensity; Squares depict the scattering intensity obtained at 2m.

### 3.2.5 Fluorescence Subtraction

When the incident x-ray energy is above the electron binding energy, a strong increased background results in ASAXS experiments. This increased background which is a constant at higher q-values is termed as fluorescence. The energy resolution of the beamline ID02 (ESRF, Grenoble, France) allows us to carry out experiments within a very small energy range. But since the energy beam has a finite size, as the absorption edge is approached a part of the primary beam lies beyond the absorption edge and hence gives rise to fluorescence. Fig.3.4 shows the primary beam profile at an energy (15198 eV). As is evident from the Fig. 3.4 a part of the beam is already beyond the absorption edge which lies at 15199.7 eV.

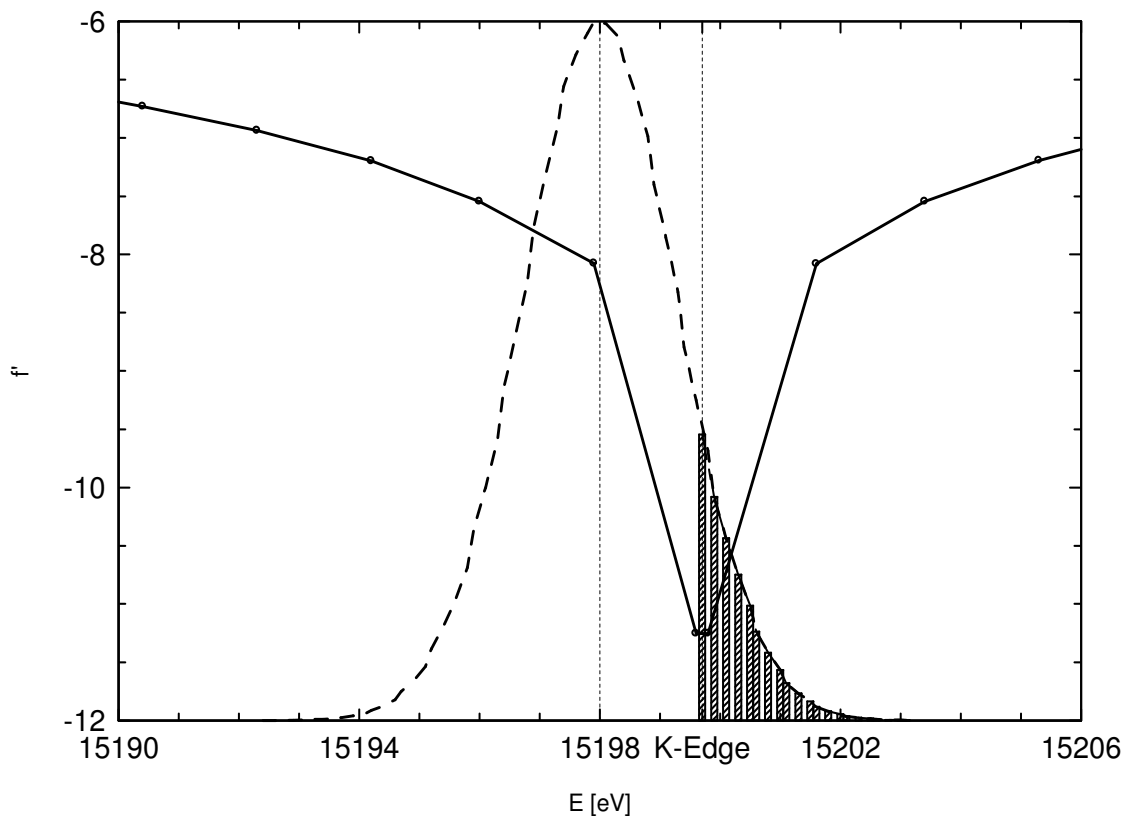


Fig. 3.4 shows the profile of the incident beam for energy 15198 eV. The dashed lines represent the beam profile. The solid line represents the  $f'$  values. The vertical line at 15198 eV represents the energy at which the measurements are taken, while the vertical line at 15199.7 denoted as the K-edge is the theoretical value for the absorption edge of Rubidium.

The incoherent scattering contribution of fluorescence in addition to the coherent scattering can be assumed to be an additive and can be removed from the total scattering intensity. To

eliminate the incoherent scattering contribution, at  $q = 4$  a constant was determined for reference curve which had no influence of fluorescence (i.e., scattering intensity measured far away from the absorption edge). The difference between the constant at  $q = 4$  of the reference scattering curve and the constant of the scattering curve with incoherent scattering contribution was then subtracted from the corresponding curve. The correction thus effected is rather small in as much the present work is restricted to the  $q$ -range given by  $q < 0.6 \text{ nm}^{-1}$  in the case of spherical polyelectrolytes. Moreover, all data discussed here have been taken below the edge in order to minimize the problem of fluorescence. Fig. 3.4 shows that this problem becomes appreciable only in the immediate neighbourhood of the edge.

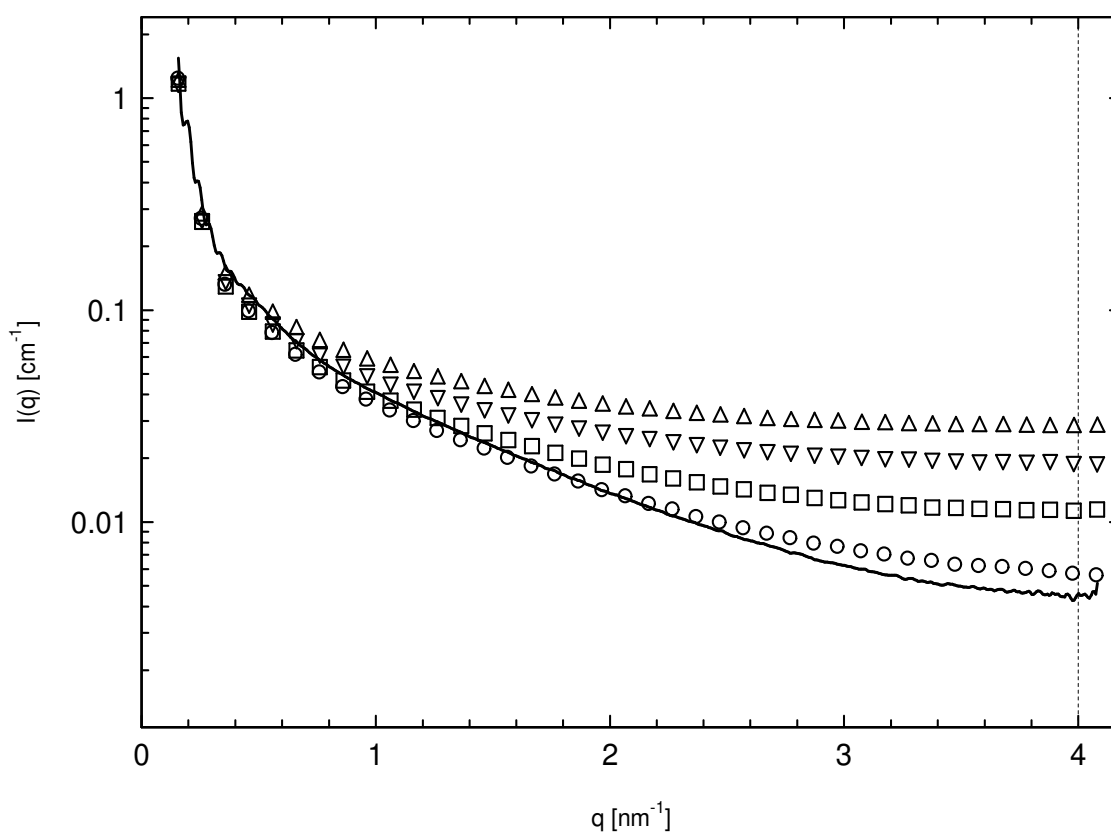


Fig. 3.5 shows the correction of fluorescence of spherical polyelectrolyte brushes (6.5 wt %) with Rubidium counterions at  $\text{pH}=10$ . The scattering intensity  $I(q)$  measured for different energies  $E$  of the incident radiation is plotted as the function of  $q$  at detector position  $2m$ . The solid line refers to  $E=15100 \text{ eV}$ , where contributions of the fluorescence can be neglected. Circles:  $15192 \text{ eV}$ ; squares:  $15196 \text{ eV}$ ; filled circles:  $15198 \text{ eV}$ ; empty triangles:  $15200 \text{ eV}$ .

From Fig. 3.6 it can be clearly seen that after the correction for the contributions of fluorescence from the scattering intensities, the effects at high  $q$ -values vanish and all the scattering intensities overlap over each other.

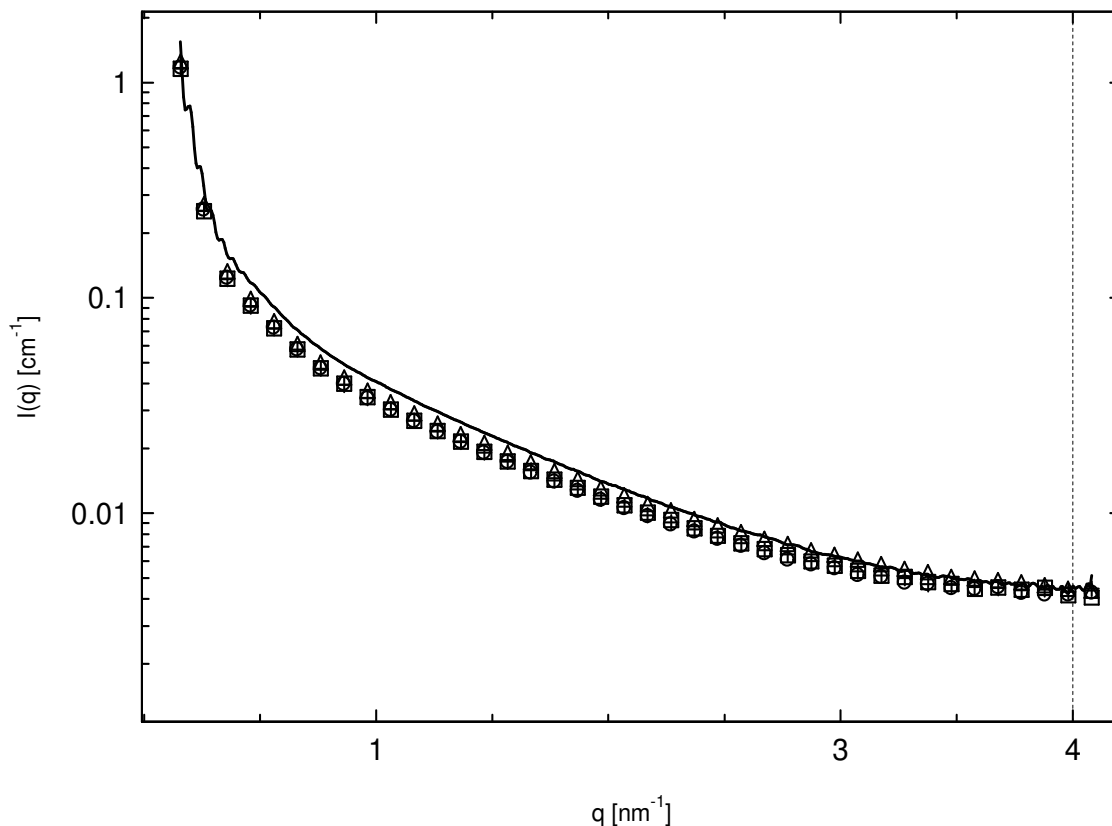


Fig. 3.6 shows the scattering intensities obtained of spherical polyelectrolyte brushes (6.5 wt. %) with Rubidium counterions at  $pH=10$  after the subtraction of the fluorescence contribution using the method described in Section 3.2.5. The solid line refers to the scattering intensity used as a reference curve ( $E= 15100$  eV); The markers represent the scattering intensities after the fluorescence subtraction. Triangles ( $E= 15192$  eV); Crosses ( $E=15196$  eV); Squares ( $E= 15198$  eV); Circles ( $15200$  eV) (Data points have been reduced for the sake of clarity)

### 3.2.6 Edge Localization

The experimental energies measured by synchrotron radiation differ slightly as compared to their theoretical values due to the backlash of the monochromator. This small shift needs to be taken into account for the determination of the true energy of the incident beam. The experimental energies were determined by locating exactly the energy of edge by measurement of the absorption of each sample. All the experimental intensities were then corrected for this small shift in the energy. This procedure was done for each sample measured in the course of this work.

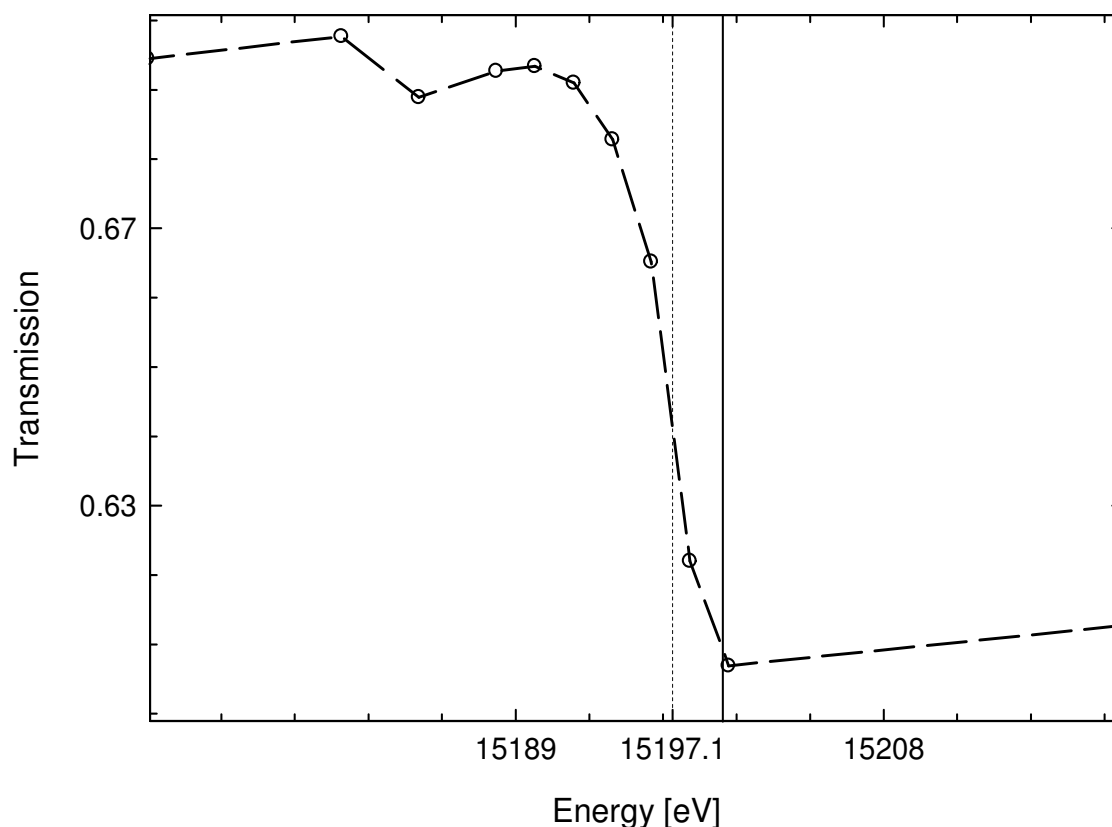


Fig. 3.7 displays a typical example of the transmission of a spherical polyelectrolyte brush solution (6.5 wt %) consisting of  $Rb^+$  counterions as a function of the energy of the incident beam. The solid line marks the theoretical value of the energy of the edge (15199.7 eV), while the dashed line represents the experimental edge determined as described in Section 3.2.6. The markers denote the transmission of the sample measured as a function of energy.

### 3.2.7 Effective scattering factors $f'_{eff}$ and $f''_{eff}$

As discussed in detail in the previous Section 3.2.6 (See Fig. 3.4), a finite width of the primary beam and the range of energies probed by a given position of the monochromator is not infinitely small [Patel et al. 2004; Dingenouts et al. 2004]. Hence it is necessary to correct for this effect by defining the effective scattering factors  $f'_{eff}$  and  $f''_{eff}$ . The effective scattering factors  $f'_{eff}$  and  $f''_{eff}$  results from a convolution of the energy spread of the primary beam with  $f'$  or  $f''$  respectively. Following Table (3.1) summarizes all data obtained by this procedure for measurements carried out on spherical polyelectrolyte brushes. In this way a small but significant correction is effected if  $E$  is in the immediate vicinity of the edge. For larger distances this correction is negligible as can be seen from Table (3.1). In the following work, the effective quantities  $f'_{eff}$  and  $f''_{eff}$  were solely used.

$\Delta E$	$f'$	$f'_{eff}$	$f''$	$f''_{eff}$
-2737.1	-1.41	-1.41	0.74	0.74
-397.1	-3.08	-3.08	0.54	0.54
-197.1	-3.75	-3.75	0.53	0.53
-97.1	-4.44	-4.44	0.52	0.52
-47.1	-5.17	-5.17	0.52	0.52
-27.1	-5.73	-5.73	0.51	0.51
-17.1	-6.20	-6.21	0.51	0.51
-13.1	-6.47	-6.49	0.51	0.51
-9.1	-6.87	-6.88	0.51	0.51
-7.1	-7.15	-7.18	0.51	0.51
-5.1	-7.58	-7.60	0.51	0.53
-3.1	-8.01	-8.34	0.51	0.88
-1.1	-10.06	-9.69	0.51	2.23

TABLE (3.1): Scattering factors  $f'_{eff}$  and  $f''_{eff}$

<sup>a</sup> Difference of the energy of the incident beam to the absorption edge in eV; <sup>b</sup> Real part of the scattering factor  $f$ ; <sup>c</sup> Effective real part of the scattering factor  $f$ ; <sup>d</sup> Imaginary part of the scattering factor,  $f$ ; <sup>e</sup> Effective imaginary part of the scattering factor  $f$ .

## **4 Results and Discussion**

In the following, results obtained from the studies of rod-like polyelectrolytes, spherical polyelectrolyte brushes and star polyelectrolytes using small angle x-ray scattering method namely, Anomalous Small-Angle X-ray Scattering (ASAXS) would be presented along with osmometry studies of rod-like polyelectrolytes.

### **4.1 Rod-like Polyelectrolytes**

The rod-like polyelectrolytes used in this work consist of a poly(p-phenylene) backbone. Onto each monomer unit two n-hexyl spacer groups are attached, the ends of which bear a charged ammonium group. The counterion can be chlorine, bromine or iodine. The counterions are replaced using counterion replacement technique. The method of counterion replacement allows us to study the effect of different counterions in polyelectrolyte solutions [Wittmann et al. 2000]. Such systems were synthesized by the synthetic route described in literature [Rehahn et al. 1988, 1989, 1990; Wittmann et al. 2000]. These systems have been studied previously in our group using SAXS [Guillaume et al. 2001] and osmometry measurements [Blaul et al. 2001].

Depending on the number of charges per monomer unit the charge parameter can also be varied. However, the systems studied in this work all carried two charges per monomer unit bearing a charge parameter  $\xi=3.3$ . As discussed earlier, the synthetic route undertaken here is first the synthesis and characterization of the uncharged polymer using N.M.R spectroscopy. After the molecular weight determination, the uncharged polymer is converted into polyelectrolyte through a number of synthetic steps described in the synthesis section. The polyelectrolyte is then purified using the ultrafiltration technique. From the synthetic route the polyelectrolyte bearing iodide ions is obtained which can then be replaced by chloride or bromide ion depending on requirement using counterion replacement technique by ultrafiltration with 0.02 M salt solution of the respective counterion (eg. KCl, KBr).

In this work rod-like polyelectrolytes with chloride, bromide and iodide counterions were studied by osmometry and only polyelectrolyte containing bromide were studied using ASAXS, since the absorption edge of bromine is ideal to be studied by synchrotron radiation.

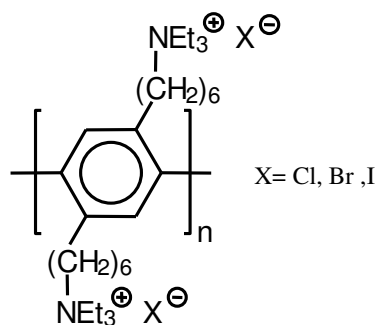


Fig. 4.1 shows Chemical representation of Poly (p-phenylene) polyelectrolytes with two charged groups on each monomer unit, where X = I, Br, Cl counterion.

	<b>PPP-2Br</b>
$M_0$ / g/mol	604
$\eta_e$ / e-/monomer unit	320
$l$ nm	0.43
$M_n$ g/mol	32044
$P_n$	53
$L_P$ / nm	23
$V_P$ / cm <sup>3</sup> /g	0.834
$\xi$	3.3

Table. 4.1 summarizes some of the characterization properties of Poly(p-phenylene) polyelectrolytes having bromide as counterion  $M_0$ : Molecular weight of each monomer unit with bromine counterion in g/mol,  $\eta_e$ : is the number of electrons per monomer unit in electrons,  $l$ : is the length of the monomer unit in nm,  $M_n$ : is the number-average molecular weight in g/mol,  $P_n$ : is degree of polymerization, is the persistence length  $L_P = l * P_n$ ,  $V_P$ : is the partial specific volume of the polymer in cm<sup>3</sup>/g calculated from the experimental data of density measurements and  $\xi$  is the charge parameter at 25 °C.



### 4.1.1 Osmotic Coefficient of Rod-like Polyelectrolytes

In this thesis, the osmotic coefficient of rod-like polyelectrolytes bearing different counterions namely, chloride, bromide and iodide is studied using membrane osmometry and compared to theoretical PB-cell model. The osmotic coefficient of a polyelectrolyte is defined through the ratio of the real and ideal osmotic pressure, where the ideal osmotic pressure for any solution is calculated through the counterions.

If  $c_p$  is the concentration of the polyelectrolyte then the reduced osmotic pressure  $\frac{\Pi}{c_p}$  is given as:

$$\frac{\Pi}{c_p} = \frac{h\rho g}{c_p}$$

$h$  is the height of the water column,  $\rho$ , the density of water ( $1000 \text{ kg.m}^{-3}$ ),  $g$  is the gravitational constant ( $9.81 \text{ m.s}^{-2}$ ) and  $c_p$  the polymer concentration in  $\text{g/L}^{-1}$ .

The osmotic coefficient is then described through van't Hoff law :

$$\phi = \frac{\Pi}{c_c RT} = \frac{\Pi}{c_p} \frac{M_m \nu}{RT \zeta}$$

where  $\frac{\Pi}{c_p}$  is the reduced osmotic pressure in  $(\text{PaLg}^{-1})$ ,  $c_c = \frac{c_p \zeta}{M_m \nu}$  is the counterion concentration in  $\text{mol.L}^{-1}$ ,  $M_m$  is the molecular weight of each repeating monomer unit in  $\text{gmol}^{-1}$ ,  $\zeta$  is the number of charged groups per monomer unit and  $\nu$  the valence of the counterion.

For the osmotic coefficient measurements of poly (p-phenylene) polyelectrolytes, symmetric membranes of cellulose acetate with a cut-off 5000 Dalton supplied by SARTORIUS were used. These membranes are coated with glycerine and other additives to protect them from drying and microbial degradation. Before using, the membranes are placed in Millipore water for approximately 1 day prior to their use. The water is then replaced every 2 hours with fresh Millipore water to free the membranes from any rest additives. Once immersed in water the membranes are always stored under water to prevent the drying and clogging of membranes. Special care is to be taken while performing osmotic pressure measurements using Membrane Osmometer. Even very small quantities of low molecular weight material can permeate through the membrane and result in erroneous results due to the high sensitivity of the Membrane Osmometer [Reddy, Marinsky 1970; Blaul 2001].

To purify the polyelectrolytes, approximately 100-150 mg of freeze-dried polyelectrolyte is taken in an ultrafiltration cell with a regenerated cellulose membrane with Cut-off of 30,000 Dalton and ultra filtered with approximately 25 liters of Millipore water under a nitrogen pressure of 1 bar.

The polyelectrolyte solution is purified until the conductivity of the outgoing serum is less than 1  $\mu\text{S}/\text{cm}$ . After the purification of the polyelectrolyte solution is concentrated to approximately 25 ml by concentrating in the ultrafiltration cell.

Care should be taken while concentration, since the conductivity of the outgoing serum increases as the solution is concentrated. After concentration, the solid content of the solution is determined and this solution is taken as the stock solution. All solutions are prepared by dilution of this stock solution.

All the measurements are carried out in a temperature regulated room at temperature of 25<sup>0</sup>C. As described in literature [Blaul 2001], the measurements are also followed by the help of plotter to determine whether small quantities of small molecular weight material are permeating through the membrane.

The results obtained by osmotic pressure measurements shown in Fig. 4.2. confirm that only about 20 % of the counterions are contributing to the osmotic pressure of the system while approximately 80 % of the counterions are 'condensed' to the macroions. The small dotted line is calculated osmotic coefficient from Manning theory of counterion condensation has a value of 0.15, while the long dashed line pertains to the Poisson-Boltzmann Cell Model for a charge parameter  $\xi=3.3$ .

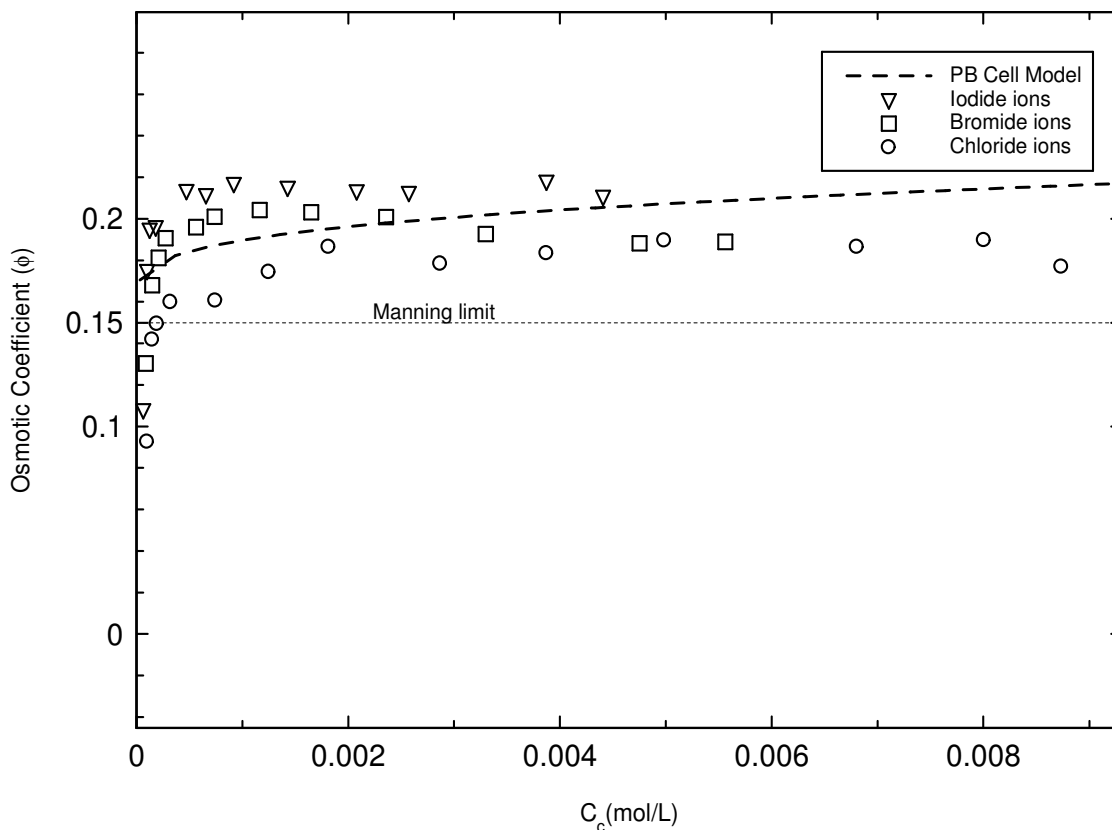


Fig. 4.2 shows the comparison of osmotic coefficient measurements for PPP in water at 25 °C, circles: chloride ions, squares: bromide ions, triangles: iodide ions, long dashed line: theoretical osmotic coefficient calculated using PB-Cell Model, short-dashed line: Manning limit.

Since the osmotic coefficient is only slightly dependent on the radius of the macroion, the comparison of the experimental data with the theoretical PB Cell model proceeds without any fit parameter. Results obtained here are in agreement with the Poisson-Boltzmann Cell Model semi-quantitatively within the limits of experimental error. The comparison proceeds without any need for the adjustment of charge parameter.

The osmotic coefficient measurements carried out on stiff-chain polyelectrolytes with chloride, bromide and iodide counterions is shown in Fig. 4.2 from which it is evident that the osmotic coefficient remains a constant at low concentrations. In contrast to the theory which does not take into account the specific effects of counterions [Manning 1984], a clear difference is evident in the measurements with various counterions. Experimental results for different counterions have shown that the interactions between counterions and macroion can lead to a reduction in the osmotic pressure [Mandel 1988; Katchalsky 1971]. Titration

experiments on polyacrylic acid also suggest that the size of the counterions does play a significant role in the counterion activity [Kagawa et al. 1957]. On the other hand numerical calculations suggest that the presence of even extremely small quantities of salt has a very large effect on the osmotic coefficient values [Deserno et al. 2001]. This leads to an uncertainty whether the specific interactions of the counterions or the salt has a stronger influence on the osmotic coefficient values obtained experimentally.

The results obtained in this study are in qualitative agreement with earlier measurements carried out on such systems [Alexandrowicz 1969; Blaul 2001]. The results also confirm that the Manning theory overestimates the counterion condensation remarkably. From Fig. 4.2 it can be seen that the Poisson-Boltzmann model though seems to underestimate the osmotic coefficient for the chloride ions, but is well in agreement in the case of bromide and iodide counterions.

The problem of the discrepancy between the experimental results and the PB-Cell model can arise from the assumption that the solvent is treated as a continuous dielectric background. Hydration effects are also ignored in PB-Cell model. The rods are considered to be infinitely long. However, the finite size of the macroion can lead to an increase in the osmotic coefficient [Deserno et al. 2001]. Molecular-Dynamics Simulations have shown that the simulations which took into consideration the correlation effects between the macroion and the counterion showed a reduction in the osmotic coefficient. The osmotic coefficient did not reduce significantly enough to explain the experimental data [Blaul 2000]. A significant deviation from the theory is observed for the osmotic coefficient values presented in Fig. 4.2 suggesting the correlation to be concentration-dependent at increased polyelectrolyte concentrations. Such a behavior was also observed in earlier Osmotic coefficient measurements [Blaul 2000].

## 4.2 Anomalous Small Angle X-ray Scattering (ASAXS)

### 4.2.1 Rod-like Polyelectrolytes

As already discussed in Section 2.4, rod-like polyelectrolytes are described using the well-known Poisson-Boltzmann Cell Model. The macroions are placed in cylinders parallel to each other with counterions surrounding them. For cylindrical objects in which the scattering length density varies only along the radial distance ( $r_c$ ). The scattering of the macroion can be modelled in terms of a real excess electron density  $\Delta\rho_{rod}$ . With  $a$  being the minimum approach of the macroion and the counterions, it follows that the radial excess electron density  $\Delta\rho(r_c) = \Delta\rho_{rod}$  for all  $r_c \leq a$ .

For  $r_c \geq a$ ,  $\Delta\rho(r_c)$  is solely determined by the excess electron density of the counterions. Evidently, the integration in Equation. (2.78) must include all counterions otherwise the condition of electro neutrality would be violated [Guilleaume et al. 2000, 2001].

For ions immersed in a medium of scattering length density  $\rho_m$ , the contrast per ion can be given as :

$$\Delta\rho_{ion} = \frac{f}{V_{ion}} - \rho_m \quad (4.1)$$

where  $V_{ion}$  is the volume of the ion, and  $\rho_m$  the contrast of the surrounding medium.

If  $n(r_c)$  denotes the radial number density of the counterions. The distribution function  $n(r_c)$  can then be calculated according to the Poisson-Boltzmann Cell model [Le Bret et al. 1984; van der Maarel et al. 1992,1997,1998]. In this theory the radial distribution  $n(r_c)$  is calculated according to the mean-field approximation that takes into account the variation of the scattering length along the radial distance ( $r_c$ ).

For  $r_c \geq a$ ,  $\Delta\rho(r_c)$  can be given as:

$$\Delta\rho(r_c) = \Delta f_{ion} n(r_c) \quad (4.2)$$

where  $\Delta f_{ion}$  is the number of excess electrons of a single ion. This quantity is given by [Guilleaume et al. 2001]:

$$\Delta f_{ion} = f_0 - \rho_m V_{ion} + f' + \tilde{f}'' \quad (4.3)$$

where  $f_0$  it's non-resonant scattering factor,  $f'$  and  $f''$  are the real and the imaginary part of the energy-dependent scattering factor [Stuhrmann 1985] respectively, while  $\tilde{i}$  is the imaginary unit. The respective scattering lengths are obtained by multiplication of these quantities by the Thomson factor  $r_0$  [Porod 1982; Stuhrmann 1985].

For the calculation of the SAXS-intensity measured far away from the absorption edge only  $f_0$  is taken into account. Only if measurements are conducted in the immediate neighbourhood of the absorption edge of the counterions, the contributions due to  $f'$  and  $f''$  become important and must be taken into account [Stuhrmann 1985].

The excess electron density to be introduced into Equation (2.78) follows as:

$$\Delta\rho(r_c) = \begin{cases} \Delta\rho_{rod} & 0 \leq r_c \leq a \\ n(r_c)\Delta f_{ion} & a \leq r_c \leq R_0 \\ 0 & r_c > R_0 \end{cases} \quad (4.4)$$

Here  $R_0$  denotes the cell radius introduced by the Poisson-Boltzmann cell model (Section. 2.4).  $\Delta\rho(r_c)$  may therefore be split into a non-resonant term  $\Delta\rho_0(r_c)$  and the resonant contributions of the counterions [Guillaume et al. 2002]

$$\Delta\rho(r_c) = \Delta\rho_0(r_c) + n(r_c)f' + \tilde{i}n(r_c)f'' \quad (4.5)$$

where  $\tilde{i}$  is the imaginary unit. Insertion of Equation (4.5) into Equation (2.78) and Equation (2.80) leads to three terms that are related to the Hankel-transforms of the terms  $\Delta\rho_0(r_c)$ ,  $n(r_c)f'$  and  $n(r_c)f''$  respectively: [Guillaume et al. 2001]

$$F(q, \alpha)F^*(q, \alpha) = \left( L \frac{\sin(q\alpha L/2)}{q\alpha L/2} \right)^2 \left\{ F_{cr}^2[\Delta\rho_0(r_c), q, \alpha] + 2f'F_{cr}[\Delta\rho_0(r_c), q, \alpha]F_{cr}[n(r_c), q, \alpha] \right. \\ \left. + (f'^2 + f''^2)F_{cr}^2[n(r_c), q, \alpha] \right\} \quad (4.6)$$

Hence, ASAXS leads to three partial intensities: The first term  $F_{cr}^2[\Delta\rho_0(r_c), q, \alpha]$  in the curved brackets leads to the usual SAXS-intensity measured far away from the absorption edge and is only dependent on the  $f_0$ . The additional terms give the modification of  $I_0(q)$  in the vicinity of the absorption edge. The second term is the cross-term emanating from the energy-

independent part of the scattering amplitude  $F_{cr} [\Delta\rho_o(r_c), q, \alpha]$ , the third-term is known as the self-term of the counterions  $F_{cr} [n(r_c), q, \alpha]$ . The self-term is the energy-dependent part of the scattering amplitude and depends on the real dispersive scattering factor  $f'$ . In many cases the cross term (second term of Equation (4.6)) is the dominating term in ASAXS. The self-term (third term of Equation (4.6)) may be dominant if the contrast of the macroion is small.

As discussed in Section 2.6.2, Equation (4.6) can be simplified for  $q > \frac{1}{L}$ . In this case the main part of scattering of a rod-like object results if  $q$  is perpendicular to the long axis of the rod and when  $\alpha = 0$ , as shown in Equation (2.81) [Guilleaume et al. 2001].

As already discussed in Section 2.4, the Poisson-Boltzmann Cell Model treats the system to be an assembly of  $N$  rods placed in cells of radius  $R_o$ . The cell radius is determined by the geometry of a cylinder  $(N/V)\pi R_o^2 L = 1$ .

The distribution function  $n(r_c)$  can be calculated from PB cell model as:

$$\frac{n(r_c)}{n(R_o)} = \left( \frac{2|\beta|}{\kappa r_c \cos[\beta \ln(r_c / R_M)]} \right)^2 \quad (4.7)$$

using known parameters  $\xi$  the charge parameter, 'a' the radius of the macroion and  $R_o$  the cell radius, the first integration  $\beta$  can be calculated by:

$$\arctan\left(\frac{\xi-1}{\beta}\right) + \arctan\left(\frac{1}{\beta}\right) - \beta \ln\left(\frac{R_o}{a}\right) = 0 \quad (4.8)$$

The second integration constant,  $R_M$  which is assumed to be the radial distance where counterions are condensed can be calculated using the following equation.

$$R_M = a \exp\left[\frac{1}{\beta} \arctan\left(\frac{\xi-1}{\beta}\right)\right] \quad (4.9)$$

The distribution function obtained for a given number density  $N/V$  is then further used to calculate the respective scattering intensity according to Equation (2.80) and Equation (4.6).

The analysis of the data obtained for rod-like polyelectrolytes follows as discussed in Chapter 3, first the exact position of the absorption edge is determined from the measurements of the transmission [Dingenouts et al 2003].

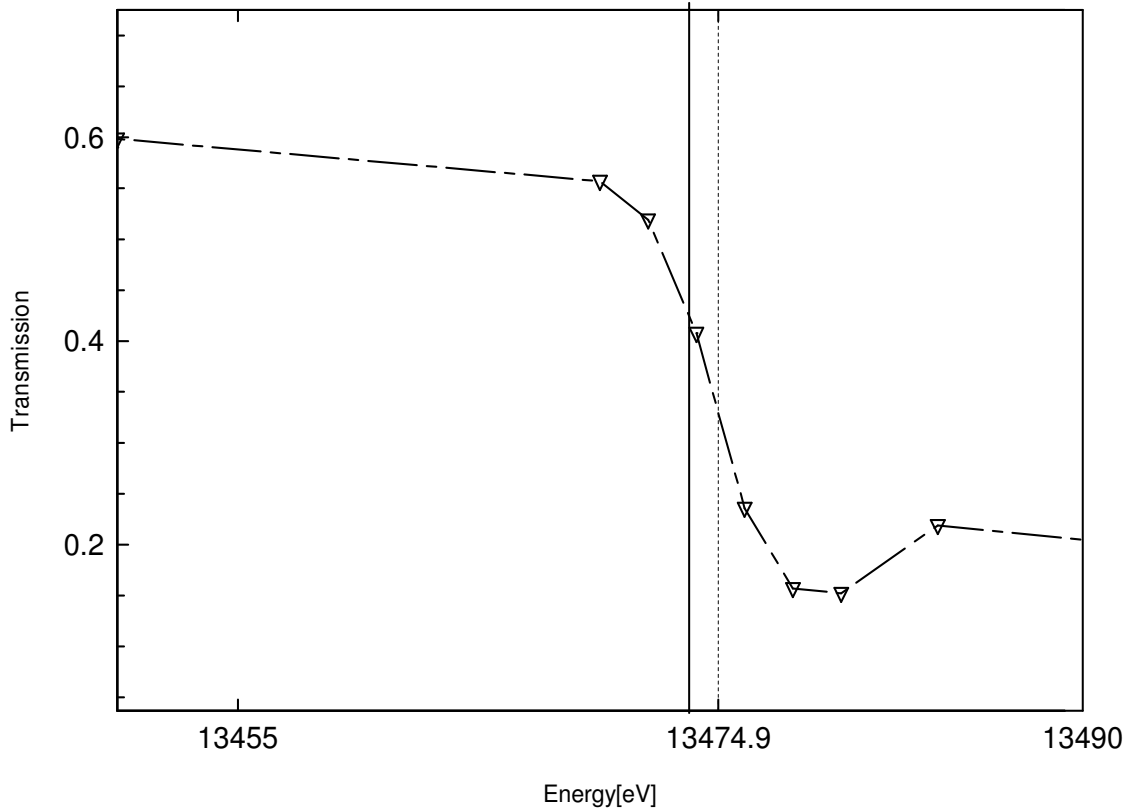


Fig. 4.3 shows the transmission of KBr solution as a function of the energy of the incident beam. The dashed line marks the point of inflection taken as the correct energy of the absorption edge; solid line denotes the theoretical absorption edge for Bromine.

As is evident from Fig. 4.3, there is a small shift as compared to the value of the literature [Henke et al. 1993; Brennan et al. 1992]. This shift is corrected for all the subsequent calculations as described in Section 3.2.6. In the course of this work, therefore only  $\Delta E$  from the absorption edge is given. Secondly the problem of the finite width of the energy distribution of the primary beam also needs to be taken into consideration. The finite width is taken into account by the calculation of the effective scattering factors  $f'_{eff}$  and  $f''_{eff}$  [Dingenouts et al. 2003]. This is done by weighing the respective scattering factors by the profile of the primary beam shifted to the respective energy. Table (4.2) shows the data



obtained by carrying out this procedure. This correction is only important in the immediate vicinity of the absorption edge.

Table (4.2): Scattering factors  $f'$  and  $f''$

$\Delta E^a$	$f'^b$	$f_{eff}'^c$	$f''^d$	$f_{eff}''^e$
-1014.9	-2.23	-2.23	0.61	0.61
-74.9	-4.75	-4.75	0.54	0.54
-2.9	-8.38	-8.38	0.53	0.55
-0.9	-10.11	-9.88	0.53	1.25
1.1	-9.62	-9.72	3.86	3.30
3.1	-8.14	-8.28	3.86	3.85

*a: Difference of the energy of the incident beam to the absorption edge in eV.*

*b: Real part of the scattering factor  $f$ .*

*c: Effective real part of the scattering factor  $f$ .*

*d: Imaginary part of the scattering factor  $f$ .*

*e: Effective imaginary part of the scattering factor  $f$ .*

(See Section 3.2.7)

The finite width of the primary beam is also related to the fluorescence which becomes important as the absorption edge is approached [Dingenouts et al. 2003]. A part of the beam profile is already localized above the edge which leads to fluorescence which can be seen through a background. This additional contribution is independent of the scattering angle. Fig. 4.4 demonstrates that this effect comes into play in the immediate vicinity of the absorption edge.

In Fig. 4.4, the background scattering by the capillary and water has not been removed. The highest energy (13478 eV) lies slightly above the edge which leads to an increase of the background due to fluorescence. Fig. 4.4 shows that the scattering beyond  $q= 3.5 \text{ nm}^{-1}$  is independent of  $q$ . Therefore, in this region the measured intensity is fully dominated by the background as the scattering of capillary, water and fluorescence. Unlike colloidal suspensions, the scattering intensity emanating from dissolved macromolecules is much smaller. Hence, the total background needs to be determined carefully and subtracted for each scattering curve. Therefore, the entire parasitic scattering which comprised of the

capillary, water as well as fluorescence was removed from the data as already demonstrated by Fig. 3.1 in Section 3.1.2.

The above discussion has shown that the problem of the removal of the background scattering is more difficult for rod-like polyelectrolytes than in case of colloidal dispersions. The forward scattering intensity normalized to the unit concentration scales with the molecular weight and the much smaller masses that are of the order of  $10^4$  g/mol lead to concomitantly smaller intensities.

The decrease of  $I(q)$  with  $q$ , however, scales only with  $q^{-1}$  instead of the final slope  $-4$  observed in the case of colloidal spheres. Fig. 4.5 demonstrates that, indeed reasonable data were obtained up to  $q \approx 3 \text{ nm}^{-1}$ . Moreover, the shift of  $I(q)$  toward smaller values with decreasing  $\Delta E$  predicted by Equation (4.6) is indeed seen by ASAXS.

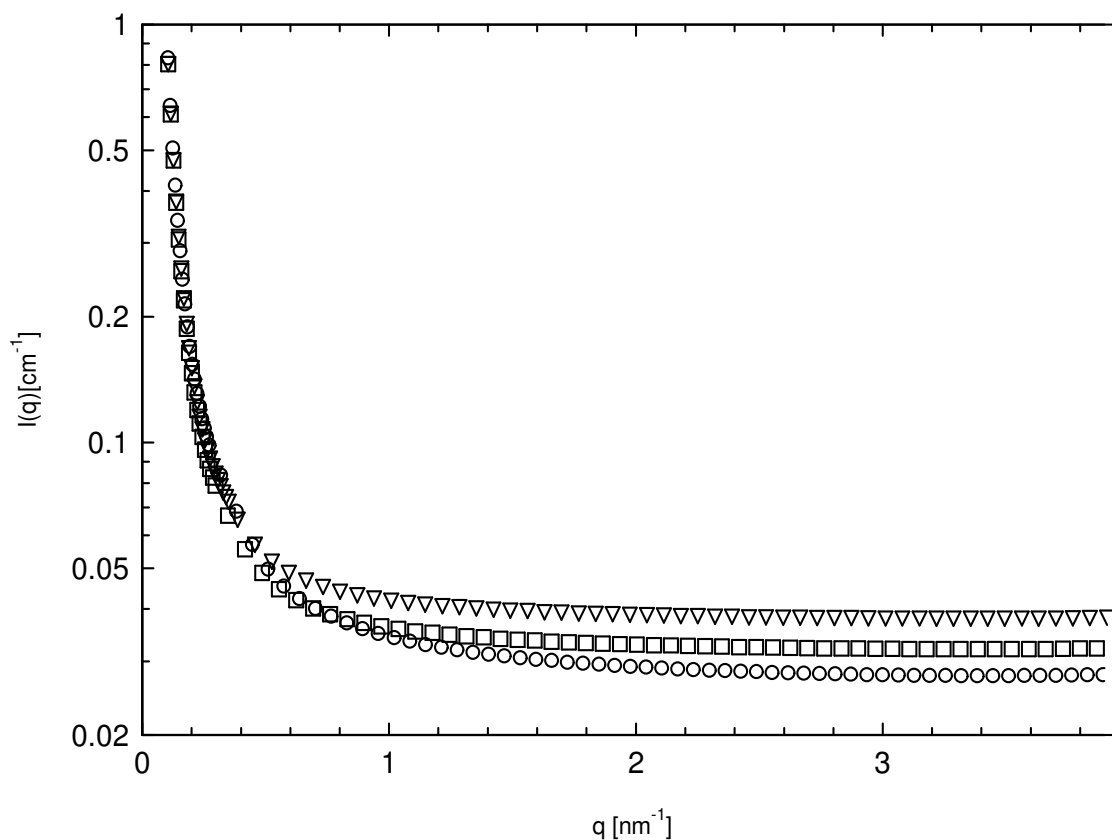


Fig. 4.4 displays the resulting scattering intensities measured at different energies of the incident beam. Dependence of the measured intensities on the energy of the incident beam is shown here. For the sake of clarity only three different energies are shown here. However for the evaluation procedure all the six different energies shown in Table. 4.5 have been used. Circles:  $\Delta E = -1014.9$ ; Squares:  $\Delta E = -0.9$ ; Triangles:  $\Delta E = 1.1$

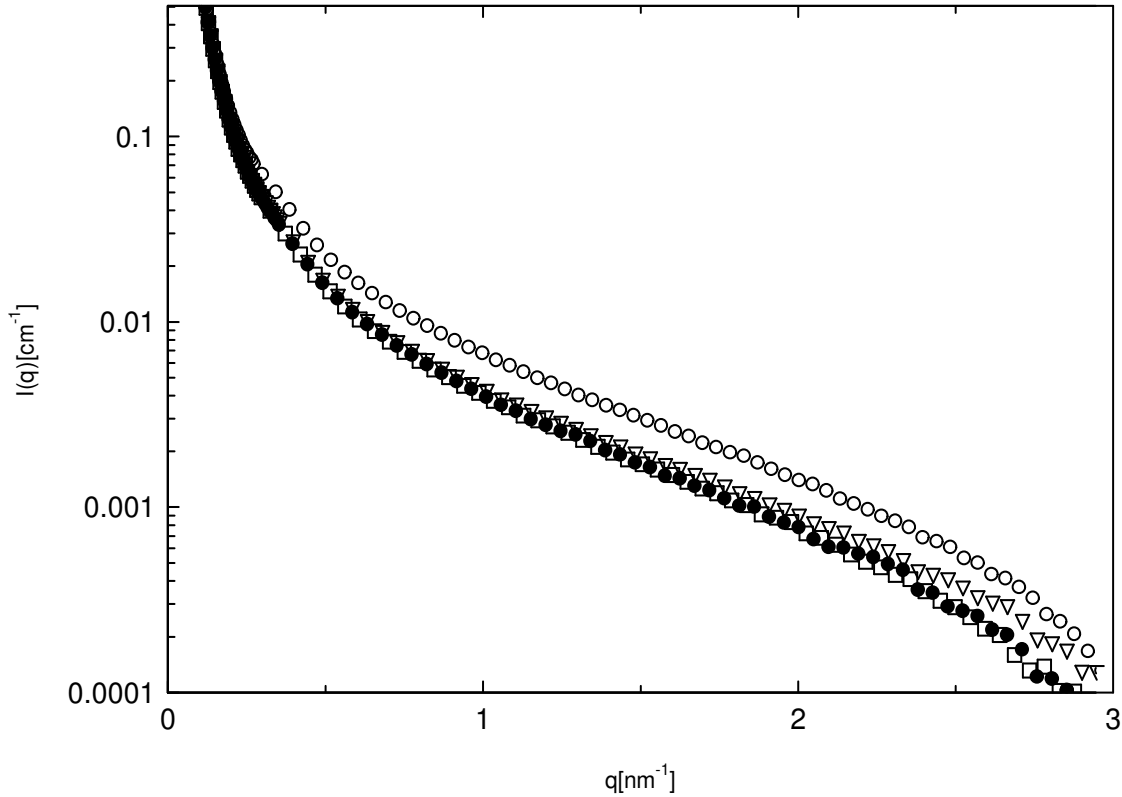


Fig. 4.5 shows the scattering intensities at different energies after correction for the fluorescence and the solvent water and empty capillary. The difference of the energy of the incident beam from the edge is indicated in this Figure. The subtracted procedure used is as described in Section. 3.1.2 and demonstrated by Fig. 3.1. Circles:  $\Delta E = -1014.9$ ; Triangles:  $\Delta E = -2.9$ ; Squares  $\Delta E = -0.9$ ; Filled Circles:  $\Delta E = 1.1$

The present procedure removes also all possible contributions from the longitudinal fluctuations of the counterions. These fluctuations come into play for highly charged macroions and give an additional contribution to the measured intensity [Guilleaume et al. 2002]. Because of the mean-field approximation, the counterions are not treated as single entities from which the scattered radiation emanates but as a distribution of counterions homogenous along the long axis of the rod. This mean field approximation is not valid however, if  $\frac{2\pi}{q}$  is much large than the average distance between the counterions [Guilleaume et al. 2002]. Hence, if the contrast of the system is high enough the fluctuations of the local number density of the ions also become visible in any scattering experiment. Since the polyelectrolyte consists of two counterions as opposed to the four counterions per monomer

unit [Guillaume et al. 2002]. A significant contribution due to the fluctuations of the counterions to the scattering intensity is not expected.

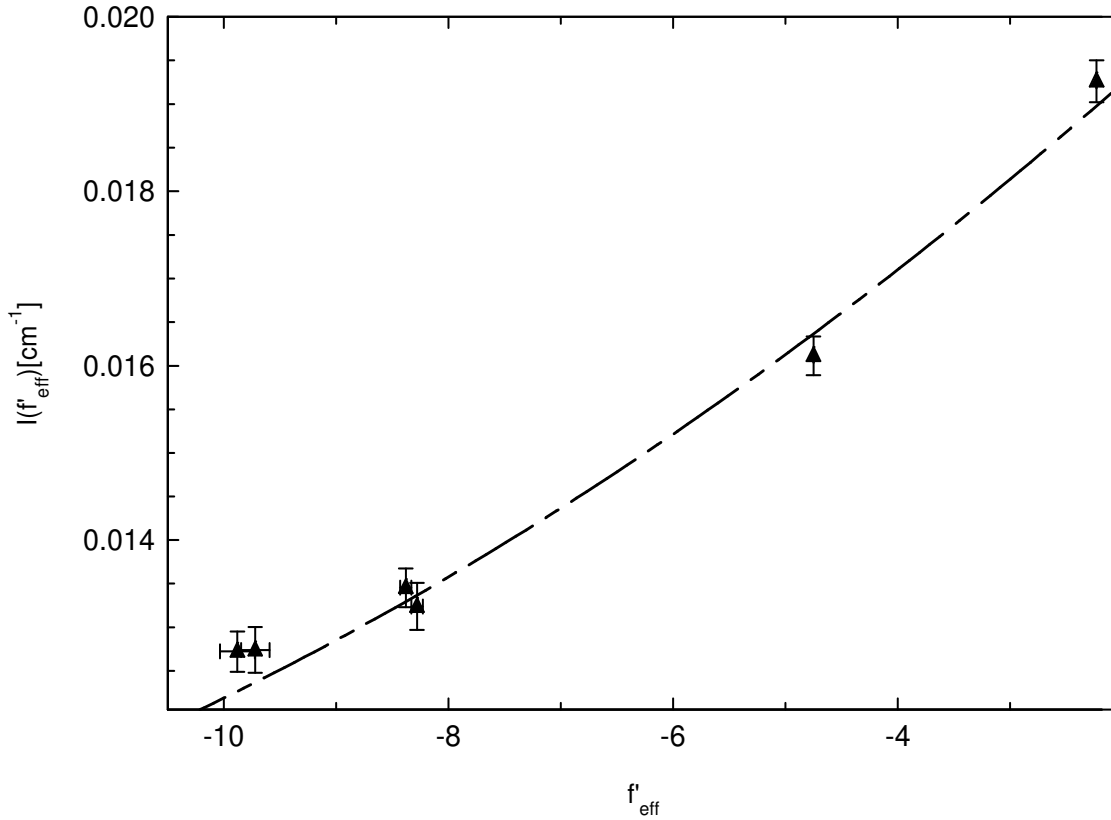


Fig 4.6 shows the Decomposition of the ASAXS intensities measured at different energies of the incident beam according to Equation (4.6). The intensities measured at a  $q$ -value shown in this Figure are plotted against the effective real part  $f'_{\text{eff}}$  is disregarded. The markers shown are obtained for  $q = 0.5494 \text{ nm}^{-1}$ .

Equation (4.6) shows that ASAXS leads to three partial intensities, namely the first term which contains the non-resonant scattering, the cross term and the third term that is solely due to the resonantly scattering units. The latter partial intensity named self-term is the most interesting result because it is the scattering intensity of the cloud of counterions only. All previous evaluations of ASAXS-data proceeded by subtracting the first, non-resonant term from the experimental data [Guillaume et al. 2001]. The non-resonant term can in principle be obtained through measurements far below the edge. Model calculations furthermore showed that the third partial intensity is small as compared to the cross term. Hence, this term was disregarded in previous ASAXS-studies of polyelectrolytes [Guillaume et al. 2001].

As already discussed in Section 3.2.7, since the finite width of the primary beam and the range of energies probed by a given position of the monochromator is not infinitely small [Patel et al. 2004; Dingenouts et al. 2004]. It is necessary to correct for this effect by defining the effective scattering factors  $f'_{eff}$  and  $f''_{eff}$ . The effective scattering factors  $f'_{eff}$  and  $f''_{eff}$  are calculated from a convolution of the energy spread of the primary beam with  $f'$  or  $f''$  respectively.

Subtracting two large terms in order to give a small difference is a numerically ill-posed problem. Therefore a different scheme for the general treatment of the ASAXS data is considered here: Equation (4.6) is a quadratic form in terms of the scattering factor  $f'$  if  $f''$  is disregarded. This approximation is certainly justified for data below the edge where  $f''$  is rather small indeed as depicted in Fig. 2.7. Hence, for each  $q$ -value the set of the 4 scattering curves measured below the edge as the function of solely  $f'_{eff}$  was used at first for the decomposition (see Table 4.2). While the above procedure is numerically much more stable, it disregards the data taken above the edge. Measurements at positive values of  $\Delta E$  however, impose no particular problem if the fluorescence is subtracted properly. As already discussed, the removal of the background caused by fluorescence provides no major difficulty. Moreover, measurements above the edge lead to a greater self-term because  $f''$  is not small anymore as is evident from Fig. 2.7. Therefore all data including the point above the edge were taken into account by the use of a non-linear fit procedure. This also takes into account that  $f''_{eff}$  already raised below the edge because of the finite width of the energy distribution of the primary beam as already discussed in Section 3.2.5 and demonstrated by Fig. 3.4 for spherical polyelectrolyte brushes. However, in the case of rod-like polyelectrolytes, it was found that inclusion of a finite  $f''_{eff}$  leads to the same result within the limits of error. Hence, the decomposition of Equation (4.6) can be done for the present set of data by neglecting  $f''_{eff}$ . Fig. 4.6 depicts the plot of  $I(q)$  as the function of  $f'_{eff}$ . For the sake of clarity only one set of data for a single value of  $q = 0.5494 \text{ nm}^{-1}$  is shown. The dashed line shows the fit of Equation (4.19) for  $q = 0.5494 \text{ nm}^{-1}$ . All the three partial scattering terms enumerated in Equation (4.19) can be obtained by repeating this procedure for all  $q$ -values under consideration. The range of  $f'$  covered by this analysis must be wide since the accuracy of the three partial scattering terms depends on the curvature of this plot. The dashed line in Fig. 4.6 displays the fit obtained for a given  $q$ -value for all energies including the data taken above the edge with neglect of  $f''_{eff}$ .

The present set of data is over determined and Fig. 4.3 allows to assess the accuracy of the procedure. The range of  $f'_{eff}$  is obviously sufficient to extract the linear and the quadratic term of Equation (4.6).

As expected from previous model calculations, the intensities exhibit a very similar dependence on  $q$  [Guilleaume et al. 2001]. The self-term which is much smaller than the non-resonant term or the cross term can be obtained up to  $q = 2.5 \text{ nm}^{-1}$ . As mentioned above, this term provides the most valuable information of the ASAXS-experiment. It refers to the scattering intensity that would result from a system in which the macroion is totally matched.

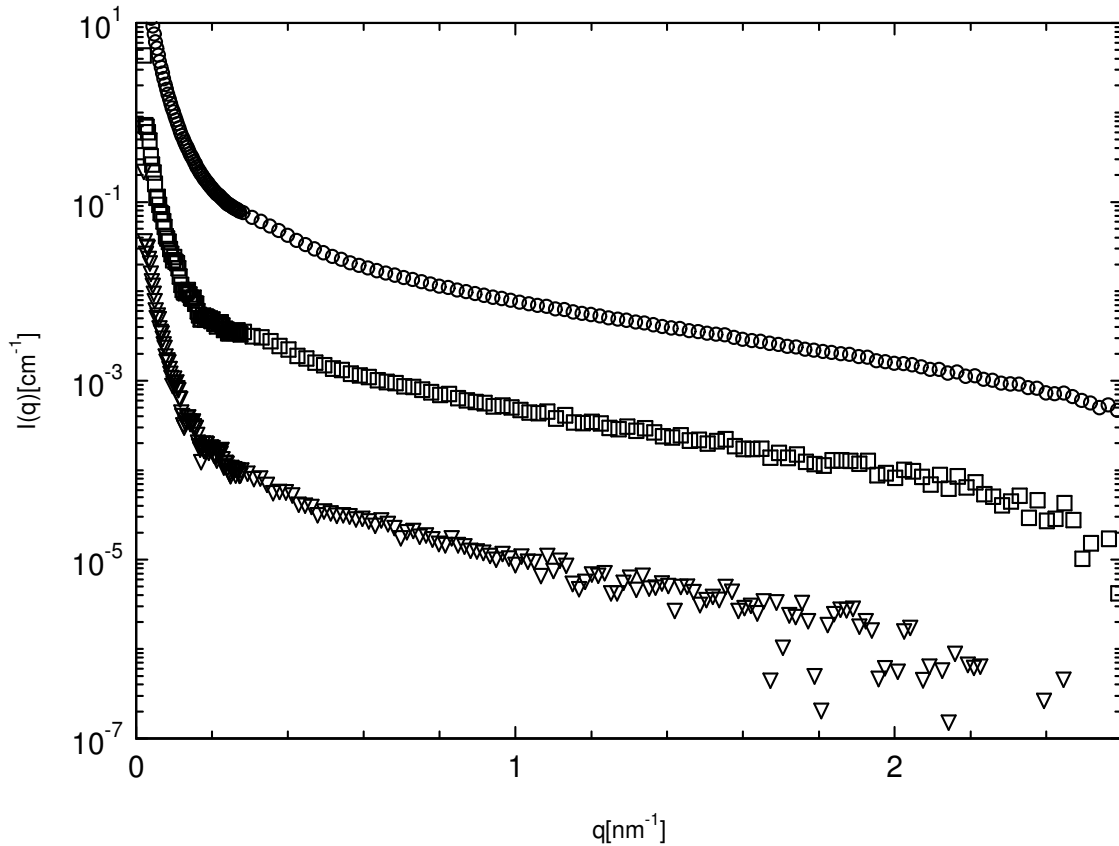


Fig. 4.7 displays the three partial intensities. Here the scattering intensity denoted by (circles) corresponds to the conventional SAXS-intensity measured far below the edge. The lowermost curve depicted by (triangles) is the self-term of Equation 4.6 and the curve in between marked by (squares) is the cross-term.

## 4.2.2 Comparison with the Poisson-Boltzmann Cell Model

Since the polyelectrolyte has already been studied by conventional SAXS, all parameters are taken from this work [Guilleaume et al. 2001]. The charge parameter  $\zeta$  is 3.3 which is determined through the chemical structure [Guilleaume et al. 2002]. The cell radius  $R_0$  is determined from the number density of the rod-like polyelectrolyte. Subsequently the integration constants  $\beta$  in Equation (4.8) and  $R_M$  Equation (4.9) are determined. The contrast  $\Delta f_{ion}$  of the  $Br^-$  counterion is determined from the crystallographic radii. The hydration shell of the ion is treated as bulk water. The value calculated in this way for  $Br^-$  is  $\Delta f_{ion} = 26 e^-/ion$ . For the contrast of the macroion the value  $\Delta \rho_{rod} = 25 e^-/nm^3$  is used [Guilleaume et al. 2000].

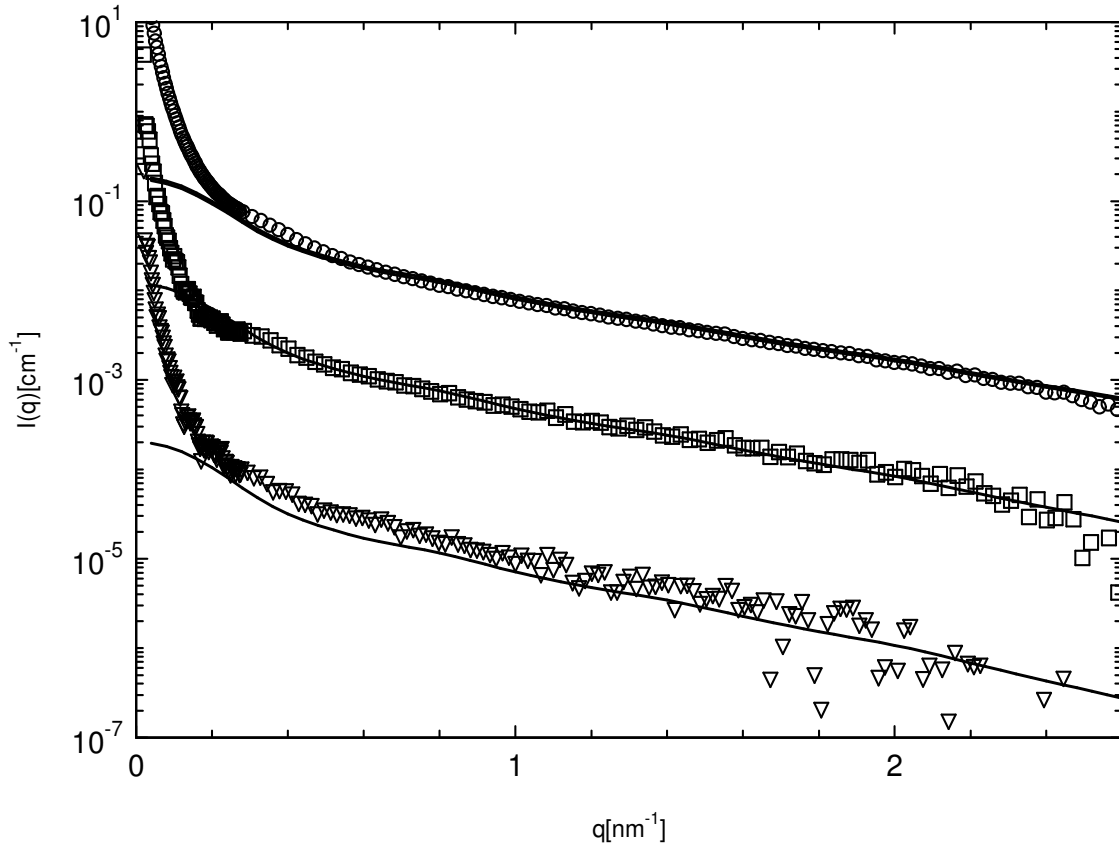


Fig. 4.8 The partial scattering intensities obtained by ASAXS are plotted against  $q$  and compared to the prediction of the cell model. Circles: is the first term of Equation (4.6) and related to the scattering intensity obtained far below the absorption edge. Squares: denote the cross-term in Equation (4.6). Triangles: refers to the self term which is solely due to the scattering contribution of the counterions. The solid lines mark the prediction of the cell mode as already discussed in Section. 4.2.1.

With the distribution  $n(r_c)$  the partial scattering intensities in Equation (4.6) can now be calculated and compared to the experimental data shown in Fig. 4.8. The solid lines in Fig. 4.8 show this comparison. For this comparison all theoretical intensities had to be multiplied by a factor of 2.3. This shift of the scattering curves can be assigned to the problem of absolute intensities in SAXS-measurements. However, the ratio of the respective partial intensity remained the same. Fig. 4.8 shows that good agreement is reached for all three partial intensities. All ratios between the intensities as well as their dependence on  $q$  are captured by the cell model. Only the self-term is slightly underestimated but the small differences seen in Fig. 4.8 are hardly beyond the experimental uncertainty.

More importantly, no additional adjustable parameter had been introduced into this comparison, because all parameters are either fixed or have been taken from a previous analysis as  $\Delta\rho_{rod}$ . Moreover, as is obvious from Equation (4.6), the self-term is not dependent on any contrast and is thus model-independent.

Only at the smallest  $q$ -values there is a discrepancy between theory and experiment. This upturn of  $I(q)$  has already been seen at smallest scattering angles in recent studies by conventional SAXS [Guilleaume et al. 2000, 2001, 2002]. This effect is also seen in solutions of flexible polyelectrolytes as well [Zhang et al. 2001] as in measurements carried out on DNA [Borsali 1998]. The reasons for this phenomenon are not yet clear, although the common interpretation is that it is due to the scattering of aggregates or clusters. The present data shows that the strong upturn is also seen for the self-term that is solely related to the counterions, as can be seen in the Fig. 4.7.

From these findings, it can be concluded that the three terms described by theory (Section 4.2) can be obtained efficiently by synchrotron radiation. Model calculations based on PB Cell Model describe the experimental data very well. ASAXS experiments can indeed be used to determine the contribution of the counterions to the total scattering intensity. The results have shown that, the counterions are strongly correlated to the macroion. To elucidate the effect further, studies using rod-like polyelectrolytes with a charge parameter  $\zeta < 1$  would be helpful.



### 4.3 ASAXS Studies of Spherical Polyelectrolyte Brushes

The method for the synthesis of spherical polyelectrolyte brushes studied in the course of this work was devised by Xuhong Guo [Guo et al. 1999]. The spherical polyelectrolyte brushes consist of a spherical polystyrene core onto which polyelectrolyte chains were grafted using ‘grafting from’ technique.

In this thesis, the polyelectrolyte chains grafted onto the polystyrene core were synthesized using acrylic acid as monomer. After the synthesis, the latex was purified by extensive ultra filtration to remove any free polyelectrolyte present in the serum. The characterization with regard to the contour length  $L_c$  and the grafting density was done using dynamic light scattering, disc centrifugation, TEM etc. The particles used in this study have a core diameter of 68 nm, weight-average contour length  $L_c = 233$  nm and a grafting density  $\sigma = 0.026$  nm<sup>-2</sup>. The  $Rb^+$  counterions were introduced by titration of the acidic particles by aqueous  $RbOH$ . Previous studies using dynamic light scattering have shown that all carboxyl-groups within the brush are converted by this procedure [Guo et al. 2000, 2001]. Studies carried out on spherical polyelectrolyte brushes by varying the pH of these systems showed that the brush length of brushes consisting of polyacrylic acid increased with increasing  $pH$ , suggesting the charging of the brush [Guo et al. 2000]. No additional salt was added to the system studied here. In order to ensure full ionization of the brush,  $RbOH$  was added until a  $pH$  of 10 was reached [Guo et al. 2001].

As has been already discussed in earlier Section.4.2.2, for the case of bromide ions of rod-like polyelectrolytes, the energy of the incident radiation was changed to reach the absorption edge of Rubidium (15199.7eV) from below. The macroion is made up from polystyrene core which does not exhibit any anomalous dispersion in the energy range used here.

The absolute scattering intensity  $I(q)$  is given by:

$$I(q) = \frac{N}{V} I_0(q) S(q) \quad (4.10)$$

where  $N/V$  is the number of dissolved particles per volume,  $I_0(q)$  is the scattering intensity of a single particle and  $S(q)$  is the structure factor. Since all the experiments carried out in the course of this study are in the dilute regime, the influence of  $S(q)$  is restricted to the region of smallest angles [Ballauff 2001]. Hence, in the following  $S(q) = 1$  which corresponds to a system of non-interacting particles.

Despite the spherical symmetry the scattering intensity  $I(q)$  is a complex quantity because the scattering factor of the rubidium ions has a non-vanishing imaginary part. As discussed earlier in Section. 2.5.3 by Equation (2.51), the scattering intensity is given through:

$$I_0(q) = F(q)F^*(q) \quad (4.11)$$

where  $F(q)$  is the complex scattering amplitude of a single particle. Because of the spherical symmetry of the particles  $F(q)$  follows as:

$$F(q) = 4\pi \int_0^\infty [\rho(r) - \rho_m] \frac{\sin qr}{qr} r^2 dr \quad (4.12)$$

where  $\rho(r)$  is the radial electron density of the spherical polyelectrolyte brush and  $\rho_m$  is the electron density of the surrounding medium water. The excess electron density  $\rho(r) - \rho_m$  consists of two parts: i) The contribution of the macroion, and ii) the contribution of the counterions which is complex.

### 4.3.1 Contrast of macroion

The macroion is composed of a poly(styrene) core having an excess electron density  $\Delta\rho_{core}$ . This contrast of poly(styrene) in water is small [Dingenouts et al. 1999] and the main contributions stems from the PAA-chains attached to the surface. With the radial excess electron density of the PAA-chains given by  $\Delta\rho_{PAA}(r)$ , the radial excess electron density of the macroion can be given as:

$$\begin{aligned} \Delta\rho_{macroion}(r) &= \Delta\rho_{core}; r \leq R_c \\ \Delta\rho_{macroion}(r) &= \Delta\rho_{PAA}(r); r > R_c \end{aligned} \quad (4.13)$$

where  $R_c$  is the radius of the core.

### 4.3.2 Complex contrast of counterions

As already discussed is previous Section 2.7 in conjunction with Equation. (2.82), the scattering factor  $f_{ion}$  becomes complex in the vicinity of the absorption edge. Both  $f'(E)$  and  $f''(E)$  are related to each other by the Kramers-Kronig relation.

As discussed above for the analysis of rod-like polyelectrolytes, if  $n_{ion}(r)$  be the number of counterions per unit volume within distance  $r$  from the center of the particle. Then the contribution of the counterions to the excess electron density of the entire particles is given by:

$$\Delta\rho_{ion}(r) = n_{ion}(r)\Delta f_{ion}; r \geq R_c \quad (4.14)$$

From these conditions it follows that the excess electron density of the spherical polyelectrolyte brush is given by:

$$\begin{aligned} \Delta\rho(r) &= \Delta\rho_{core}(r); r \leq R_c \\ \Delta\rho(r) &= \Delta\rho_{PAA}(r) + \Delta f_{ion}; r > R_c \end{aligned} \quad (4.15)$$

### 4.3.3 Calculation of $I_0(q)$ and of $v(q)$

The scattering amplitude  $F(q)$  is split into a non resonant term  $F_0(q)$  and an energy-dependent term  $F_{res}(q)$ :

$$F(q) = F_0(q) + F_{res}(q) \quad (4.16)$$

For the non-resonant term we obtain from Equation. (4.13):

$$F_0(q) = 4\pi \int_0^{\infty} \Delta\rho_{macroion} \frac{\sin qr}{qr} r^2 dr + \Delta f_0 4\pi \int_{R_c}^{\infty} n_{ion}(r) \frac{\sin qr}{qr} r^2 dr \quad (4.17)$$

The resonant term follows as:

$$\begin{aligned} F_{res}(q) &= (f'(E) + \tilde{f}''(E)) 4\pi \int_{R_c}^{\infty} n_{ion}(r) \frac{\sin qr}{qr} r^2 dr \\ &= (f'(E) + \tilde{f}''(E)) v(q) \end{aligned} \quad (4.18)$$

where  $v(q)$  is the Fourier-transform of the distribution function of the counterions  $n_{ion}(r)$ . Equation (4.11) then leads to:

$$I_0(q) = F_0^2(q) + 2f' F_0(q)v(q) + (f'^2 + f''^2)v^2(q) \quad (4.19)$$

Equation (4.19) shows that the intensity measured near the absorption edge consists of three parts: The term  $F_0^2(q)$  denotes the non-resonant intensity that is measured far away from the edge by the conventional SAXS-experiment. The second term is the cross term of the non-resonant and the resonant amplitudes of the macroion and the counterions. It scales linearly with  $f'$  and presents in most cases the leading part of the ASAXS-effect [Stuhrmann 1985]. It should be kept in mind that the amplitude  $F_0(q)$  embodied in this term is still related to the entire scattering object, i.e., to the spatial distribution of the non-resonant scatterers as well. Only the third term is solely related to the spatial distribution of resonantly scattering parts of the object under consideration. Its prefactor is much smaller, however, and its measurement is rather difficult [see Section 4.2.1]. Since we consider centrosymmetric particles the term  $\varphi(\vec{q})$  of Equation (2.90) vanishes and leads us to Equation (4.19) [See Section 2.7].

#### 4.3.4 Model calculation

In the following thesis a model calculation was carried out for typical parameters. Hence, slightly polydisperse, concentric core-shell particles are considered. For spherical polyelectrolyte brushes it is assumed that a system of non-interacting particles with a core diameter of 120 nm and a homogeneous shell of a thickness of 30 nm. The shell is assumed to consist of 14 wt.% of PAA. The contrast of the repeating unit of PAA was estimated from density data and is given by 15 e<sup>-</sup>/unit. From this number of  $Rb^+$  counterions confined in the shell was assumed to be the same as the number of repeating units. For the sake of simplicity it is further assumed that the counterions are evenly distributed. The contrast of the Rubidium ions is  $\Delta f_{ion} = 31.5 \text{ e}^-/\text{nm}^3$ . The latter value has been calculated from the Pauling radius of the Rubidium ion (0.148 nm) [Marcus 1983].

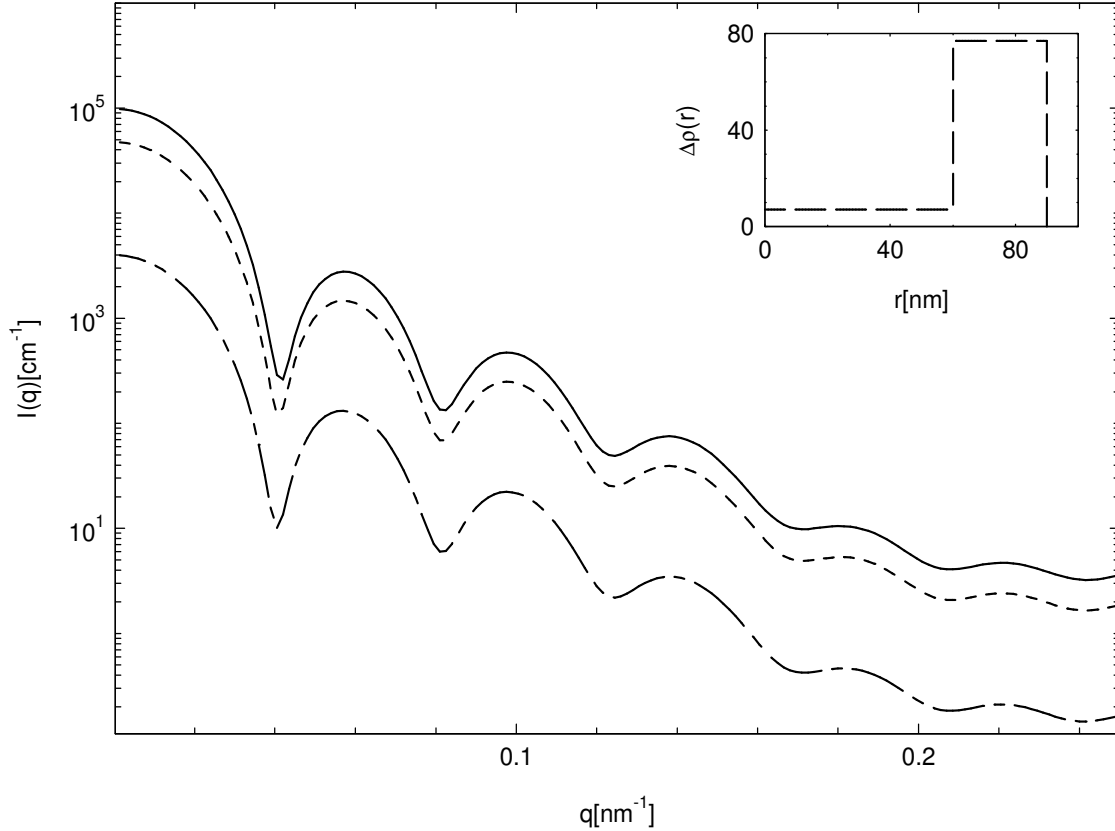


Fig. 4.9: Model calculation: The three partial intensities obtained by an ASAXS-experiment according to Equation. (4.19) are calculated for a spherical polyelectrolyte brush. The weight concentration assumed in this calculation was 6.5%. The parameters are:  $\Delta E = -3.1\text{eV}$ ,  $f' = -8.01$ , and  $f'' = 0.51$ . The solid line denotes the intensity  $I_0(q)$  measured at this energy. The short-dashed lines display the negative cross amplitude  $-2fF_0(q)v(q)$ , whereas the long-dashed line shows the third term of Equation. (4.19).

For  $\Delta\rho_{core}$  the value for poly(styrene) was taken to be  $7\text{ e-}/\text{nm}^3$ , calculated from density data [Dingenouts et al. 1999]. In order to ensure a meaningful comparison with experimental scattering curves, a Gaussian size distribution with a width of 7% was used.

Fig. 4.9 displays the result of a model calculation done for an energy of  $-3.1\text{eV}$  according to Equation. (4.19). The different contributions to the overall intensity  $I_0(q)$  are plotted as a function of the magnitude  $q$  of the scattering vector. The respective scattering factors  $f' = -8.01$  and  $f'' = 0.51$  (Table. 3.1) are taken from the tabulations of [Henke et al. 1993; Brennan et al. 1992]. Fig. 4.9 demonstrates that the cross term  $f'F_0(q)v(q)$  (second term of Equation 4.19) is of considerable magnitude in the immediate vicinity of the edge. As a consequence of this, the negative cross term that increases linearly with  $f'$  will lead to a systematic lowering of the measured scattering curves when approaching the absorption edge. The self-term (long-

dashed line in Fig. 4.9) is smaller but presents a notable contribution to the measured intensity. Moreover, all the three terms shown in Fig. 4.9 show the same oscillations.

#### 4.3.5 ASAXS Results for Spherical Polyelectrolyte Brushes

The ASAXS-data obtained with this suspension can now be evaluated to yield the information on the distribution of the counterions around the macroion. A previous analysis had only extracted the cross term (second term of Equation 4.19) (Dingenouts et al. 2003]. In the course of this work a full analysis of the ASAXS-data was developed recently for the investigation of rod-like polyelectrolytes [See Section 4.2.1] and will now be used for spherical polyelectrolyte brushes as well.

Equation (4.19) shows that the intensity measured near the absorption edge consists of three parts: The term  $F_0^2(q)$  denotes the non-resonant intensity that is measured far from the edge by the conventional SAXS-experiment. The second term is the cross term of the non-resonant and the resonant amplitude of the object. The third term is solely related to the spatial distribution of the counterions.

Fig. 4.10 shows that the measured scattering intensity decreases upon approaching the K-edge of the Rubidium counterions. This is due to the cross term  $f'F_0(q)v(q)$  in Equation (4.19) that is negative because of the sign of  $f'$ . Fig. 4.10 demonstrates that the shift of the scattering curves is a robust effect that can be measured without major problems if precise absolute intensities are available. The model calculations displayed in Fig. 4.9 have shown that the strong effect seen in Fig. 4.10 should be expected for the present system. Hence, the third term in Equation (4.19) is expected to be non-negligible as well. All data have been taken below the edge where  $f''$  is small. Hence, the procedure suggested above for the decomposition of the data can be applied without restriction:  $f_{eff}''$  is small except at the last point below the edge (Table 3.1) and therefore  $f_{eff}''^2 \ll f_{eff}'^2$ . Therefore  $I(q)$  for a given value of  $q$  becomes a quadratic form in  $f_{eff}'$  in very good approximation. All terms can be determined from experimental data by a linear regression.

Fig. 4.11 shows the respective plot, i.e.,  $I(q)$  as the function of  $f_{eff}'$ . Although 13 different energies have been used to generate this plot, for the sake of clarity only one set of data for a single value of  $q$  is shown. The finite curvature demonstrates that the third term of Equation

(4.19) having  $f_{\text{eff}}'^2$  as a prefactor is non-negligible. The solid line shows the fit of Equation (4.19) for  $q = 0.0265 \text{ nm}^{-1}$ .

All terms enumerated in Equation (4.19) can be obtained by repeating this procedure for all  $q$ -values under consideration. Fig. 4.11 demonstrates at the same time that measurements far below the absorption edge are as important as data points in the immediate neighbourhood of the edge. The secure determination of all the three partial intensities rests on a precise analysis of the curvature of this plot.

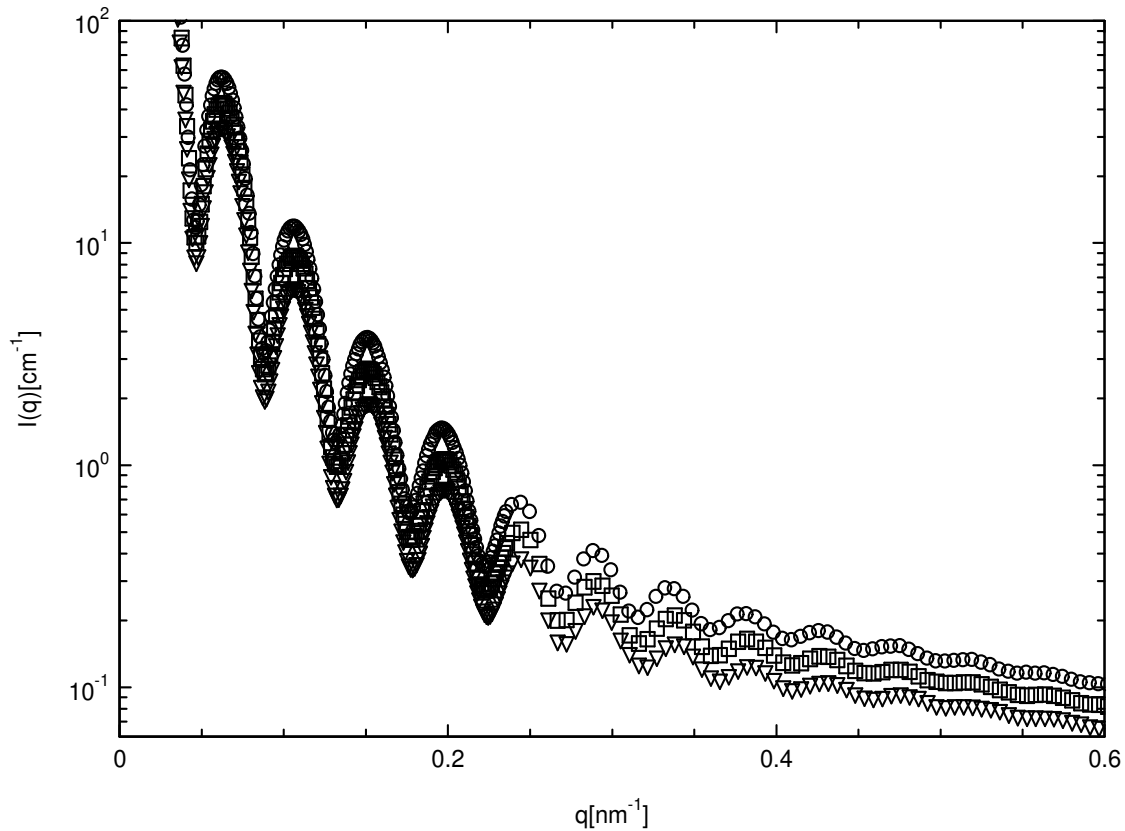


Fig. 4.10 shows the dependence of the measured scattering intensity on the energy of the incident beam. The scattering intensity has been measured at 13 different energies below the edge. For the sake of clarity only three sets of data are displayed, corresponding to the difference  $\Delta E$  to the absorption edge: Circles:  $-2737.1 \text{ eV}$ ; Squares:  $-97.1 \text{ eV}$ ; Triangles:  $-1-1 \text{ eV}$ .

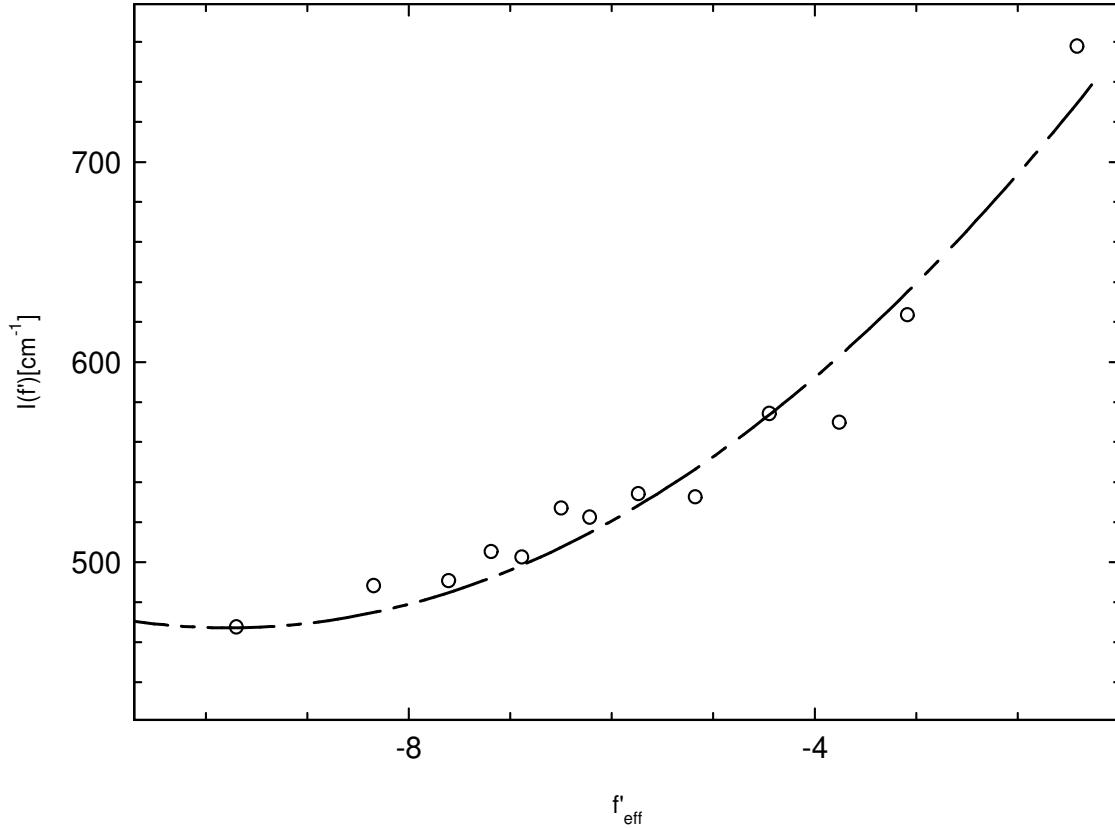


Fig. 4.11 demonstrates the dependence of  $I(q)$  on the real part  $f'$  according to Equation (4.19) for  $q=0.0265 \text{ nm}^{-1}$ . The solid line shows the fit of Equation (4.19) after neglecting  $f''_{\text{eff}}$ . This procedure is repeated for all the  $q$ -values in order to obtain all the three partial intensities displayed in Fig. 4.15

The range of  $f'$  covered by this analysis must therefore be wide enough. Fig. 4.12 displays all three terms enumerated in Equation (4.19). It demonstrates that the entire information embodied in ASAXS-measurements can be determined with good accuracy from experimental data despite the fact that the third term is small. Similar to the case of rod-like polyelectrolytes [see Section 4.2.1], all terms in Equation (4.19) have been obtained.

The result shown in Fig. 4.12 can now be used to test the theoretical predictions [Jusufi et al. 2002] in a qualitative manner. Equation (4.19) and (4.17) suggests to plot the second term  $F_0(q)v(q)$  divided by the third term  $v^2(q)$  as a function of  $q$ :

$$\frac{F_0(q)v(q)}{v^2(q)} = \frac{F_M(q)}{v(q)} + \Delta f_0 \quad (4.20)$$



Hence, ASAXS allows one to obtain the ratio of  $F_M(q)$ , the Fourier-transform of the radial distribution of the macroions and  $v(q)$ , the Fourier-transform of the counterion distribution. The crosses in Fig. 4.12 show that this ratio is a constant except for the region of smallest scattering angles. This demonstrates directly that both distributions have the same dependence on the radial distance  $r$ . The reason for this finding is the strong correlation of the counterions to the polyelectrolyte chains grafted to the surface of the core particles as predicted by theory [Jusufi et al. 2001].

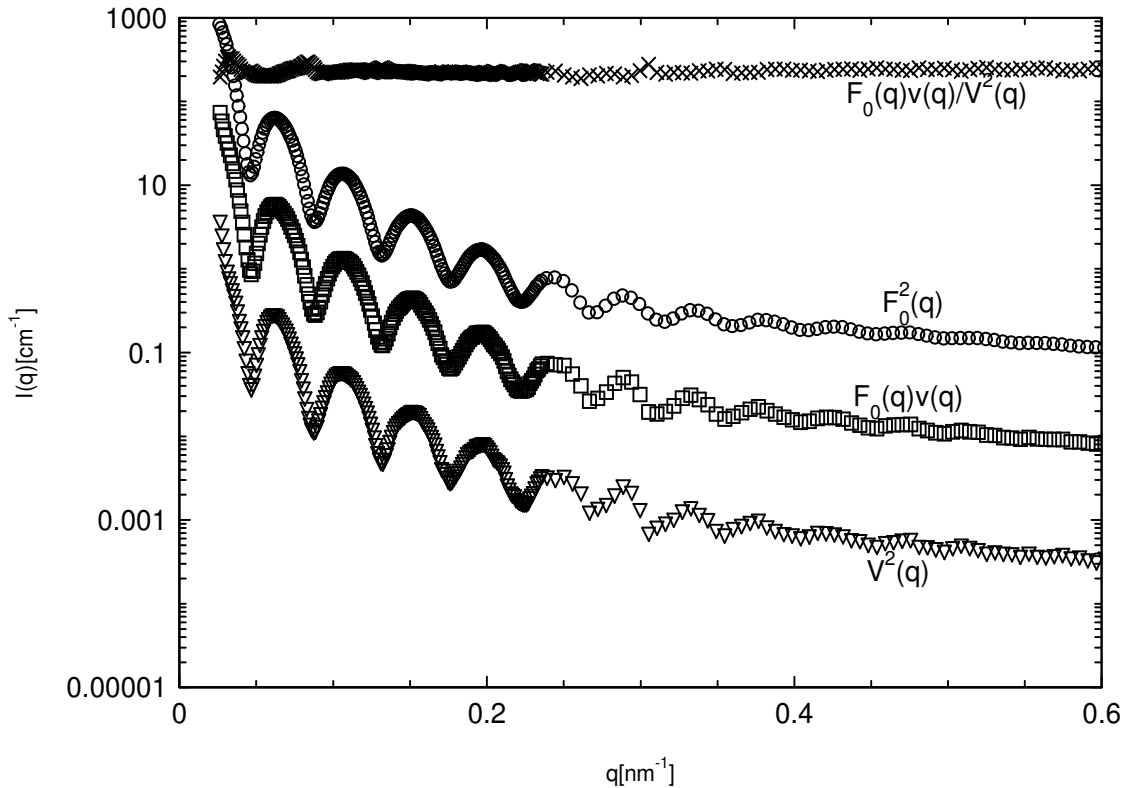


Fig. 4.12 shows the decomposition of the measured ASAXS intensity  $I(q)$  according to Equation (4.19). all the three terms have been obtained from the linear regression. The circles denotes the intensity  $I_0(q)$  measured far away from the absorption edge of Rubidium. The Squares display the cross-term of Equation (4.19) whereas the triangles show the third term of Equation (4.19). The crosses denote the ratio of the second and third term as shown in Equation (4.20).

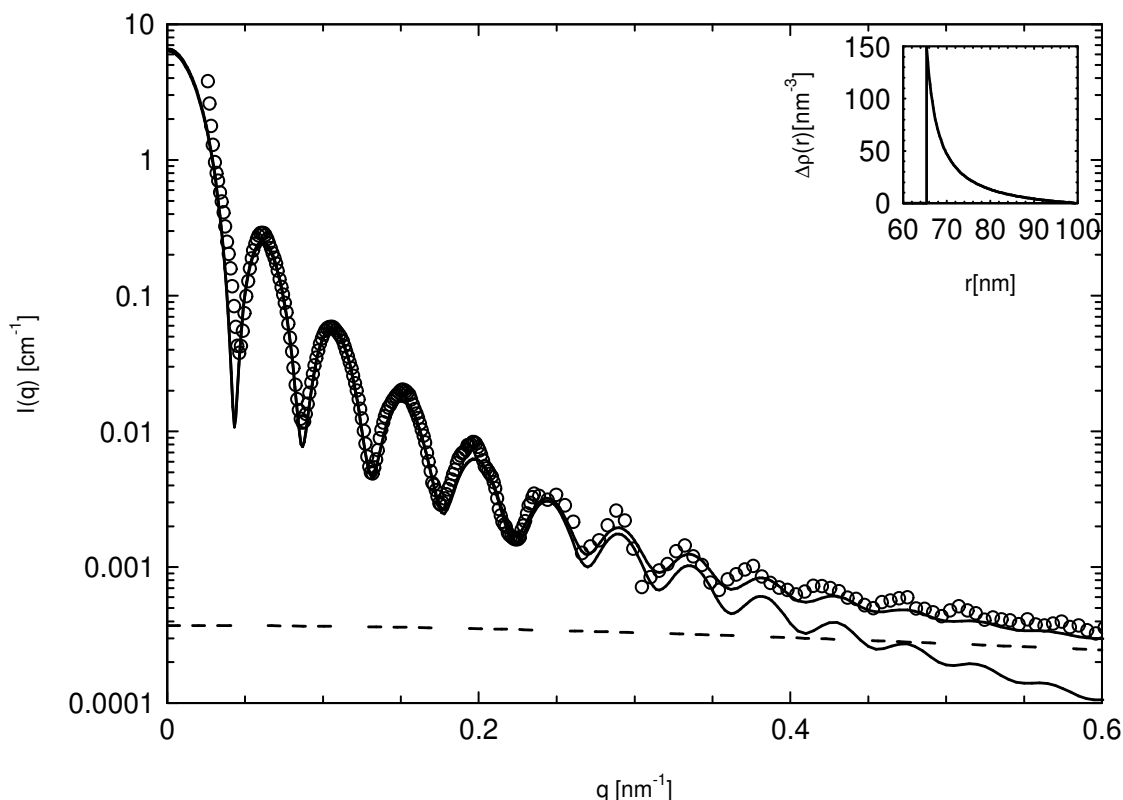


Fig. 4.13 shows the partial scattering intensity of the counterions  $v^2(q)$  as the function of  $q$ . The solid lines represent the fit by the radial profile of the excess electron density displayed in the inset. The dashed lines display the Lorentzian term due to the fluctuations of the polyelectrolyte chains grafted to the surface of the core particles.

As shown by Fig. 4.13 ASAXS leads directly to  $v^2(q)$  which is the scattering intensity of the cloud of counterions. This term can be evaluated to yield the radial distribution of the counterions  $n(r)$ . This analysis is shown in Fig. 4.13. The term  $v^2(q)$  of Fig. 4.12 has been fitted by a radial profile that assumes highly stretched chains, i.e., the distribution  $n(r)$  should scale as  $r^{-2}$ . The chains grafted to the surface, however, have been generated by a radical polymerization and are therefore polydisperse [Guo et al. 2000]. This effect may be taken care by assuming an average profile as shown in the inset of Fig. 4.13. As seen in a previous study, there is an additional scattering contribution that is due to the fluctuations of the polymer chains and the counterions at the surface [de Robillard et al. 2000].

This contribution that hardly comes into play in the present  $q$ -range may be described by a Lorentzian:

$$I_{fluct}(q) = \frac{I_{fluct}(0)}{(1 + q^2 \xi^2)} \quad (4.21)$$

Its contribution is shown by a dashed line in Fig. 4.13. It becomes important only for scattering angles for which  $q > 0.4 \text{ nm}^{-1}$ .

From these results it can be concluded that the good agreement between theory and experiment seen in Fig. 4.13 shows that the polyelectrolyte chains are stretched as predicted by theory [Jusufi et al. 2002]. The determination of the profile can be done very accurately given the fact that 8 to 10 side maxima are seen in all scattering curves. Moreover, the spatial resolution of the experiment expressed in the product of the maximum  $q$ -value and the core radius of the particles is ca. 40. Hence, the present experiment already looks into the fine details of the brush layer attached to the surface of the cores. In this way the results obtained from these ASAXS experiments can directly be compared to data obtained from reflectivity measurements on planar systems [Rühe et al. 1999, 2002; Tran et al. 2001]. The results obtained in these experiments lead us to conclude that the counterions are trapped within the polyelectrolyte brushes as predicted by theory [Jusufi et al. 2002]. These results also corroborate earlier osmotic coefficient measurements that suggest that a very high percentage of counterions are trapped within the polyelectrolyte brushes [Das et al. 2002].

#### 4.4 Effect of pH on Polyelectrolyte Brushes

Earlier reports in literature have demonstrated that, annealed brushes comprising of polyacrylic acid chains, when subjected to a change in the  $pH$  tend to swell as the carboxylic acid groups are subsequently dissociated with the addition of base as eg. NaOH. This phenomenon was studied extensively using Dynamic Light Scattering (DLS). [Guo et al. 2000, 2001]. It was shown that the thickness  $L$  of the brush increases as a function of  $pH$  between 3 to 7 and reaches a plateau thereafter.

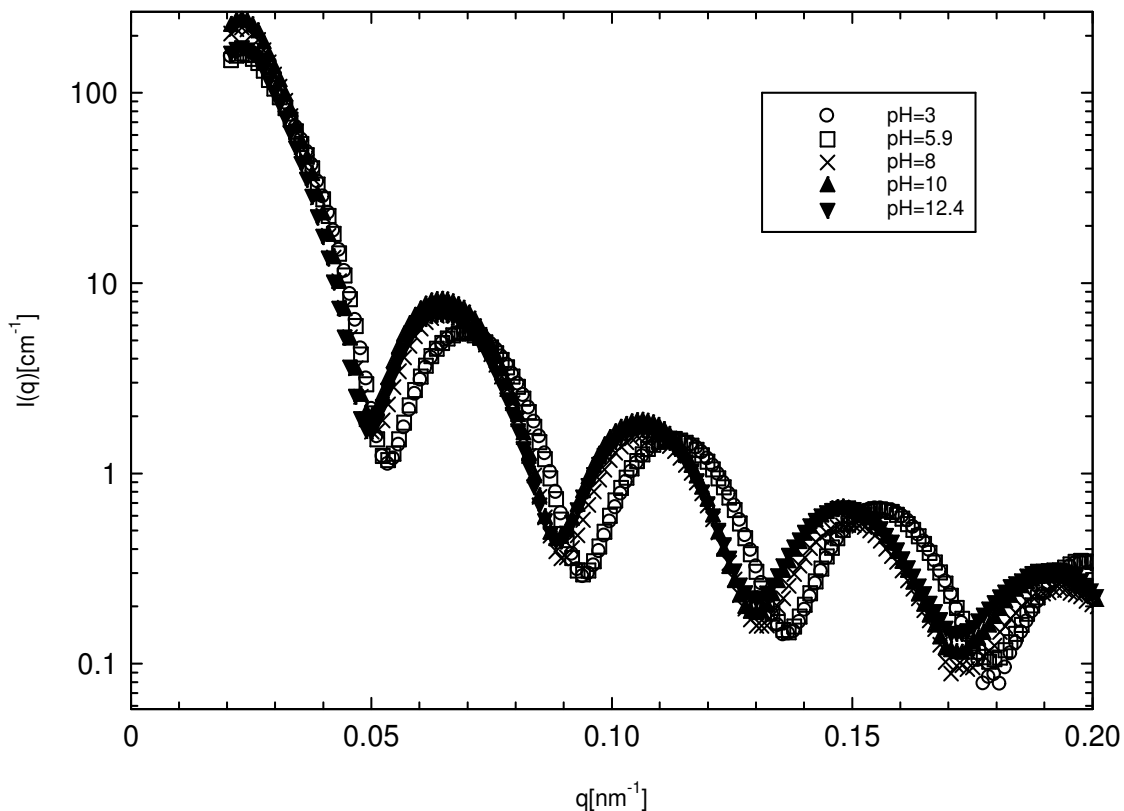


Fig. 4.14 shows the scattering intensities of annealed brushes comprising of polyacrylic acid chains measured at different pH values.  $O$  : pH=3;  $\square$  : pH=5.9;  $\times$ : pH=8;  $\blacktriangle$ : pH=10;  $\blacktriangledown$ : pH=12.4

Fig. 4.14 shows the scattering intensities measured at different pH values. From the Fig. 4.14, it is evident, at around pH=8, a remarkable shift is seen in the maxima towards lower  $q$ -values, indicating a swelling in the thickness of the brush. A further small shift is seen at pH=10 which remains more or less constant thereafter. The increase in the pH results in a higher degree of dissociation of the carboxylic groups, which leads to a higher charge density and a higher osmotic pressure of the counterions, which in turn results in the swelling of the brush. Although the  $pK_a$  for polyacrylic acid is reported to be 4.6 with ionic strength between 0.02 to 0.2 M [Blaakmeer et al. 1990], no remarkable swelling was observed at pH= 5.9. The swelling of brushes as a function of pH has been studied using Dynamic Light Scattering [Guo et al. 2000] and confirmed by the SAXS measurements shown here.

## 4.5 Star-Shaped Polyelectrolytes

Star-shaped polyelectrolytes as shown in Fig. 1.3, comprises of a very small core onto which are attached polyelectrolyte arms of poly(acrylic acid) (PAA) with varying number of arms and degree of polymerization. The synthetic route delivers stars bearing uncharged arms consisting of ester groups, which are then cleaved to generate the corresponding carboxylic acid, the polyelectrolyte is then generated by titrating the polyacid with RbOH solution until the pH of the system was greater than 10. High pH ensured that the arms of star-shaped polyelectrolytes were fully stretched as in the case of spherical polyelectrolyte brushes [Guo et al. 2001].

Star Polyelectrolytes	No. of Arms	Deg. of Polymerization
SP1	21	60
SP2	21	125

Table. 4.3 shows the two different star-shaped polyelectrolytes studied using SAXS and ASAXS

### 4.5.1 SAXS Studies of Star-shaped Polyelectrolytes

A series of SAXS and ASAXS experiments were carried out on star-shaped polyelectrolytes Results of which would be discussed here. As depicted in Table 4.3, two different systems were chosen for SAXS studies i.e., star polyelectrolytes with same number of arms (in this case a system with 21-arms of polyacrylic acid was chosen), but with different degree of polymerization i.e., the arm length with  $P_n=60$  and  $P_n=125$ . Due to different arm lengths, such systems obviously had different overlap volume fractions and were ideally suited to study and compare the behavior of such polyelectrolyte stars in the vicinity of their overlap volume fractions.

Fig. 4.15 shows the SAXS results obtained for star-shaped polyelectrolytes for a series of concentrations below and above the overlap volume fraction for SP1 of Table. 4.3 while Fig. 4.16 shows the concentrations series for SP2 of Table. 4.3.

It is immediately evident from both Fig. 4.15 and Fig. 4.16, that an ordering is observed in the vicinity of the overlap concentration, which then vanishes on either side of the overlap volume fraction in the case SP1 of Table. 4.3  $\phi^*= 0.44$  vol.% (Fig. 4.15) and  $\phi^*= 0.11$  vol.% (Fig. 4.16) SP2 of Table. 4.3.

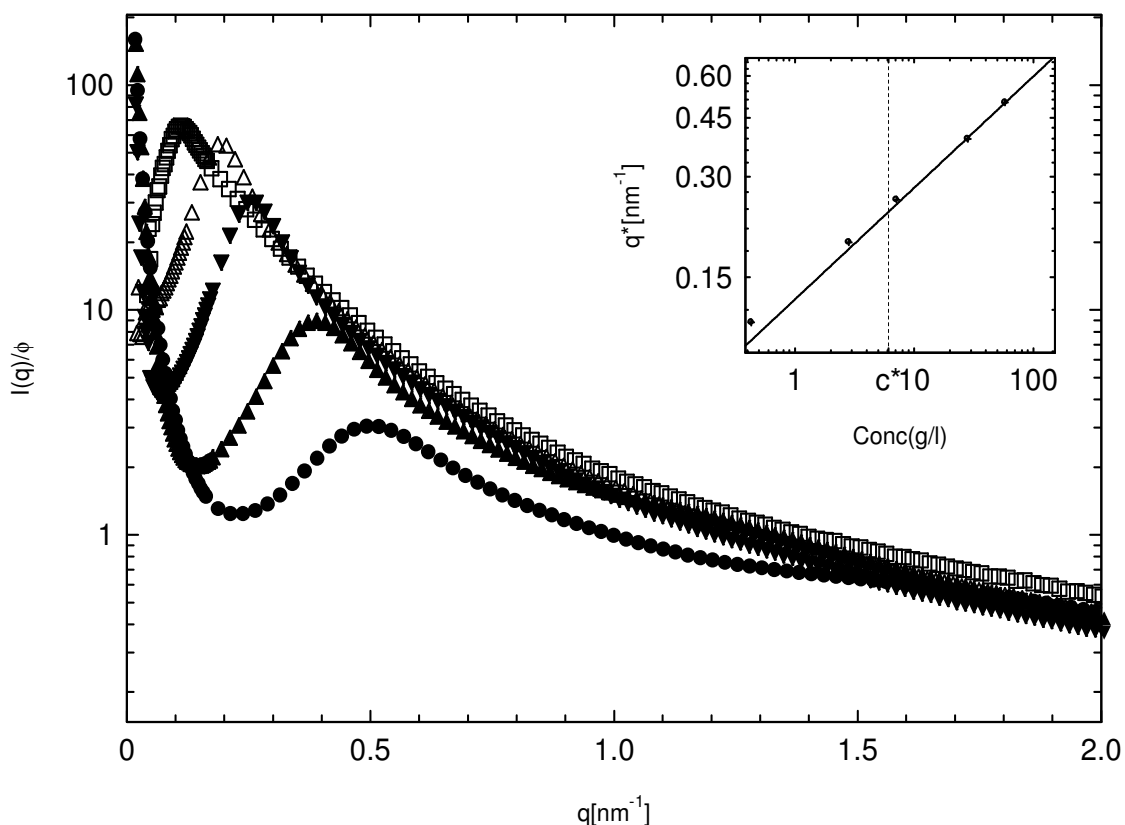


Fig. 4.15 shows the scattering intensities measured for concentration series of star polyelectrolyte (SPI), the overlap volume fraction ( $\phi^*$ ) calculated for such a system is 0.44 vol. %. The empty symbols denote the scattering intensities measured below the overlap volume fraction, and the filled symbols denote the scattering intensities above  $\phi^*$ .  $\square$  : 0.43 g/l;  $\times$ : 1.29 g/l;  $\Delta$  :2.84 g/l;  $\blacktriangledown$ :7.10 g/l;  $\blacktriangle$ :28.16 g/l;  $\bullet$ :58.02 g/l. The inset shows the variation of  $q^*$  as a function of concentration.

The ordering of star-shaped polyelectrolytes is in accordance with the previous observations [Heinrich et al. 2001], where the peak at  $q^*$  was observed to be larger below the overlap concentration. A shift is observed in the  $q^*$  values towards higher  $q$  values as a function of increased concentration. This shift is attributed to the decrease in the interparticle distance between the polyelectrolyte chains of the neighboring star polyelectrolytes. On the other hand, in the semi-dilute regime, as the concentration increases the peak disappears gradually. This can be attributed to the interpenetration of the star polyelectrolytes [Heinrich et al. 2001]. As discussed in the earlier Section.1.3, this type of ordering depends largely upon the number of arms attached onto the core of the star polyelectrolytes.

As observed in earlier Section. 4.2.2 in the case of rod-like polyelectrolytes, an upturn of the scattering intensity is observed at low  $q$  values for star polyelectrolytes as well. This upturn is usually attributed to aggregates [Borsali et al. 1991; Ise et al. 1991]. The inset in Fig. 4.15 and Fig. 4.16 depicts the variation of the peak  $q^*$  as a function of the concentration.  $q^*$  scales as  $(C_p)^{1/3}$ , which is very well in agreement with the earlier findings [Heinrich et al. 2001]. Only the prefactor in both the cases is different depending on the degree of polymerization ( $P_n$ ). For SP1,  $q^* = 0.129 (C_p)^{1/3}$  and for SP2  $q^* = 0.104 (C_p)^{1/3}$ .

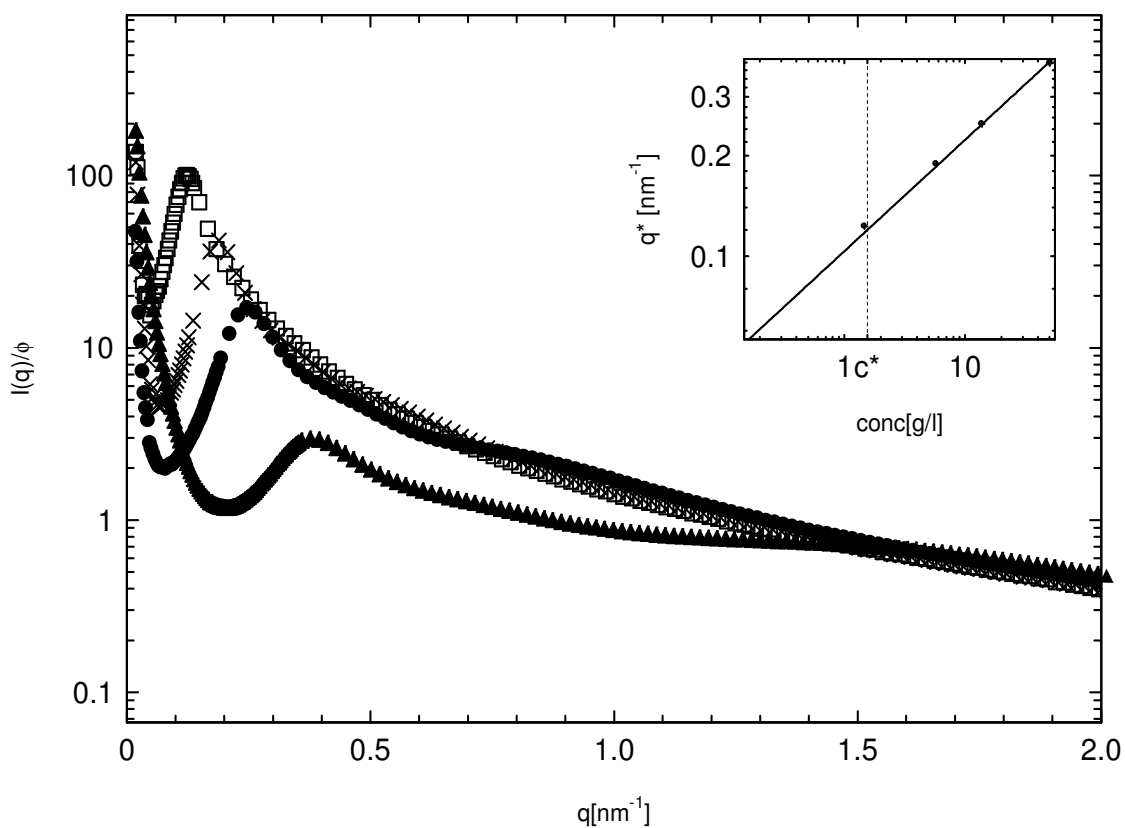


Fig. 4.16 shows the scattering intensities measured for a concentration series of a star polyelectrolyte (SP2), the overlap volume fraction ( $\phi^*$ ) calculated for such a system is 0.11 vol. %. The empty symbols denote the scattering intensities measured below the overlap volume fraction, and the filled symbols denote the scattering intensities above  $\phi^*$ .  $\square$  : 1.47 g/l;  $\times$ : 5.75 g/l;  $\bullet$ : 13.76 g/l;  $\blacktriangle$ : 50.21 g/l. The inset shows the variation of  $q^*$  as a function of concentration.

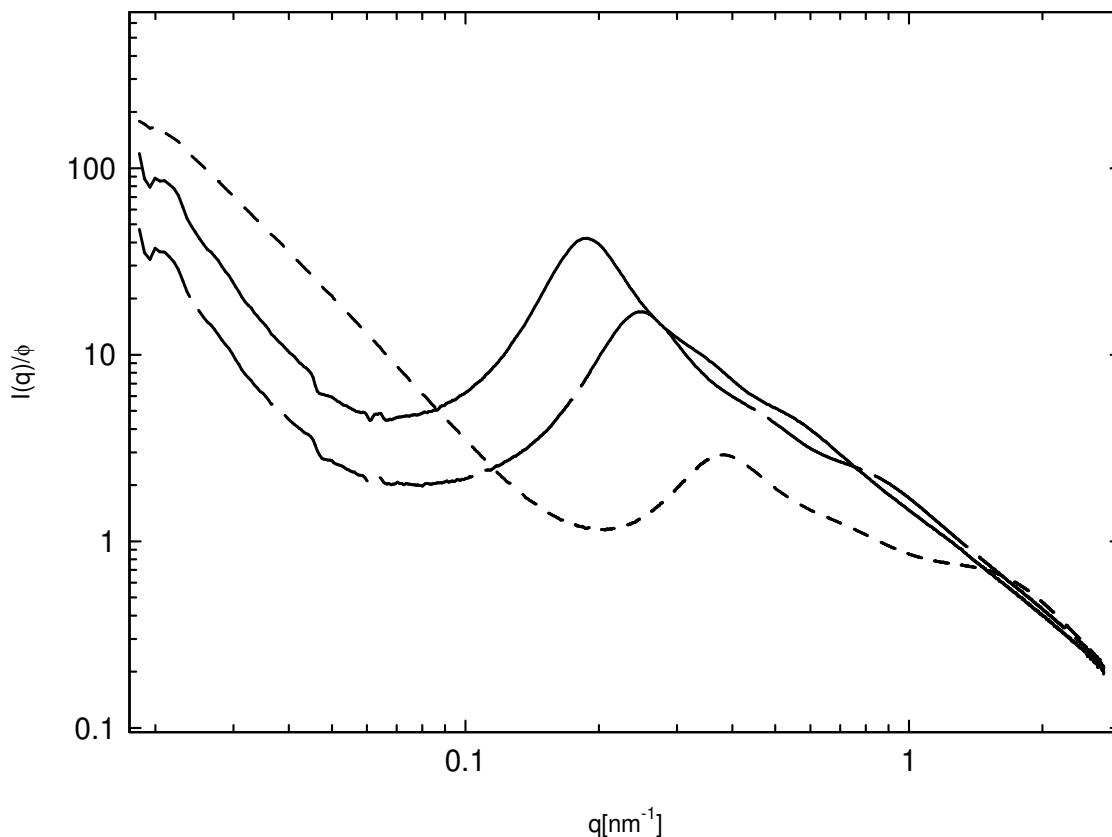


Fig. 4.17 shows a log-log plot of the scattering intensities measured for concentration series of star polyelectrolyte (SPI), the overlap volume fraction ( $\phi^*$ ) calculated for such a system is 0.44vol. %. The solid line denotes g/l; 28.16 g/l; long dashed lines:58.02 g/l; small dashed lines :136.19 g/l . Only the scattering intensities measured after the  $c^*$  are depicted here.

In addition to the first peak, which is generally related to the position order of the star polyelectrolytes, a second peak ( $q^{**}$ ) is seen to be developing as the semi-dilute regime ( $c > c^*$ ) of the star polyelectrolytes is approached. The second peak ( $q^{**}$ ) is clearly visible in Fig. 4.17 and Fig. 4.18 for both the star polyelectrolytes systems investigated. The second peak  $q^{**}$  is observed at higher  $q$  values as compared to the position order peak. The second peak is much broader and seems to be more prominent in the case of polyelectrolyte with a higher degree of polymerization as shown in Fig. 4.18. Earlier SAXS studies stars have observed the presence of the second peak only in the case of charged polyelectrolytes like sodium poly(styrene sulfonate), suggesting the electrostatic nature of the second peak [Heinrich et al. 2001]. In the systems studies here, such a second peak was only evident in the semi-dilute regime ( $c > c^*$ ). As the concentration is increased much higher in the semi-



dilute regime both the peaks seem to disappear gradually suggesting the interpenetration of the star polyelectrolytes.

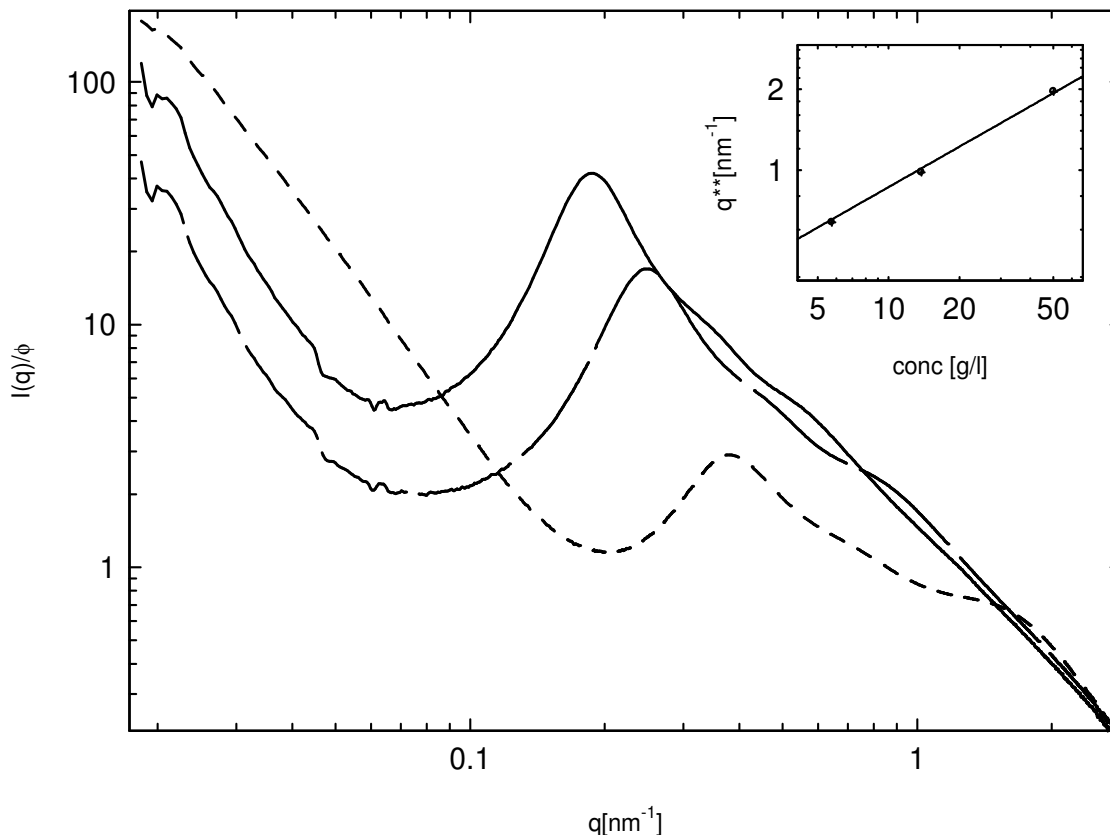


Fig. 4.18 shows a log-log plot of the scattering intensities measured for a concentration series of a star polyelectrolyte (SP2), the overlap volume fraction ( $\phi^*$ ) calculated for such a system is 0.11 vol. %. The solid lines 5.75 g/l; long dashed lines :13.76 g/l; short dashed lines: 50.21 g/l; markers:163.22 g/l. Only the scattering intensities measured after the overlap concentration ( $c^*$ ) are shown, the inset shows the  $q^{**}$  as a function of concentration.

Due to the extreme broad nature of the  $q^{**}$  peak for star polyelectrolytes, it was difficult to locate the position of the peak in case of SP1. However, the position of the second peak  $q^{**}$  in the case of SP2 can be determined relatively well. The inset of Fig. 4.18 shows the variation of the second peak as a function of the concentration, where  $q^{**} = 0.273(C_p)^{1/2}$  is observed. In literature, the second peak is often related to the correlation hole surrounding the polyelectrolyte from which other chains are driven away due to the electrostatic interactions [Heinrich et al. 2001]. Small angle x-ray scattering studies on spherical polyelectrolyte brushes have also shown similar behavior [de Robillard et al. 2000]. In semi-dilute solutions of spherical polyelectrolyte brushes, the variation of the position of  $q^*$  as a function of concentration was  $q^* = C_p^{0.45}$  [de Robillard et al. 2000].

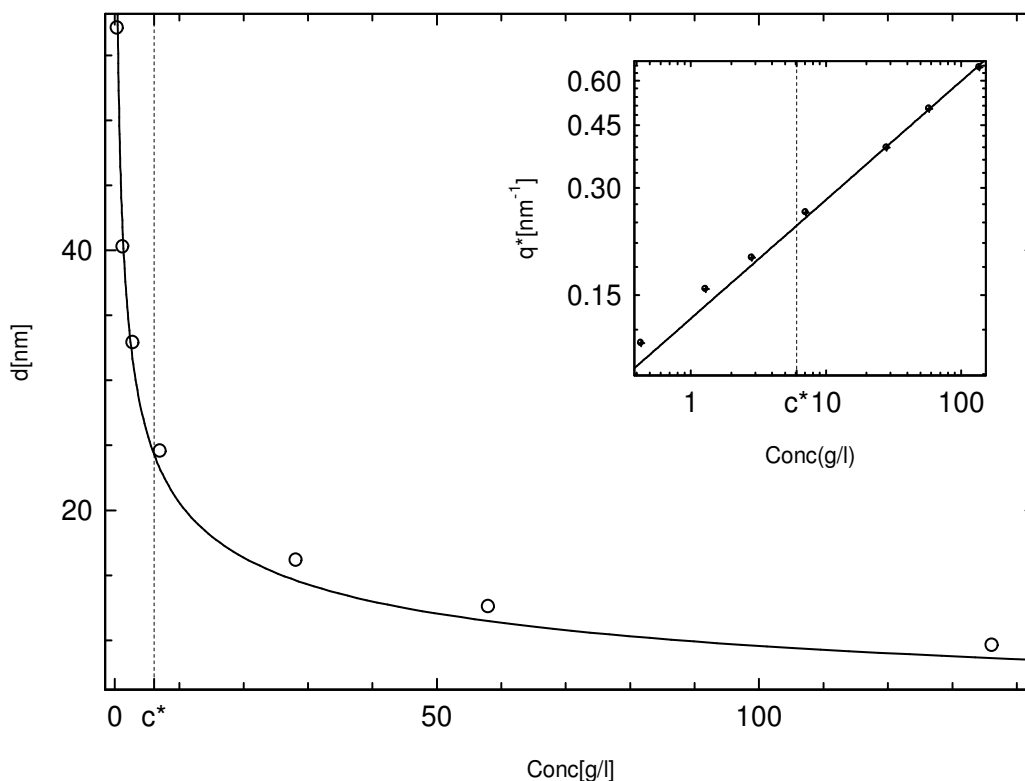


Fig. 4.19 shows the variation of, the inter star distance ( $d$ ) as a function of concentration,  $d \propto Cp^{-1/3}$ , for star polyelectrolytes (SP1), the overlap volume fraction ( $\phi^*$ ) calculated for such a system is 0.44 vol. %. The concentrations are the same as shown in Fig. 4.18. The inset shows the variation of  $q^*$  as a function of concentration.

Functionalized poly(ethylene oxide) (PEO) stars with charged tertiary amino groups at the periphery and varying arm numbers have shown that the nearest-neighbor distance  $D_0$  is proportional with  $-1/3$  power of the concentration [Ishizu et al. 2003]. It was observed that, uncharged PEO stars (*number of arms* > 72) formed a bcc structure near the overlap threshold  $c^*$  and peripherally charged PEO stars (*number of arms* > 37) formed a lattice of bcc below  $c^*$ . This result suggests that the introduction of charges into stars leads to an increase in the ordering of such systems [Ishizu et al. 2003]. This is largely due to electrostatic interactions between adjacent arms. Our results obtained for star polyelectrolytes also show a relation of  $d$  (where  $d = 2\pi/q^*$ ) with the concentration as  $d \propto (Cp)^{-1/3}$ . It can be seen from Fig. 4.19, the inter star distance decreases very sharply as a function of the polyelectrolyte concentration. This decrease in the interstar distance slows down considerably after the overlap concentration as the outer corona of the stars touch each other. A very small decrease in the interstar distance after the overlap concentration can be attributed to the slight interpenetration of the stars. Since no further harmonics are observed from the scattering intensities, no

crystalline structure was found in the systems studied here. The reason for this can be the number of arms present on the star-shaped polyelectrolyte studied here. Similar studies with an increase in the number of arms of star-shaped polyelectrolytes would be extremely helpful to determine its importance in the ordering of such systems.

#### 4.5.2 ASAXS Studies of Star-shaped Polyelectrolytes

In the case of star-shaped polyelectrolytes two sets of data was acquired each at 10m position and 2m position, at a different set of energies. The normalization, correction and the ASAXS decomposition was done prior to joining the scattering intensities at 10m and 2m. Different set of energies was used for the 10m position of the detector as compared to the 2m position. Both the sets of data carried different effective quantities  $f''_{eff}$  and  $f'''_{eff}$ . The final result for the three partial intensities after the ASAXS decomposition were joined without any additional fit parameter.

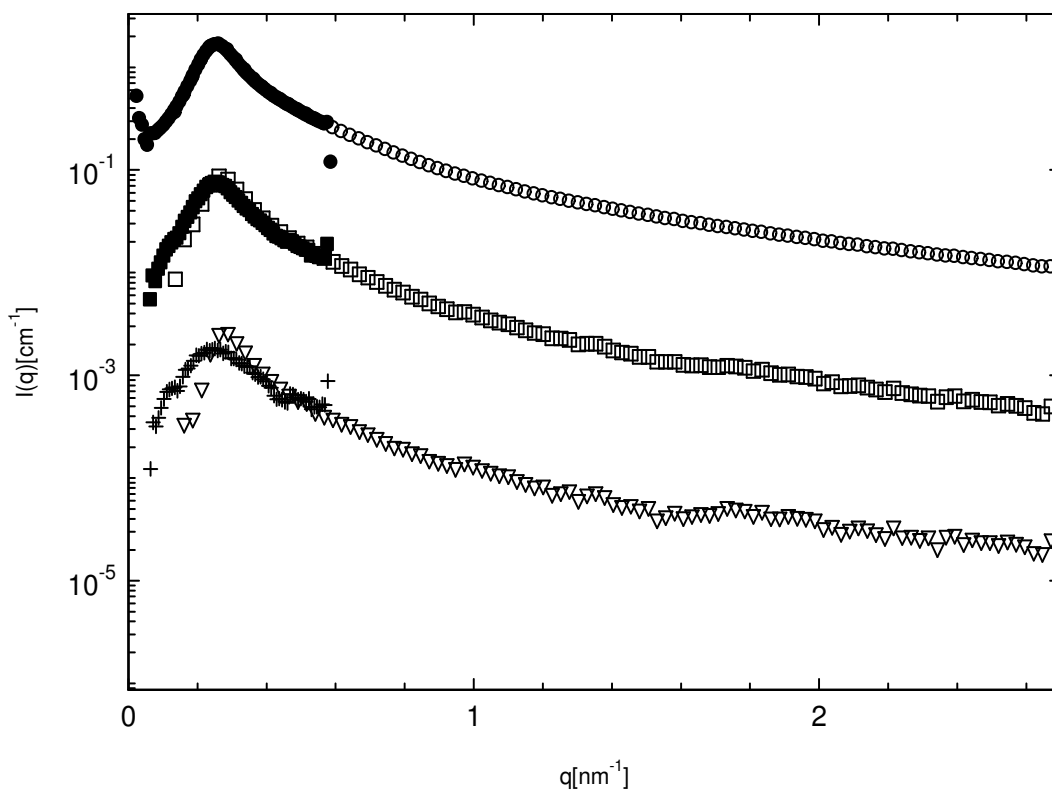


Fig. 4.20 shows the partial intensities obtained for star polyelectrolyte (SP1) separately at 10m and 2m. Filled circles:  $F_0^2(q)$  at 10m; Empty circles:  $F_0^2(q)$  at 2m; Filled squares:  $F_0(q)v(q)$  at 10m; Empty squares:  $F_0(q)v(q)$  at 2m; Crosses:  $v^2(q)$  at 10m; Triangles:  $v^2(q)$  at 2m

As discussed above, in the case of spherical polyelectrolyte brushes and rod-like polyelectrolytes, the analysis of the ASAXS data for star-shaped polyelectrolytes was also carried out in the similar fashion. All the three terms relating to Equation (4.19) can be extracted from this data as well. Fig. 4.21 and Fig. 4.22 show all the three partial intensities as a function of  $q$ , for star-shaped polyelectrolytes (SP1) and (SP2) respectively.

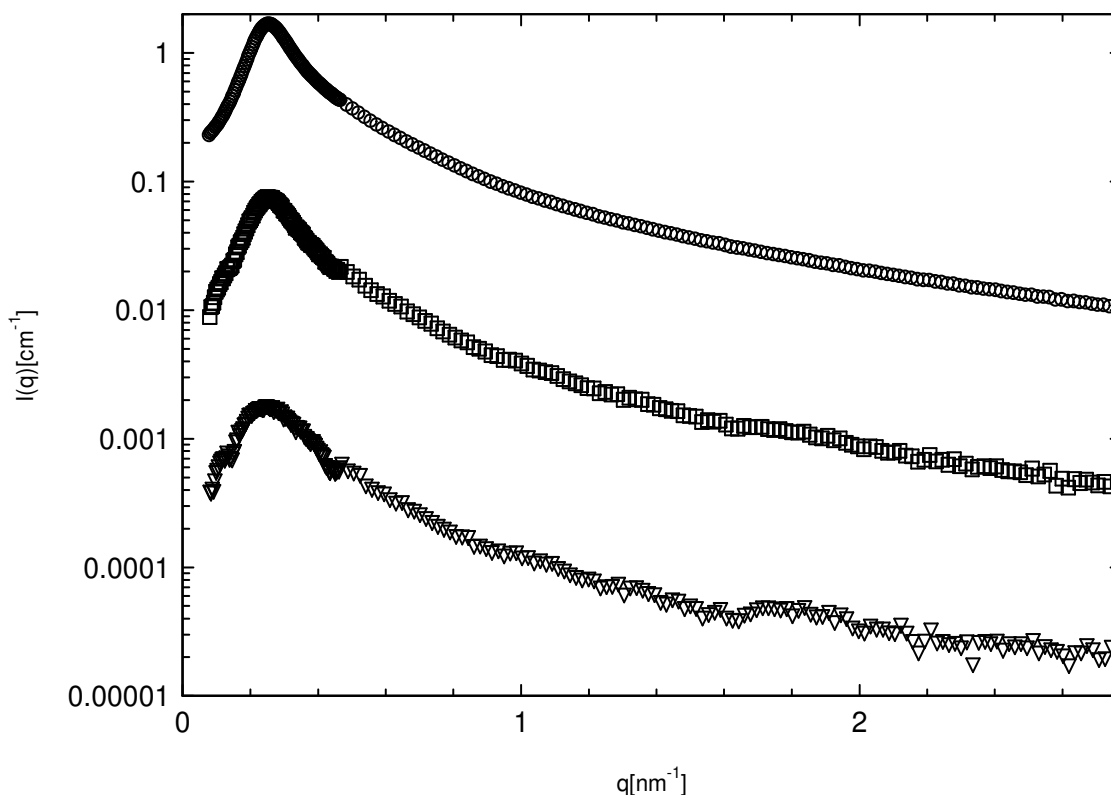


Fig 4.21 shows the decomposition of the measured ASAXS intensity  $I(q)$  for (SP1) according to Equation (4.19). The circles denotes the intensity  $I_0(q)$  measured far away from the absorption edge of Rubidium. The Squares display the cross-term of Equation (4.19) whereas the triangles show the third term of Equation (4.19). For the sake of clarity data point obtained at every 5<sup>th</sup> point is shown here and scattering intensities shown here are within  $q$ -range  $q=0.08$ - $2.78 \text{ nm}^{-1}$ .

As observed in the case of rod-like polyelectrolytes and spherical polyelectrolyte brushes, the counterions are seen closely correlated to the polyelectrolyte chains for star-shaped polyelectrolytes as well. ASAXS studies on polyelectrolytes with different architecture have demonstrated that the counterions are very strongly correlated to the macroions. A different

set of energies was used to obtain ASAXS data for higher  $q$  values as compared to the data at lower  $q$  values. The final partial scattering intensities obtained after ASAXS decomposition can be joined together without any additional parameter ( See Fig. 4.20). This observation suggests that the method employed here is independent of the experimental conditions employed. The history of the data acquisition has no bearing over the final outcome of the ASAXS results.

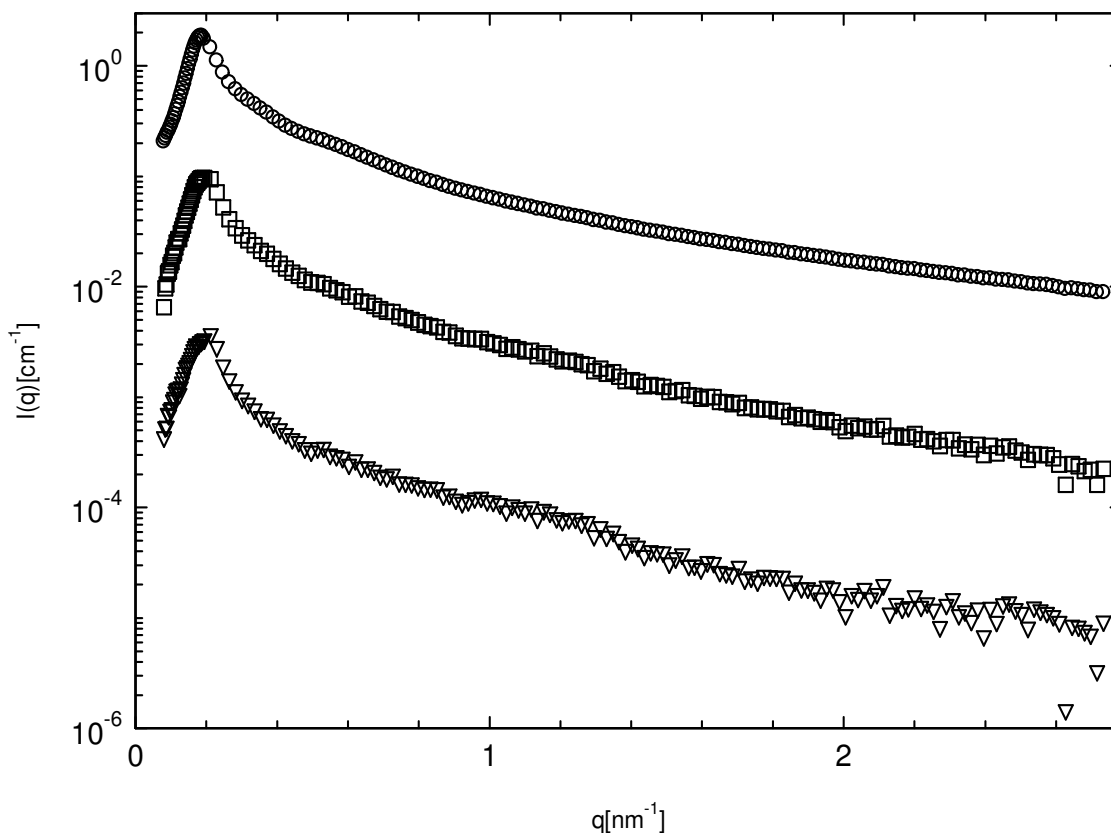


Fig. 4.22 shows the decomposition of the measured ASAXS intensity  $I(q)$  according to Equation. (4.19). all the three terms have been obtained from the linear regression for star-shaped polyelectrolytes (SP2). The circles denotes the intensity  $I_0(q)$  measured far away from the absorption edge of Rubidium. The Squares display the cross-term of Equation (4.19) whereas the triangles show the third term of Equation (4.19). For the sake of clarity data point obtained at every 5<sup>th</sup> point is shown here and scattering intensities shown here are within  $q$ -range  $q=0.08-2.78 \text{ nm}^{-1}$ .

Since ASAXS experiments were carried out in the immediate vicinity of the overlap concentration of the corresponding star polyelectrolytes, a maxima related to the order of such systems is visible at lower  $q$  values. This maxima was also seen in all the SAXS experiments [See Fig. 4.15 and Fig. 4.16] even at very low concentrations below the critical overlap

concentration  $c^*$ . This is due to the strong interactions present in star-shaped polyelectrolytes. From Equation (4.19), it can be demonstrated that the self term can also be obtained as:

$$\frac{(F_0(q)v(q))^2}{F_0^2(q)} = v^2(q) \quad (4.22)$$

In the similar fashion the  $F_0(q)v(q)$  and  $F_0^2(q)$  can also be calculated using the relationship shown in Equation. (4.22). This exercise is then used as a consistency check to validate the accuracy of the ASAXS decomposition.

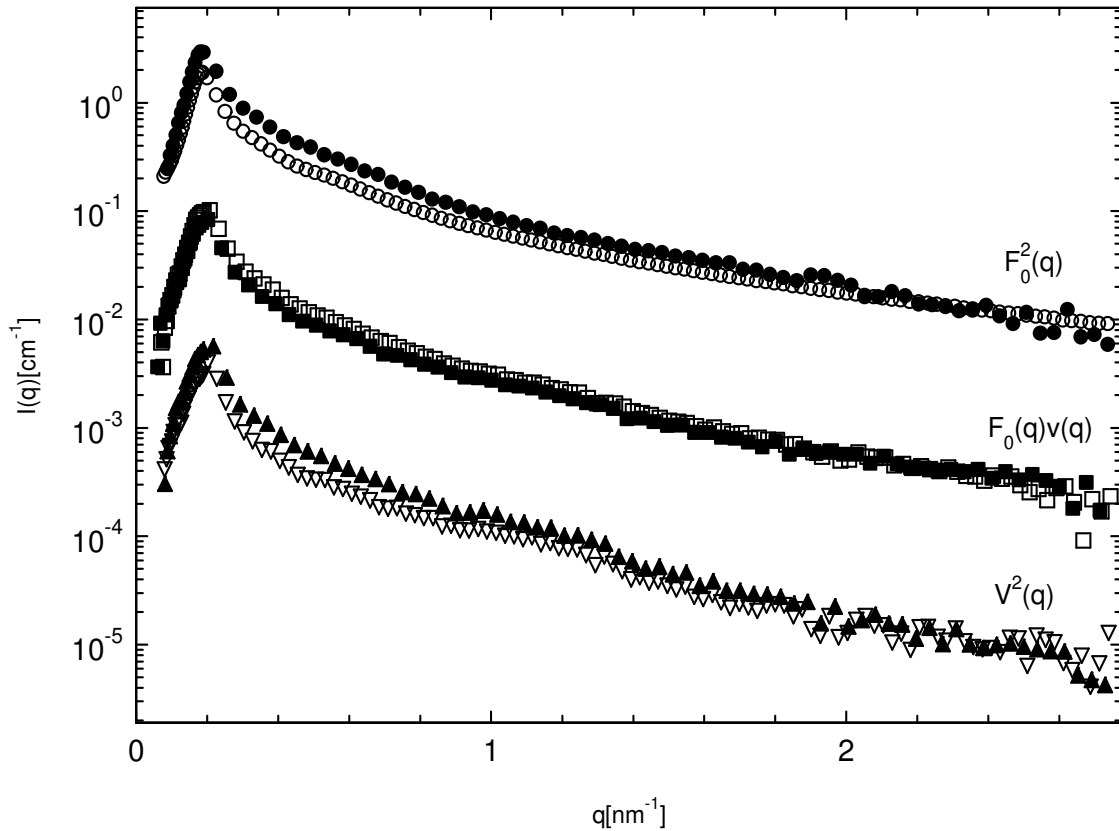


Fig. 4.23 shows the decomposition of the measured ASAXS intensity  $I(q)$  for star-shaped polyelectrolytes (SP2). The empty markers (SP2) denote all the three partial scattering terms obtained after the ASAXS decomposition according to Equation. (4.19). The filled markers (SP2) depict all the three scattering terms calculated according to Equation. (4.22). For the sake of clarity data point obtained at every 5<sup>th</sup> point is shown here and scattering intensities shown here are within  $q$ -range  $q=0.08$ - $2.78 \text{ nm}^{-1}$ .

It is observed from Fig. 4.23 that all the three terms can indeed be calculated from the relationship demonstrated by Equation (4.22). Fig. 4.23 shows the three scattering intensities (filled markers) calculated according to Equation (4.22) compared with the scattering intensities obtained from the normal SAXS decomposition procedure according to Equation (4.19). This consistency check for the SAXS decomposition further validates the SAXS procedure. The results obtained using Equation (4.20) are in agreement with the experimental results within limits of error.

Experimental results of star-shaped polyelectrolytes using SAXS suggest that the counterions are strongly correlated to the macroion as seen for rod-like polyelectrolytes and spherical polyelectrolyte brushes. This study has indeed demonstrates that SAXS is a powerful tool to study polyelectrolytes of different architecture and to extract the important information about the correlation of counterions around the macroion. These results can now be compared with theoretical predictions of star-shaped polyelectrolytes using computer simulations [Jusufi et al. 2002]. Further comparisons of the SAXS results and osmotic pressure measurement would also be helpful.

## 5 Summary

In this thesis, a systematic and comprehensive study of polyelectrolytes in solution has been carried out using Anomalous Small Angle X-ray Scattering (ASAXS) in order to probe the counterion correlation around the macroion. In the course of this study, different polyelectrolyte systems such as, rod-like polyelectrolytes, spherical polyelectrolyte brushes and star shaped polyelectrolytes have been studied using ASAXS.

ASAXS is the method of choice for the study of aqueous polyelectrolytes because it obviates the need of using labelled compounds or counterion exchange, as in the case of SANS or conventional SAXS. Scattering experiments performed near the absorption edge of the element under investigation, allow us to obtain the three partial scattering terms predicted by theory.

The theory of ASAXS predicts that, the measured scattering intensity consists of three parts:

$$I_0(q) = F_0^2(q) + 2f' F_0(q)v(q) + (f'^2 + f''^2)v^2(q)$$

The term  $F_0^2(q)$  denotes the non-resonant intensity that is measured far away from the edge and measured by any conventional SAXS-experiment. The second term is the cross term of the non-resonant and the resonant amplitudes of the macroion and the counterions. It scales linearly with  $f'$ . The third term called as the self-term is solely related to the spatial distribution of resonantly scattering parts of the scattering entity under consideration. All the three partial scattering terms predicted by theory are obtained for the first time experimentally and compared with the theoretical predictions of rod-like polyelectrolytes and spherical polyelectrolyte brushes.

Rod-like polyelectrolytes bearing a rigid poly(p-phenylene) and comprising of two counterions per monomer unit with a persistence length of 21 nm were studied using ASAXS and osmometry. The results of the ASAXS experiments carried out on rod-like polyelectrolytes are compared with the predictions of the Poisson-Boltzmann Cell Model. The results suggest that the counterions are strongly correlated with the macroion. Osmotic coefficient measurements on rod-like polyelectrolytes show that approximately 20% of the counterions are osmotically active. The comparison of the experimentally obtained osmotic coefficient with the theory proceeds without adjusting the charge parameter. The results are in semi-quantitative agreement with the predictions of the Poisson-Boltzmann Cell Model.

Spherical polyelectrolyte brushes consisting of a poly(styrene) core of 68 nm with densely grafted linear poly(acrylic acid) chains with Rubidium counterions were studied using ASAXS. In this thesis the first complete analysis of a colloidal polyelectrolyte brush by



ASAXS has been presented. It has been demonstrated that there is a strong correlation of the counterions to the grafted polyelectrolyte chains of the spherical polyelectrolyte brushes. The correlation between ions and polymer chains in spherical polyelectrolyte brushes is much stronger than linear polyelectrolytes. The experiments therefore validate the theoretical predictions that most of the counterions are fully trapped within the brush and this leads to a strong stretching of the polyelectrolyte chains.

Star-shaped polyelectrolytes bearing 21-arms of poly(acrylic acid) with Rubidium counterions were studied using SAXS and ASAXS. In SAXS experiments, the dependence of the maxima ( $q^*$ ) in the scattering experiments was observed to be concentration dependent. The ordering in star-shaped polyelectrolytes was maximum in the vicinity of the critical concentration ( $c^*$ ). The maxima observed in the scattering experiments obey the scaling theory for polyelectrolytes. This is an indication of some order between the star-shaped polyelectrolytes. Evidence for the presence of any crystalline structure was not found. Scattering experiments with varying number of arms may be helpful to determine their role in the formation of crystalline structure. The three scattering terms predicted by ASAXS theory were also obtained for the star-shaped polyelectrolytes.

It has been demonstrated that ASAXS is indeed a very robust method to study the polyelectrolytes in solution and to obtain the information regarding the distribution of counterions in solution. ASAXS studies of polyelectrolytes have demonstrated that the counterions are strongly correlated to the macroion.

## 5 Zusammenfassung

In dieser Arbeit wurde die Verteilung der Gegenionen von Polyelektrolyten mit Hilfe der Anomalen Röntgenkleinwinkelstreuung (ASAXS) systematisch untersucht. Erstmals wurden verschiedene Polyelektrolytsysteme bzw. kettensteife Polyelektrolyte, sphärische Polyelektrolytbürsten und Stern-Polyelektrolyte mit Hilfe der ASAXS untersucht.

ASAXS ist eine einzigartige Methode, um wässrige Polyelektrolyte zu untersuchen, aufgrund der Tatsache, dass die Verwendung markierter Substanzen oder Gegenionenaustausch nicht mehr notwendig sind. Streuexperimente, die in der Nähe der Absorptions-Kante durchgeführt werden, liefern die drei partiellen Streuterme, welche von der Theorie vorhergesagt werden.

Hiernach besteht die gemessene Streuintensität aus drei Beiträgen:

$$I_0(q) = F_0^2(q) + 2f' F_0(q)v(q) + (f'^2 + f''^2)v^2(q)$$

Der erste quadratische Term ist der nicht-resonante Streubeitrag, der weit unterhalb der K-Kante in einem konventionellen SAXS Experiment gemessen wurde. Der zweite Beitrag ist der Kreuzterm aus dem Quadrat der energieunabhängigen Streuamplitude des Makroions und der energieabhängigen Streuamplitude der Gegenionen. Der Kreuzterm skaliert linear mit  $f'$ . Der dritte Ausdruck wird als Selbstterm bezeichnet und besteht nur aus dem resonanten Anteil der Streuung.

Zum ersten Mal, konnten alle drei Beiträge, welche von der Theorie bereits vorhergesagt werden, für kettensteife Polyelektrolyte und sphärischen Polyelektrolytbürsten experimentell erhalten werden und mit der Theorie verglichen werden.

In dieser Arbeit wurden kettensteife Polyelektrolyte bestehend aus einem Poly(p-Phenyl)-Makroion mit zwei Gegenionen pro Monomer und einer Persistenzlänge von 21 nm mit ASAXS und Osmometrie untersucht. Die experimentell erhaltenen Ergebnisse von ASAXS wurden mit der Poisson-Boltzmann-Theorie verglichen. Es zeigte sich, dass die Gegenionen eng mit dem Makroion korreliert vorliegen. Messungen des osmotischen Koeffizienten an kettensteifen Polyelektrolyten zeigten, dass nur 20% der Gegenionen osmotisch aktiv sind. Der Vergleich der experimentellen Ergebnisse mit der Theorie erfolgte ohne eine Anpassung des Ladungsparameters. Die Ergebnisse sind halbquantitativ mit dem PB-Zellmodell vergleichbar.

Sphärische Polyelektrolytbürsten, welche aus einem Polystyrol-Kern von 68 nm und linearen Polyelektrolytketten aus Polyacrylsäure mit Rubidium-Gegenionen bestehen, wurden mit

Hilfe der ASAXS untersucht. In dieser Arbeit konnte erstmalig eine vollständige Untersuchung kolloidaler sphärischer Polyelektrolytbürsten mit Hilfe der ASAXS vorgestellt werden. Es wurde gezeigt, dass eine starke Korrelation zwischen den Gegenionen und den Polyelektrolytketten vorherrscht. Die Korrelation zwischen den Polyelektrolytketten und den Gegenionen ist hierbei stärker als bei linearen Polyelektrolytketten. Die Untersuchung lässt darauf schließen, dass die meisten Gegenionen innerhalb der Polyelektrolytbürsten eingeschlossen sind. Hierin liegt die starke Streckung der Polyelektrolytketten begründet.

21-ärmige Sternpolyelektrolyte aus linearen Polyacrylsäureketten mit Rubidium-Gegenionen wurden mit Hilfe von SAXS und ASAXS untersucht. Im SAXS-Experiment waren die Positionen der Maxima ( $q^*$ ) abhängig von der Konzentration der Polyelektrolyte und die Ordnung der Stern-Polyelektrolyte war maximal nahe der kritischen Konzentration ( $c^*$ ). Die beobachteten Maxima in den Streuexperimenten folgten der Scaling-Theorie für Polyelektrolyte. Dies lässt auf eine Ordnung zwischen der Stern-Polyelektrolyte schließen. Eine kristalline Struktur wurde bei Stern-Polyelektrolyten nicht gefunden. Die drei partiellen Streuterme, die von der ASAXS-Theorie vorhergesagt werden, wurden auch bei den Stern-Polyelektrolyten erhalten.

In dieser Arbeit konnte gezeigt werden, dass ASAXS eine hervorragend geeignete Methode zur Untersuchung von Polyelektrolyten in Lösung ist und um zusätzlich Informationen über die Gegenionenverteilung zu erhalten. Die ASAXS-Studien zeigten deutlich dass, die Gegenionen stark korreliert mit dem Makroion vorliegen.

## 6 References

- Argiller, J.F.; Tirrell, M., *Theor.Chim. Acta.*, **82**, 343 (1992)
- Ahrens, H.; Förster, S.; Helm, C.A., *Macromolecules*, **30**, 8447 (1997)
- Ahrens, H.; Förster, S.; Helm, C.A., *Phys. Rev. Lett.*, **81**, 4172 (1998)
- Alexandrowicz, Z.J.; *Polym.Sci.*, **40**, 91, (1959)
- Alexandrowicz, Z.; Katchalsky, A.J., *Polym.Sci.*, 3231, (1963)
- Auer,H.; Alexandrowicz,Z., *Biopolymers*, **8**, 1 (1969)
- Alfrey,T.; Berg P.W.; Morawetz, H.J., *Polym.Sci.*, **7**, 543, (1951)
- Aliprantis, A.O.; Canary, J.W., *Jour. Amer. Chem, Soc.*, **116**, 6985 (1994)
- Ballauff, M., *Curr. Opinion Colloid Interf. Sci.*, **6**, 132 (2001)
- Bartunik, H.; Fourme, R.; Phillips, J.C., *Uses of Synchrotron Radiation in Biology*, Stuhmann, H.B.; (ed.), *Academic Press, London* (1982)
- Beniaminy, I.; Deutsch, M., *Comp. Phys. Comm.*, **21**, 271 (1980)
- Berg Rasmussen, F.; Molenbroek, A. M.; Clausen, B. S.; Feidenhans, R. J., *Catalysis*, **190**, 205 (2000)
- Biesalski, M.; Rühle, J.; Johannsmann, D., *J. Chem. Phys.*, **111**, 7029 (1999)
- Biesalski, M.; Johannsmann, D.; Rühle, J., *J. Chem. Phys.*, **117**, 4988 (2002)
- Biesalski, M.; Johannsmann, D.; Rühle, J., *J. Chem. Phys.*, **120**, 8807 (2004)
- Bijvoet, J.M., *Acta Cryst.*, **7**, 703 (1954)
- Bijvoet, J.M., *Acta Cryst.*, **9**, 1012 (1956)
- Biver, C.; Hariharan, R.; Mays, J.; Russel, W. B., *Macromolecules*, **30**, 1787 (1997)
- Blaul, J.; Wittemann, M.; Ballauff M.; Rehahn, M., *Jour. Phys. Chem. B.*, **104**, 7077 (2000)
- Blaul, J.; *Dissertation.*, Universität Karlsruhe (TH), (2001)
- Borisov, O.V.; Birshtein, T.M.; Zhulina, E.B., *J. Phys. II.*, **1**, 521 (1991)
- Borisov, O.V.; Birshtein, T.M.; Zhulina, E.B., *Macromolecules*, **27**, 4975 (1994)
- Borisov, O.V.; Zhulina, E.B., *Eur. Phys. J.*, **4**, 205 (1998)
- Borsali, R.; Nguyen, H.; Pecora, R., *Macromolecules*, **31**, 1548 (1998)
- Borsali, R.; Moinard, D.; Taton, D.; Gnanou, Y.; Rochas, C., *Macromol. Chem. Phys.*, **204**, 89 (2003)
- Bota, A.; Goerigk, G.; Drucker, T.; Haubold, H.-G.; Petro, J., *J. Catalysis.*, **205**, 354 (2002)
- Brennan, S.; Cowan, P.L., *Rev. Sci. Instrum.*, **63**, 850 (1992)
- Cameron, N. S.; Corbierre, M. K.; Eisenberg, A., *Can. J. Chem.*, **77**, 1311 (1999)
- Coulson, D.R., *Inorg.Synth.*, **13**, 121, (1972)
- Chang, S.L.; Chen, S.-H.; Rill, L.R.; Lin, J.S., *Jour. Phys. Chem.*, **94**, 8025 (1990)

- Chang, S.L.; Chen, S.-H.; Rill, L.R.; Lin, J.S., *Prog. Colloid Polym. Sci.*, **84**, 409 (1991)
- Conway, B.E., *Journal of Solution Chemistry*, **7**, 721 (1978)
- Cowley, J.M., *Diffraction Physics*, Elsevier Science Publishers, (1990)
- Cromer D.T.; Liberman D.A., *Acta Cryst.*, **A37**, 267, (1981)
- Currie, E. P. K.; Sieval, A. B.; Avena, M.; Zuilhof, H.; Sudhölter, E. J. R.; Cohen Stuart, M.A., *Langmuir*, **15**, 7116 (1999)
- Dang, T.D.; Bai J.S.; Heberer P.P.; Arnold F.E.; Spry, R.J. J., *Polym. Sci.: Part B: Polym. Phys.*, **31**, 1941 (1993)
- Das, R.; Mills, T.T.; Kwok L.W.; Maskel, G.S.; Millett, I.S.; Doniach, S.; Finkelstein, K.D.; Herschlag, D.; Pollack., *Phys. Rev. Lett.*, **90**, 188103 (2003)
- Das, B.; Guo, X.; Ballauff, M., *Progr. Colloid Polym Sci.*, **121**, 34 (2002)
- Dautzenberg, H.; Jaeger, W.; Kötz, J.; Phillip, J.; Seidel, C.; Stcherbina, D., *Polyelectrolytes Formation, Characterization and Application*, Hanser Publishers, (1994)
- de Robillard, Q.; Guo, X.; Ballauff, M.; Narayanan, T., *Macromolecules*, **33**, 9109 (2000)
- Debye, P.; Menke, H. *Physik Z.*, **31**, 787 (1930)
- Derian, P.J.; Belloni, L.; Drifford, M., *Europhys. Lett.*, **7**, 243 (1988)
- Dingenouts, N.; Ballauff, M., *Acta Polymerica*, **44**, 178 (1993)
- Dingenouts, N.; Ballauff, M., *Acta Polymerica*, **49**, 178 (1998)
- Dingenouts, N., *Dissertation.*, Polymer-Institut, Universität Karlsruhe (TH), (1999)
- Dingenouts, N.; Bolze, J.; Pötschke, D.; Ballauff, M., *Adv. Polym. Sci.*, **144**, 1 (1999)
- Dingenouts, N.; Merkle, R.; Guo, X.; Narayanan, T.; Goerigk, G.; Ballauff, M., *J. Appl. Crystallogr.*, **36**, 578 (2003)
- Dolar, D., in: *Polyelectrolytes; Eds.: Sélegny E., Mandel M. Strauss U.P., Reidel, Dordrecht.*, **97** (1974)
- Deserno, M.; Holm, C.; Blaul, J.; Ballauff, M.; Rehahn, M., *Eur. Phys. J.E.*, **5**, 97 (2001)
- Deserno, M.; Holm, C.; May, S., *Macromolecules*, **33**, 199 (2000)
- Deserno, M., *Dissertation* Max-Planck-Institut für Polymerforschung, Universität Mainz, (2000)
- Farmer, B.L.; Chapman, B.R.; Dudis D.S.; Adams, W.W., *Polymer* **34**, 1588 (1983)
- Feigin, L.; Svergun, D., *Structure analysis by small angle x-ray and neutron scattering*, Plenum Press: New York, (1987)
- Fischer, K., *Z.Naturforsch.*, **36a**, 1253 (1981)
- Förster, S.; Schmidt, M. *Adv. Polym. Sci.*, **120**, 51 (1995)
- Föster, S.; Hermsdorf, N.; Böttcher, Ch.; Lindner, P., *Macromolecules*, **35**, 4096 (2002)

- Fuoss, R.M.; Katchalsky, A.; Lifson, S., *Proc.Natl.Acad.Sci. U.S.A.*, **37**, 579 (1951)
- Furukawa, T.; Ishizu, K., *Macromolecules*, **36**, 434 (2003)
- Galda, P., *Dissertation*. Universität Karlsruhe (TH), (1994)
- Gast, A.P.; Pople, A.J., Armes, S.P.; Vamvakaki, M.; Büttün, V.; Lee, A.S., *Macromolecules*, **35**, 8540 (2002)
- Goerigk, G.; Schweins, R.; Huber, K.; Ballauff, M., *Europhys. Lett.*, **66**, 331 (2004)
- Glikberg, S.; Marcus, Y., *J. Soln. Chem.*, **12**, 255 (1983)
- Guo, X.; Weiss, A.; Ballauff, M., *Macromolecules*, **32**, 6043 (1999)
- Guo, X.; Ballauff, M., *Langmuir*, **16**, 8719 (2000)
- Guo, X.; Ballauff, M., *Phys. Rev. E.*, **64**, 051406 (2001)
- Guillaume, B.; Blaul, J.; Wittemann, M.; Rehahn, M.; Ballauff, M., *J. Phys: Condensed Matter.*, **12**, A245 (2000)
- Guillaume, B.; Ballauff, M.; Goerigk, G.; Wittemann, M.; Rehahn, M., *Colloid Polym. Sci.*, **279**, 829 (2001)
- Guillaume, B., *Dissertation.*, Universität Karlsruhe (TH), (2001)
- Guillaume, B. Blaul, J.; Ballauff, M.; Wittemann, M.; Rehahn, M.; Goerigk, G. *Eur. Phys. J. E.*, **8**, 299 (2002)
- Glatter, O.; Zipper, P., *Acta Physica Austriaca*, **43**, 307 (1975)
- Glatter, O.; Kratky, O., *Small angle x-ray scattering*, Academic Press: London (1982)
- Guenon, P.; Dubreuil, F., *Eur. Phys. J.*, **5**, 59 (2001)
- Guinier, A.; Fournet G., *Small angle scattering of x-rays*, John Wiley & Sons, New York, (1955)
- Groehn, F.; Antonietti, M., *Macromolecules*, **33**, 5938 (2000)
- Haddleton, D. M.; Edmonds, R.; Heming, A. M.; Kelly, E. J.; Kukulj, D., *New Journal of Chemistry.*, **23**, 477 (1999)
- Hadgichristidis, N.J., *Polym. Sci., Part A; Polym. Chem.*, **37**, 857 (1999)
- Hansen, J.P.; McDonald, I.R., *Theory of simple liquids*, London, Academic Press (1986)
- Hariharan, R.; Biver, C.; Russel, W. B., *Macromolecules*, **31**, 7514 (1998)
- Hariharan, R.; Biver, C.; Mays, J.; Russel, W. B., *Macromolecules*, **31**, 7506 (1998)
- Haupt, B.; Neumann, T; Ballauff, M., *Macromol. Bioscience*, **4**, 13 (2004)
- Heinrich, M.; Rawiso.; Zilliox, J.G.; Lesieur.; Simon, J.P., *Eur.Phys. J. E.*, **4**, 131 (2001)
- Henke, B.L.; Gullikson, E.M.; Davis, J.C., *At. Data Nucl. Data Tables.*, **54**, 181-342 (1993)
- Huizenga, J.W.; Grieger, P.F.; Wall, F.T., *Jour.Amer.Chem.Soc.*, **72**, 2636, 4228 (1950)

- Hutchings, L.R.; Richards, R.W.; Reynolds, S.W.; Thompson, R.L., *Macromolecules*, **34**, 5571 (2001)
- Hickl, P., *Dissertation*, Polymerinstitut Universität Karlsruhe (TH) (1997)
- Ise, N., *Angew. Chem. Int. Ed. Engl.*, **25**, 323 (1986)
- Ishizu, K.; Furakawa, T., *Macromolecules*, **36**, 434 (2003)
- James, R.W., *The Optical Principles of the Diffraction of X-Rays*, Bell, London (1962)
- Jusufi, A.; Likos, C. N.; Löwen, H.; Phys Rev. Lett. 2002, 88,018301-1. Jusufi, A.; Likos, C. N.; Löwen, H. J., *Chem. Phys.*, **116**, 11011 (2002)
- Jusufi, A.; Likos, C. N.; Ballauff, M., *Colloid Polym. Sci.*, **282**, 919 (2004)
- Kassapidou K.; Jesse W.; Kuil, M.E.; Lapp, A.; Egelhaaf, S.; van der Maarel, J.R.C. *Macromolecules*, **30**, 2671 (1997)
- Katchalsky, A.; Cooper, R.E.; Upadhyay, J.; Wasserman, A.J., *J. Chem. Soc. London.*, 5198 (1961)
- Katchalsky A.; Alexandrowicz Z.; Kedem O, in *Chemical Physics of Ionic Solutions*, B.E. Conway & R.G. Baradas. Edn (John Wiley & Sons, Inc., NY, ), 295 (1966)
- Katchalsky, A.; *Pure Appl. Chem.*, **26**, 327 (1971)
- Kern, W.Z., *Phys. Chem. A.*, **181**, 249 (1938)
- Lyatskaya, Yu. V.; Leermakers, F. A. M.; Fleer, G. J.; Zhulina, E. B.; Birshstein, T. M., *Macromolecules*, **28**, 3562 (1995)
- Laue, M., *von Röntgenstrahlinterferenzen* Akademische Verlagsgesellschaft, Frankfurt a. Main 1960
- Le Bret, M.; Zimm, B.H., *Biopolymers.*, **23**, 287 (1984)
- Lifson, S.; Katchalsky, A.J., *Polym. Sci.*, **13**, 43 (1954)
- Mandel, M.; Schouten, J. *Macromolecules*, **13**, 1247 (1980)
- Mandel, M.; *Polyelectrolytes. In: Encyclopedia of Polymer Science and Engineering*, 2nd Ed., Wiley & Sons: New York, **11**, 739 (1988)
- Mandel, M., *J. Phys. Chem.*, **96**, 3934 (1992)
- Manning, G. S.; Zimm, B. H. *J. Chem. Phys.* **43**, 4250 (1965) Manning, G. S. *J. Chem. Phys.*, **43**, 4260 (1965)
- Manning, G.S., *Jour. Chem. Phys.*, **51(3)**, 924, (1969)
- Manning, G.S., *Jour. Chem. Phys.*, **51(3)**, 934, (1969)
- Manning, G.S., *Biopolymers*, **9**, 1543, (1970)
- Manning, G. S., *Ann Rev. Phys. Chem.*, **23**, 117 (1972)
- Manning, G.S., *Jour. Phys. Chem.*, **79(3)**, 263, (1975)

- Manning, G. S., *Biophys. Chem.*, **7**, 95 (1977)
- Manning, G. S., *Quart. Rev. Biophys.*, **11**, 179 (1978)
- Manning, G. S., *Biophys. Chem.*, **9**, 65 (1978)
- Manning, G. S., *Acc. Chem. Res.*, **12**, 443 (1979)
- Manning, G. S., *J. Phys. Chem.*, **88**, 6654 (1984)
- Manning, G. S., *Ber. Bunsenges. Phys. Chem.*, **100**, 909 (1996)
- Manning, G. S.; Ray, J. J. *Biomol. Struct. Dyn.*, **16**, 461 (1998)
- Marcus, R. A. *J. Chem. Phys.*, **23**, 1057 (1955)
- Miyaura, N.; Suzuki, A., *Chem Rev.*, **95**, 2457 (1995)
- Miyaura, N.; Yanagi T.; Suzuki, A., *Synth. Comm.*, **11**, 513 (1981)
- Marcus, Y. J., *Solution Chem.*, **12**,4 (1983)
- Marques, C.M.; Izzo, D.; Charitat, T.; Mendes, E., *Eur.Phys.J.*, **3**, 353 (1998)
- Matyjaszewski, K., *Macromolecules*, **33**, 2340 (2000)
- McConnell, G. A.; Lin, M. Y.; Gast, A.P., *Macromolecules*, **28**, 6754 (1995)
- Milas M.; Rinaudo M.; Duplessix R.; Borsali R.; Lindner P., *Macromolecules*, **28**, 3119 (1995)
- Moffit, M.; Khougaz, K.; Eisenberg, A., *Acc. Chem. Res.*, **29**, 95 (1996)
- Muller, F.; Fontaine, P.; Delsanti, M.; Belloni, L.; Yang, J.; Chen, Y. J.; Mays, J. W.; Lesieur, P.; Tirell, M.; Guenoun, P., *Eur. Phys. J. E.*, **6**, 109 (2001)
- Müller, K. in Glatter, O.; Kratky, O., *Small angle x-ray scattering*, Academic Press: London (1982)
- Narayanan, T.; Diat, O.; Boesecke, P., *Nucl. Instrum. Methods Phys. Res. A.*, **467**, 1005 (2001)
- Nordholm, S., *Chem. Phys. Lett.*, **105**, 302 (1984)
- Nyquist, R.M.; Ha, B.Y.; Liu, A.J., *Macromolecules*, **32**, 3481 (1999)
- Okaya, Y.; Saito, Y.; Pepinsky, R., *Phys. Rev.*, **98**, 1857 (1955)
- Okubo T.; Ise, N., *Macromolecules*, **2**, 407 (1969)
- Onsager, L., *Ann. N.Y. Acad. Sci.*, **51**, 627 (1949)
- Oosawa, F., *Polyelectrolytes*. Marcel Dekker: New York., (1971)
- Oppermann, W., *Makromol. Chem.*, **198**, 927 (1998)
- Oppermann, W.; Wagner, M., *Langmuir*, **15**, 4089 (1999)
- Patel, M., Rosenfeldt, S.; Ballauff, M.; Dingenouts, N.; Pontoni, D.; Narayanan, T., *Phys. Chem.Chem. Phys.*, **6**, 2962 (2004)



- Penfold, J.; An, S.W.; Thirtle, P.N.; Thomas R.K.; Baines, F.L.; Billingsham, N.C.; Armes, S.P.; *Macromolecules*, **32**, 2731 (1999)
- Pincus, P., *Macromolecules*, **24**, 2912 (1991)
- Plamper, F., *Diplomarbeit*, Universität Bayreuth (2003)
- Polizzi, S.; Riello, P.; Goerigk, G.; Benedetti, A. J., *Synchrotron Rad.*, **9**, 65 (2002)
- Porod, G. *Kolloid-Z.*, **125**, 51 (1952)
- Rau, I. U. *Dissertation*. Universität Karlsruhe (TH), (1993)
- Rau, I. U.; Rehahn, M., *Acta Polymerica*, **45**, 3 1994
- Rau, I. U.; Rehahn, M., *Makromol. Chem. Phys.*, **194**, 2225 (1993)
- Rau, I. U.; Rehahn, M., *Polymer*, **34**, 2889 (1993)
- Reddy, M.; Marinsky, J., *A. J. Chem. Phys.*, **74**, 3884 (1970)
- Rehahn, M; Schlüter, A.-D.; Wegner, G.; Feast, W. J., *Synthesis*, **5**, 386 (1988)
- Rehahn, M; Schlüter, A.-D.; Wegner, G.; Feast, W. J., *Polymer*, **30**, 1060 (1989)
- Rehahn, M; Schlüter, A.-D.; Wegner, G.; Feast, W. J., *Polymer*, **30**, 1054 (1989)
- Rehahn, M., *Dissertation*, Mainz, (1990)
- Rehahn, M; Schlüter, A.-D.; Wegner, G., *Makromol. Chem. Phys.*, **191**, 1991 (1990)
- Rulkens, R.; Schulze, M.; Wegner, G., *Macromol. Rapid Comm.*, **15**, 669 (1994)
- Rayleigh L., *Proc. Roy. Soc. (London)*, **A84**, 25 (1911)
- Sharma, G; Ballauff, M, *Makrom. Chem. Rapid Commun.*, **25**, 547 (2004)
- Stabinger, H.; Kratky, O., *Makromol. Chem.*, **179**, 1655 (1978)
- Strobl, G.R., *Acta Cryst. A*, **26**, 367 (1970)
- Storey, R.F.; Nelson, M.E., *Appl. Polym. Sci.*, **66**, 151 (1997)
- Stuhrmann, H.B., *Adv Polym Sci.*, **67**, 123 (1985)
- Stuhrmann, H.B.; Goerigk, G.; Munk, B., in *Handbook of Synchrotron Radiation*, ed.S. Ebashi, m.Koch and E.Rubenstein, Elsevier, **4**, Chap 17, pp.557 (1991)
- Suzuki, A. *Pure & Appl. Chem.*, **57**, 1749 (1985)
- Suzuki, A. *Pure & Appl. Chem.*, **58**, 629 (1986)
- Tolman, C. A.; Seidel, W. C.; Gerlach, D. H. *J. Am. Chem. Soc.*, **94**, 2669 (1972)
- Tamashiro, M. N.; Hernandez-Zapata, E.; Schorr, P. A.; Balastre, M.; Tirell, M.; Pincus, P. J. *Chem. Phys.*, **115**, 1960 (2001)
- Thomas, E. L.; Kinning, D. J.; Alward, D. B.; Henkee, C. S., *Macromolecules*, **20**, 2934, (1987)
- Tran, Y.; Auroy, P.; Lee, L.-T., *Macromolecules*, **32**, 8951 (1999)
- Tran, Y.; Auroy, P., *Eur. Phys. J. E*, **5**, 65 (2001)

- van der Maarel, J. R. C.; Groot, L. C. A.; Mandel, M.; Jesse, W.; Jannink, G.; Rodriguez, V., *J. Phys. II France*, **2**, 109 (1992)
- van der Maarel, J. R. C.; Kassapidou K., *Macromolecules*, **31**, 5734 (1998)
- van der Maarel, J.R.C.; Groot, L C A.; Mandel, M.; Jesse, W.; Jannink G.; Rodriguez V., *J.Physique II.*, **2**, 109 (1992)
- Vanhee, S.; Rulkens, R.; Lehmann, U.; Rosenauer, C.; Schulze, M.; Köhler, W.; Wegner, G., *Macromolecules*, **29**, 5136 (1996)
- Verwey, E. J. W.; Overbeck, J. Th. G., *Theory of the Stability of Lyophobic Colloids*. Amsterdam: Elsevier, (1948)
- Wallow, T. I.; Novak, B. M., *Jour. Amer. Chem. Soc.*, **113**, 7411 (1991)
- Wallow, T. I.; Novak, B. M., *Polym. Prep.*, **33**, 908 (1992)
- Wallow, T. I.; Novak, B. M., *Polym. Prep.*, **32**, 191 (1991)
- Wang, L.; Bloomfield V. A., *Macromolecules*, **23**, 194 (1990)
- Wang, L.; Bloomfield V. A., *Macromolecules*, **23**, 804 (1990)
- Wang, L.; Bloomfield V. A., *Macromolecules*, **24**, 5791 (1991)
- Wesley, R. D.; Cosgrove. T.; Thomson, L.; Armes, S. P.; Billingham, N. C.; Baines, F. L., *Langmuir*, **16**, 4467 (2000)
- Witte mann, A.; Haupt, B.; Ballauff, M., *Phys. Chem. Chem. Phys.*, **5**, 1671 (2003)
- Witte mann, M. *Dissertation.*, Universität Karlsruhe (TH), (2000)
- Witte mann, M.; Kelch, S.; Blaul, J.; Hickel, P.; Guillaume, B.; Brodowski, G.; Horvath, A.; Ballauff, M.; Rehahn, M., *Macromol. Symp.*, **142**, 43 (1999)
- Witte mann, M.; Rehahn, M., *J. Chem. Soc., Chem. Comm.*, 623 (1998)
- Williams, C.E. *Conf. Proc. Ital. Phys. Soc. 1990, 25. Eur. Conf. Prog. X-Ray Synchrotron Radiat. Res.* <sup>nd</sup> **2** (1989)
- Wu, C.F.; Chen, S.H.; Shih, L.B.; Lin, J.S. *Phys. Rev. Lett.*, **61**, 645 (1988)
- Zernicke, F.; Prins, J.A., *Z. Physik.*, **41**, 184 (1927)
- Zhulina, E.B.; Borisov, O.V.; Birshtein, T.M., *J.Phys II.*, **2**, 63 (1992)
- Zhulina, E.B.; Borisov, O.V.; Birshtein, T.M., *Macromolecules*, **28**, 1491 (1994)
- Zhulina, E.B.; Borisov, O.V., *Macromolecules*, **29**, 2626 (1996)
- Zhulina, E.B.; Birshtein, T.M., *Ber. Bunsen-Ges.Phys.Chem.*, **100**, 929 (1996)
- Zhulina, E.B.; Borisov, O.V.; Birshtein, T.M., *Macromolecules*, **32**, 8189 (1999)
- Zhulina, E.B.; Borisov, O.V.; Klein, Wolterink, J., *Macromolecules*, **33**, 4945 (2000)

## Appendix

### 7 Synthesis

In the following chapter the synthesis of rod-like polyelectrolytes, Spherical Polyelectrolyte Brushes and Star-shaped Polyelectrolytes would be discussed briefly. The rod-like polyelectrolytes were synthesized using the synthetic strategy developed by Rehahn et al. [Rehahn et al. 1988, 1989, 1990]. The spherical polyelectrolyte systems used for this work were synthesized and kindly provided by Dr.Xuhong Guo. The Star-shaped polyelectrolytes used for the scattering studies were synthesized and kindly provided by Mr.Felix Plamper ( MC II, University of Bayreuth ).

#### 7.1 Synthesis of Rod-like Polyelectrolytes

The monomer was synthesised using the sequence described by Rehahn et al. [Rau, Rehahn 1994]. The first step involved mono methylation of 6-bromohexane through nucleophilic substitution of the bromo functionality by refluxing with sodium methanolate in a methanol/diethyl ether mixture for two days using potassium iodide as a catalyst. [Dionneau 1907; Rau, Rehahn 1994]. The product 6-bromohexylmethylether was distilled from other oligomers using SCHREINER-BÖSHERTZ column. 6-bromohexylmethylether was then reacted with magnesium in diethylether to form Grignard-Reagent, in the presence of dichloro(1,3-bis(diphenylphosphino)propane)-nickel(II) as a catalyst followed by a coupling reaction with p-dichlorobenzene to 1,4-bis(6-methoxyhexylbenzene)[Rehahn Schlüter 1988; Rau, Rehahn 1994]. The raw product was purified by distillation. The next step involved the deprotection of the ether groups. 1,4-bis(6-methoxyhexylbenzene) was refluxed with HBr/AcOH for 48 hours [Rau, Rehahn 1993, 1994]. The raw-product was recrystallized in methanol. 1,4-bis(6-bromohexyl)benzene was refluxed for 3 days in presence of bromine using dichloromethenechloride as solvent under absolute dark conditions and Iodine as the catalyst. Special care is to be taken to avoid light entering the reaction vessel. The reaction mixture is then neutralized NaOH-solution. The product is recrystallized using ethanol/hexane mixture (1:1). In the next step sodium-t-butanolate is refluxed in presence of excess phenol in dimethylformamide to form sodium phenolate. 1,4-dibromo-2,5-bis(6-bromohexyl)benzene in toluene and potassium iodide as catalyst is then added and the reaction mixture was refluxed overnight . The nucleophilic reaction of bromide functional group into phenoxy

group on the side chains forms 1,4-dibromo-2,5-bis(6-phenoxyhexyl)benzene. After workup the raw product is crystallized in hexane and loaded on silica gel column and eluted using toluene as mobile phase and recrystallized in hexane.

The final step is the formation of the monomer unit 4-bromo-2,5-bis(6-phenoxyhexyl)phenylboronic acid [Rehahn et al. 1989;Rau, Rehahn 1994]. n-butyllithium at  $-55\text{ }^{\circ}\text{C}$  was added to a solution of 1,4-dibromo-2,5-bis(6-phenoxyhexyl)benzene in a mixture of diethylether and toluene. The suspension is then stirred at room temperature for 2 hours. The reaction mixture was recooled to  $-60\text{ }^{\circ}\text{C}$  to which trimethylborate was added and refluxed overnight. The mixture is then hydrolysed with dil. HCl to form the monomer. The product is purified using column chromatography. The purification of precursor is very critical in order to obtain high molecular weight polymers.

### Synthesis of 6-bromomethyl ether:

(Rau, Rehahn 1994)



88 g sodiummethanoate, 1.6 g of potassium iodide was added in 300 ml of distilled and dried diethyl ether, in a 2L three-neck flask, fitted with an overhead stirrer, and reflux condenser. Using a 500 ml addition funnel, 450ml of methanol was added drop wise to this suspension, to dissolve sodium methanoate. To this clear solution, 250 g of 1,6-dibromohexane was added using an addition funnel. The reaction mixture was refluxed for two days.

After cooling, the NaBr thus formed was dissolved using 500 ml water. The water phase was extracted 4-5 times with t-butylmethylether. The organic phase was washed with 3\*100 ml water, dried over  $\text{MgSO}_4$ . After evaporation of the solvent, using rota vapour, a yellow oily raw product was obtained.

Purification of the raw product was carried out by fractional distillation method, using SCHREINER-BOSHERTZ column with a reflux rate 120:1, and a pressure of 50 mbar.

Boiling point: 119°C (p=60 mbar)

<sup>1</sup>H-N.M.R (CDCl<sub>3</sub>):

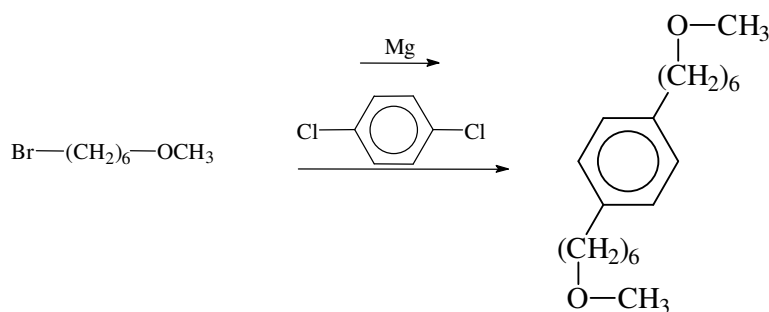
δ= 1.39; 1.47; 1.58; 1.87; (4m, 8H, Br-CH<sub>2</sub>-(CH<sub>2</sub>)<sub>4</sub>); 3.33(s, 3H, O-CH<sub>3</sub>); 3.37(t, 2H, CH<sub>2</sub>-O); 3.41(t, 2H, Br-CH<sub>2</sub>)

<sup>13</sup>C-N.M.R (CDCl<sub>3</sub>):

δ= 25.31; 27.95; 29.41; 32.69; (4t, Br-CH<sub>2</sub>-(CH<sub>2</sub>)<sub>4</sub>); 33.80(t, Br-CH<sub>3</sub>); 58.49(q, CH<sub>3</sub>); 72.58(t, O-CH<sub>2</sub>)

### Synthesis of 1,4-bis(6-methoxyhexyl)benzene:

(Rehahn, 1994)



In a 1-L three-neck flask, fitted with an addition funnel and reflux condenser, under nitrogen atmosphere, 26 g of magnesium fillings was taken in 300ml. distilled and dry ether. In the addition funnel, 4.04 g of 6-bromohexylmethyl ether in 100ml diethyl ether was taken, after addition of approx. 10 ml of this solution, the reaction mixture was slightly heated to trigger an exothermic Grignard reaction, the rest of the 6-bromohexylmethyl ether solution in diethyl ether was then added drop wise, in such a way as to maintain a gentle reflux of the reaction mixture. Once the addition was complete, the reaction mixture was refluxed under nitrogen overnight, a grayish two phase reaction mixture was obtained.

In another 2-L three-neck flask, fitted with addition funnel, reflux condenser, under nitrogen atmosphere 8.19 g 1,4-dichlorobenzene and 75.44 mg of dichloro-(1,3-bis(diphenylphosphino)propane)nickel-II in 100 ml diethyl ether was taken. To this approx. 20 ml, of the Grignard's reaction mixture, under nitrogen, was added using addition funnel, the Grignard's coupling reaction is triggered by warming the reaction mixture slightly, the

color of the green reaction mixture turns reddish brown, the rest of the reaction mixture is then added slowly, maintaining a gentle reflux of the solvent. After addition of the Grignard reagent is complete, the reaction mixture is refluxed for 3 days, MgBrCl precipitates out. The reaction mixture is carefully neutralized in an ice bath using 2M HCl solution, to obtain a clear two phase reaction mixture. The organic phase is separated, and the water phase extracted using 2\*80 ml. t-butylmethyl ether. The complete organic phase is washed with 3\*100 ml water, and dried overnight under MgSO<sub>4</sub>. After evaporation of solvent, using rota vapour, the raw product obtained as colorless oil is further distilled using Vigreux column under reduced pressure. (Pressure =  $4.0 \cdot 10^{-1}$  )

Boiling Point: 145-159 °C

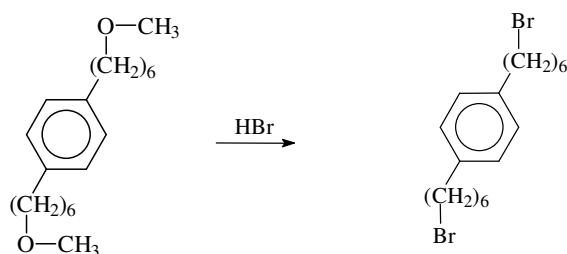
<sup>1</sup>H-N.M.R (CDCl<sub>3</sub>):

δ= 1.36; 1.56; (2m, 16H, Aryl-CH<sub>2</sub>-(CH<sub>2</sub>)<sub>4</sub>); 2.56(t, 4H, Aryl-CH<sub>2</sub>); 3.32(t, 6H, CH<sub>3</sub>-O); 3.35(t, 4H, O-CH<sub>2</sub>)

<sup>13</sup>C-N.M.R (CDCl<sub>3</sub>):

δ= 26.01; 29.17; 29.57; 31.50; 35.46 (5t, CH<sub>2</sub>); 58.52(q, O-CH<sub>3</sub>); 72.89(t, CH<sub>2</sub>-O); 128.22(d, C<sub>2</sub>); 139.95 (s, C<sub>1</sub>)

### 1,4-bis(6-bromohexyl)benzene:



20 g of 1,4-bis(6-methoxyhexyl)benzene was taken in a 1 L three neck flask, equipped with a reflux condenser and a addition funnel, to this was added 137.2 ml of 5.7M HBr solution in acetic acid, the reaction mixture was refluxed for 2 days. To the ensuing brown reaction mixture, 750 ml of water was added, and extracted with 4\*150 ml of t-butylmethyl ether. The organic phase was neutralized extremely carefully using 3\*120 ml of 2M sodium carbonate solution (Caution: CO<sub>2</sub> is liberated vigorously). The organic phase is then washed with 100\*3

ml water and dried using  $\text{MgSO}_4$ , the solvent is evaporated, and the yellow brown solid raw product was re-crystallized in 1L methanol, to obtain pure white needle-like crystals.

Yield: 16.48 g; white needle like crystals

$^1\text{H-N.M.R}$  ( $\text{CDCl}_3$ ):

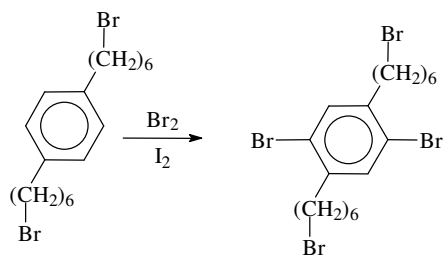
$\delta = 1.35; 1.46; 1.61; 1.85; (4m, 16H, \text{Aryl-CH}_2\text{-(CH}_2\text{)}_4); 2.57(t, 4H, \text{Aryl-CH}_2); 3.39(t, 4H, \text{CH}_2\text{-Br}); 7.08(s, 4H, \text{H-Aryl})$

$^{13}\text{C-N.M.R}$  ( $\text{CDCl}_3$ ):

$\delta = 28.02; 28.39; 31.29; 32.72; 33.99; 35.37 (6t, \text{CH}_2); 128.25 (d, \text{C}_2); 139.80(s, \text{C}_1)$

### 1,4-dibromo-2,5-bis(6-bromohexyl)benzene:

(Rehahn 1988)



In a light protected reaction hood (the reaction hood was completely covered using aluminum foil), 5.98 g of 1,4-bis(6-bromohexyl)benzene and 1.19 g iodine was dissolved in 200 ml dichloromethane, the reaction setup (1 L three necked flask fitted with reflux condenser and addition funnel), was covered using aluminum foil to protect from light 1.6 g of bromine dissolved in 20 ml. dichloromethane was taken in the addition funnel and was drop wise added to the reaction mixture. The reaction mixture was refluxed for 3 days, after cooling the reaction mixture 40 ml of 2N NaOH was added, and the reaction mixture was stirred overnight at room temperature. The mixture was transferred to a round bottom flask and the dichloromethane evaporated, using rotavapour. To the ensuing two phase reaction mixture, 200 ml. toluene was added, the organic layer is separated and the aqueous layer extracted with 3\*100 ml toluene. The complete organic layer is washed with 3\*100 ml water and dried overnight over  $\text{MgSO}_4$ , the solvent is evaporated using rotavapour, the slightly yellow colored solid raw product, was re-crystallized using 100 ml of (1:1) hexane/ethanol mixture.

Yield: 3.26 g

$^1\text{H-N.M.R}$  ( $\text{CDCl}_3$ ):

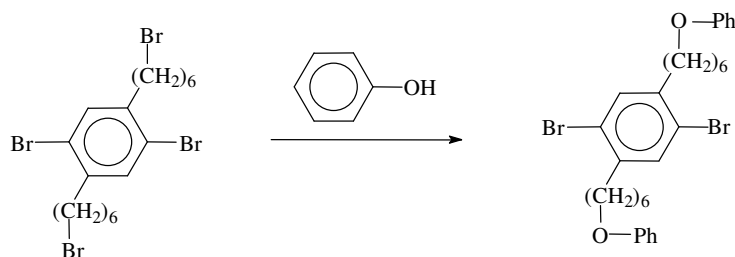
$\delta = 1.39; 1.49; 1.60; 1.88; (4\text{m}, 16\text{H}, \text{Aryl-CH}_2\text{-(CH}_2\text{)}_4); 2.65(\text{ t}, 4\text{H}, \text{Aryl-CH}_2); 3.41(\text{ t}, 4\text{H}, \text{CH}_2\text{-Br}); 7.35(\text{ s}, 4\text{H}, \text{H-Aryl})$

$^{13}\text{C-N.M.R}$  ( $\text{CDCl}_3$ ):

$\delta = 27.89; 28.39; 29.57; 32.64; 33.89; 35.36 (6\text{t}, \text{CH}_2); 123.05 (\text{s}, \text{C}_1); 133.83(\text{s}, \text{C}_3); 141.12(\text{s}, \text{C}_2)$

### 1,4-dibromo-2,5-bis(6-phenoxyhexyl)benzene:

(Rau 1993)



2.18 g of phenol and 1.97 g of sodium-*t*-butylate was dissolved in 80 ml DMF, and after refluxing for 3 hours, in a three neck 1-L round bottom flask equipped with reflux condenser and addition funnel under nitrogen, a solution of sodium phenolate is formed, to this clear solution, 3.26 g 1,4-dibromo-2,5-bis(6-bromohexyl)benzene in 20 ml. toluene and 15 mg. potassium iodide was added, and the reaction mixture refluxed overnight for 24 hours. After cooling the reaction mixture, the resulting solid NaBr was dissolved by addition of 100 ml of water. The water phase was extracted with 4\*75 ml toluene, the residual phenol in the organic phase was neutralized with 3\*50 ml 2N NaOH and washed with 3\*100 ml water.

The organic phase was dried overnight over  $\text{MgSO}_4$ , the solvent was evaporated over rota vapor, and the residual solid was re-crystallized using 75 ml hexane. The solid obtained was then further purified again using column chromatography over silica gel, using toluene as mobile phase, and re-crystallized further using 75 ml of hexane to obtain pure, white crystals.

Yield: 3.0 g

$^1\text{H-N.M.R}$  ( $\text{CDCl}_3$ ):

$\delta = 1.46; 1.51; 1.62; 1.80; (4\text{m}, 16\text{H}, \text{Aryl-CH}_2\text{-(CH}_2\text{)}_4); 2.65(\text{ t}, 4\text{H}, \text{Aryl-CH}_2); 3.96(\text{ t}, 4\text{H}, \text{CH}_2\text{-Br}); 6.90(\text{ m}, 6\text{H}, \text{H}_8, \text{H}_{10}); 7.26(\text{m}, 4\text{H}, \text{H}_9); 7.35(\text{s}, 2\text{H}, \text{H}_3)$

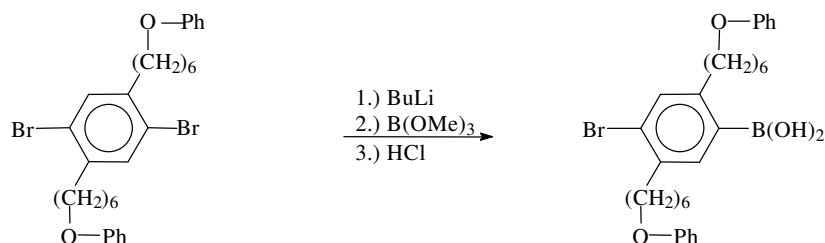


$^{13}\text{C}$ -N.M.R ( $\text{CDCl}_3$ ):

$\delta = 25.85; 29.04; 29.17; 29.72; 35.43; (5t, \text{CH}_2); 67.71 (t, \text{CH}_2\text{-O}); 114.46 (s, \text{C}_8); 120.43 (d, \text{C}_{10}); 123.04 (d, \text{C}_1); 129.47(d, \text{C}_9); 133.82(d, \text{C}_3); 141.18 (s, \text{C}_2); 159.04 (s, \text{C}_7)$

#### 4-bromo-2,5-bis(6-phenoxyhexyl)benzeneboronic acid:

(Rehahn 1994)



A three neck 1-L flask fitted with a reflux condenser, addition funnel, under inert atmosphere, 3.0g 1,4-dibromo-2,5-bis(6-phenoxyhexyl)benzene in 100 ml diethylether und 100 ml toluene was taken, and cooled to  $-55\text{ }^\circ\text{C}$  using a acetone/dry ice mixture. To this white suspension, 2.65 ml of 2,5 molar n-butyllithium-solution in hexane is added using addition funnel. The reaction mixture was then stirred, at around  $-10\text{ }^\circ\text{C}$  a homogenous a yellow solution resulted, this reaction mixture was further stirred at room temperature for 30 min. This reaction mixture was again cooled to  $-60\text{ }^\circ\text{C}$  using acetone/dry ice mixture, to this cooled solution 2.046 ml trimethylborate was added using a syringe, the resulting suspension was stirred at room temperature for 8 hours.

This suspension was hydrolyzed with 100 ml 2N HCl solution, and the resultant two phase reaction mixture was stirred overnight at room temperature. The organic phase was separated and the aqueous phase extracted with 3\*50 ml toluene. The complete organic phase washed with 2\*100 ml water and dried over anhydrous  $\text{MgSO}_4$ . After the evaporation of solvent, the yellowish oil was taken in a mixture of 1:4 toluene/hexane mixture, this solution is taken in a separating funnel and shaken with 100 ml 2N. HCl solution, until the resulting white solid precipitate does not stick to the inner walls of the separation funnel. The white solid precipitate was filtered, washed with water, dried overnight over  $\text{P}_2\text{O}_5$ . The raw product was dissolved in 100 ml warm toluene, and purified using column chromatography over silica gel, after passing approximately 6 liters of toluene, the compound is eluted using 3 liters of t-

butylmethylether. After evaporation of the solvent, the resultant colorless oil, was taken in 1:4 toluene/hexane mixture, and further shaken in a separating funnel with 100 ml 2N HCl solution. The resulting white solid is then filtered, washed with water and dried overnight under vacuum over  $P_2O_5$ .

Yield: 2.46 g

$^1H$ -N.M.R (DMSO):

$\delta$ = 1.34; 1.42; 1.54; 1.71; ( 4m, 16H, Aryl- $CH_2$ -( $CH_2$ )<sub>4</sub>); 2.63, 2.69 ( 2t, 4H, Aryl- $CH_2$ ); 3.90, 3.92( t, 4H,  $CH_2$ -O); 6.90 ( m, 6H,  $H_8$ ,  $H_{10}$ ); 7.27(m, 4H,  $H_9$ ) ; 7.30, 7.33 (2s, 2H,  $H_3$ ,  $H_6$ ); 3.35, 8.10 (2s, 2H,  $B(OH)_2$ )

## 7.2 Polymerization

### 7.2.1 Synthesis of Polymer Precursor

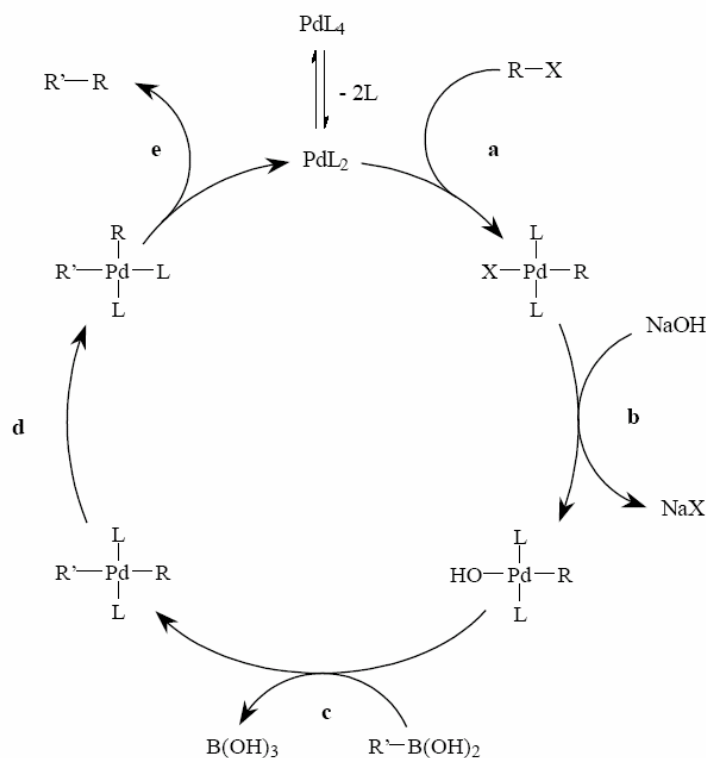


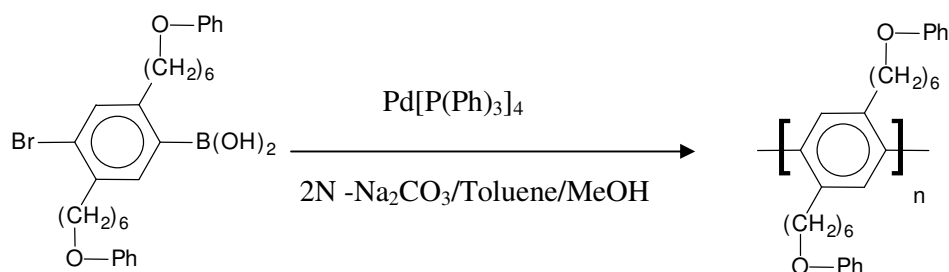
Fig 7.1 shows the catalytic cycle of the palladium catalyst used for the synthesis of stiff-chain polyelectrolytes [Blaul 2000].

The reaction follows the catalysis cycle of Suzuki-Coupling [Suzuki 1985,1986; Aliprantis, Canary 1994]. Tetrakis(triphenylphosphine)-palladium(0)  $Pd(PPh_3)_4$  forms active species

$\text{Pd}(\text{PPh}_3)_2$  by elimination of two phosphine-ligands followed by oxidative addition of aryl halide, palladium is oxidised from  $\text{Pd}(0)$  to  $\text{Pd}(\text{II})$ , which is followed by a ligand exchange. The next step involves the trans-metallation of the boron group by palladium in presence of the base and subsequent release of boronic acid, which is followed by a cis-trans isomerisation and subsequent reductive elimination to couple the C-C bond and to regenerate the catalyst [Aliprantis, Canary 1994].

**poly(2,5-bis(6-phenoxyhexyl)-1,4-phenylene):**

(Rau, Rehahn 1994)



In a two necked round bottom flask, equipped with a reflux condenser, evacuated several times and flushed with argon and kept under argon pressure, 1.0 g 4-bromo-2,5-bis(6-phenoxyhexyl)-benzylboronicacid, 50 ml Toluene, 100 ml. 2N  $\text{Na}_2\text{CO}_3$ -solution, and 5 ml of methanol was added in the reaction vessel, the resultant suspension was further evacuated and flushed with argon several times. 9.0 mg of  $\text{Pd}[\text{P}(\text{Ph})_3]_4$  catalyst, weighed and handled in specially ordered glove bag under argon atmosphere, was added to the reaction mixture and refluxed for 5 days. 2 ml. of bromobenzene was added and the reaction mixture was refluxed further for two days. After cooling, the polymer was precipitated from the reaction mixture by dropping the reaction mixture into 1.5 liters of methanol. The resulting solid was filtered, and washed with 2N HCl to neutralize the sodium carbonate, washed several times with water and dried overnight under vacuum over  $\text{P}_2\text{O}_5$ . The solid polymer was extracted overnight with toluene using Soxhlett-Apparatus. The solvent is then evaporated and re-precipitated using 1.5 liters Methanol. The solid polymer was then filtered, dried under vacuum over  $\text{P}_2\text{O}_5$ . The polymer was further dissolved in minimum quantity of benzene and freeze dried.

Yield: 0.61 g

$^1\text{H-N.M.R}$  ( $\text{CDCl}_3$ ):

$\delta =$  1.36; 1.55; 1.69; ( 4m, 16H, Aryl- $\text{CH}_2$ -( $\text{CH}_2$ ) $_4$ ); 2.46 ( m, 4H, Aryl- $\text{CH}_2$ ); 3.83,( t, 4H,  $\text{CH}_2$ -O); 6.81, 6.87 ( m, 6H,  $\text{H}_8$ ,  $\text{H}_{10}$ ); 7.27(m, 4H,  $\text{H}_9$ ) ; 7.20, (m, 6H,  $\text{H}_3$ ,  $\text{H}_9$ )

## 7.2.2 Characterisation of the Precursor

All the steps in the monomer and precursor synthesis are followed by NMR-spectroscopy to check the purity. The molecular weight and the degree of polymerization was determined using Viscometry [Brodowski et al. 1996; Brodowski 1999]

## 7.3 Polyelectrolyte Synthesis

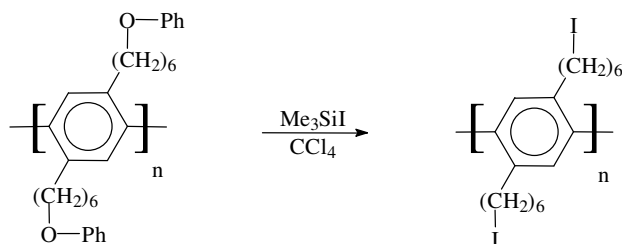
The polymer was then converted into polyelectrolyte after characterization of the uncharged precursor according to the following synthetic procedure:

### 7.3.1 Deprotection of the Ether Groups

The regio selective elimination of the phenoxy group on the side chain was carried out using trimethylsilyliodide under mild conditions. [Ho, Olah 1977; Jung 1977, Lyster 1977; Olah, Narang 1982]. The phenoxyhexyl precursor was refluxed with in carbon tetrachloride for 8 days, to form the iodohexyl derivative. After 5 days 2.5 equivalents of trimethylsilyliodide was further added. The reaction mixture was precipitated in methanol.

#### poly(2,5-bis(6-iodohexyl)-1,4-phenylene):

(Rehahn 1994)



In a two necked round bottomed flask, equipped with a reflux condenser and evacuated several times and flushed with nitrogen and kept under nitrogen over pressure, was added 1.0 g poly(2,5-bis(6-phenoxyhexyl)-1,4-phenylene) in 40 ml tetrachlorocarbon and 6.35 ml of trimethylsilyliodide was added to it. The reaction mixture was refluxed for 5 days, 3.0 ml of

trimethylsilyliodide was further added the reaction mixture was refluxed for 2 days. The reaction mixture was cooled and reprecipitated in 1.5 liters methanol. The precipitated polymer was filtered, washed several times with methanol and dried overnight under vacuum over  $P_2O_5$ .

Yield : 0.98 g

$^1H$ -N.M.R ( $CDCl_3$ ):

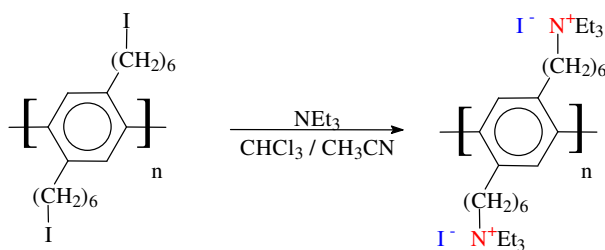
$\delta = 1.34$ ; (m, 8H, Aryl- $CH_2$ -( $CH_2$ )<sub>4</sub>); 1.55 (m, 4H, Aryl- $CH_2$ - $CH_2$ ); 1.78, (m, 4H,  $CH_2$ - $CH_2$ -I); 2.47 (m, 4H, Aryl- $CH_2$ ); 3.17 (m, 4H,  $CH_2$ -I); 7.15 (s, 2H, Aryl-H)

### 7.3.2 Synthesis of Polyelectrolyte

This reaction converts the unpolar precursor into a highly polar product. The iodo-hexyl-derivative is dissolved in a solvent mixture of chloroform and acetonitrile, to which excess amount of triethylamine is added in order to quaternize the iodo group on the side chain. Acetonitrile is added every two hours to dissolve the product formed. The reaction is followed using  $^{13}C$ -NMR-Spectroscopy. The solvent is then evaporated and the raw product was dissolved in warm water. The solution was then filtered and ultra filtered with Millipore water to remove the oligomers using regenerated cellulose with a cut-off 1000 Dalton. The polyelectrolyte was then freeze-dried and stored.

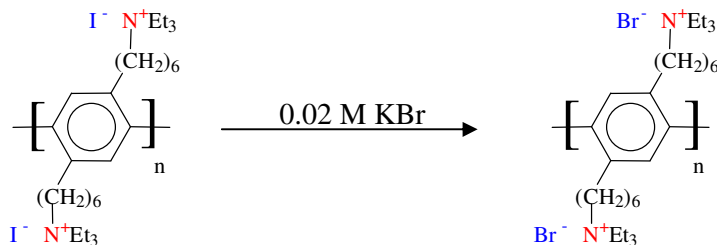
**poly(2,5-bis(6-triethylammoniumiodide)hexyl-1,4-phenylene):**

(Brodowski 1996)



In a two necked round bottomed flask, equipped with a reflux condenser and evacuated several times and flushed with nitrogen and kept under nitrogen over pressure, to this was added 0.98 g of poly(2,5-bis(6-iodohexyl)-1,4-phenylene) in 50 ml chloroform, after addition of 15 ml of acetonitrile and 16.45 ml of triethylamine the reaction mixture was refluxed, approximately after 4 hours of refluxing, a blackish precipitate appears, which was dissolved by further addition of 25 ml portion of acetonitrile to dissolve the precipitate and further refluxed for 24 hours. After cooling the reaction mixture, the solvent was evaporated using a rota vapour and the residual solid dissolved in 100 ml of warm, bidistilled water. The undissolved residue was centrifuged and separated from the ensuing polyelectrolyte solution. The solution was then purified using ultra filtration technique using (NMWL 30,000 regenerated cellulose) with bidistilled water at 1 bar, until the conductivity of the serum dropped under  $1 \mu\text{S}/\text{cm}$ , concentrated, freeze-dried and stored under inert atmosphere.

**poly(2,5-bis(6-triethylammoniumbromo)hexyl-1,4-phenylene):**



The polyelectrolyte PPP2Br was prepared from the polyelectrolyte PPP2I as described elsewhere [Witte mann 2000]. 0.35 g of PPP2I was dissolved in approximately 25 ml of bidistilled water and placed in an ultrafiltration cell (regenerated cellulose 30,000 NMWL), which was then stirred with 4 liters of 0.02 M KBr solution and later cleaned with bidistilled Millipore water until the conductivity of the resulting serum was less than  $1 \mu\text{S}/\text{cm}$ .

### 7.3.3 Sample Preparation for Osmotic Coefficient Measurements

Poly(p-phenylene) polyelectrolyte was synthesized having a degree of polymerization  $P_n=53$  according to procedure described elsewhere. The polyelectrolyte samples prior to use were subjected to extensive ultra filtration. Using a regenerated cellulose filter paper (NMWL 30,000) in a home-manufactured ultra filtration cell under a constant nitrogen pressure of 1 bar. The ultra filtration continued until the conductivity of the outgoing serum dropped to approximately  $1\mu\text{S}/\text{cm}$ . The polyelectrolyte solution was then filtered through a  $0.45\mu\text{m}$  filter, freeze-dried and stored in plastic bottles flushed with argon. Fresh samples were prepared prior to measurements using Millipore Water, conductivity of which was  $0.9\text{--}1.0\mu\text{S}/\text{cm}$ .

The temperature of the osmometer was set at 25 degrees Celsius. Degassed water obtained by heating water at 50 degrees Celsius for approximately 1 hour was then poured into the opened lower half of the measuring cell up to approximately 5 mm below the upper rim. The cell was cleaned several times using the cleaning solution supplied and then washed several times with Millipore water.

Prior to the measurements, the cell was filled several times with water until a constant baseline can be recorded on the plotter, to ensure the stability of zero baseline. After fixing the baseline approx.  $500\mu\text{l}$  of polyelectrolyte solution is introduced into the upper cell. By slowly releasing the pressure valve, the polyelectrolyte solution was introduced inside the measuring cell. This procedure was repeated about 2-3 times until a constant pressure reading can be recorded on the plotter. The stable pressure reading was then recorded and the measuring cell cleaned with water until a stable zero baseline was obtained again before proceeding for further measurements.

## 7.4 Synthesis of Spherical Polyelectrolyte Brushes

The method to synthesize spherical polyelectrolyte brushes used in this study was devised by Xuhong Guo [Guo 2001].

The synthesis of these spherical polyelectrolyte brush systems proceeds in three steps: In the first step, narrowly distributed poly-styrene core latex is synthesized by emulsion polymerization. In the second step a thin layer of photo initiator, in most cases 2-[p-(2-hydroxy-2-methylpropiophenone)]-ethylene glycol-methacrylate (HMEM) is generated on the surface of the polystyrene core. In the final step, water-soluble monomers (as eg. acrylic acid, sodium-styrene sulfonate), are polymerized onto the core by radiation of ultraviolet light to produce a shell of polyelectrolyte chains on the surface of the polystyrene core.

In spite of the turbidity of the system, the reaction proceeds largely due to the elastic light scattering in the latex system which allows the light not absorbed by the photo initiator to scatter and to reach other particles and initiate subsequent polymerization [Guo et al. 2001].

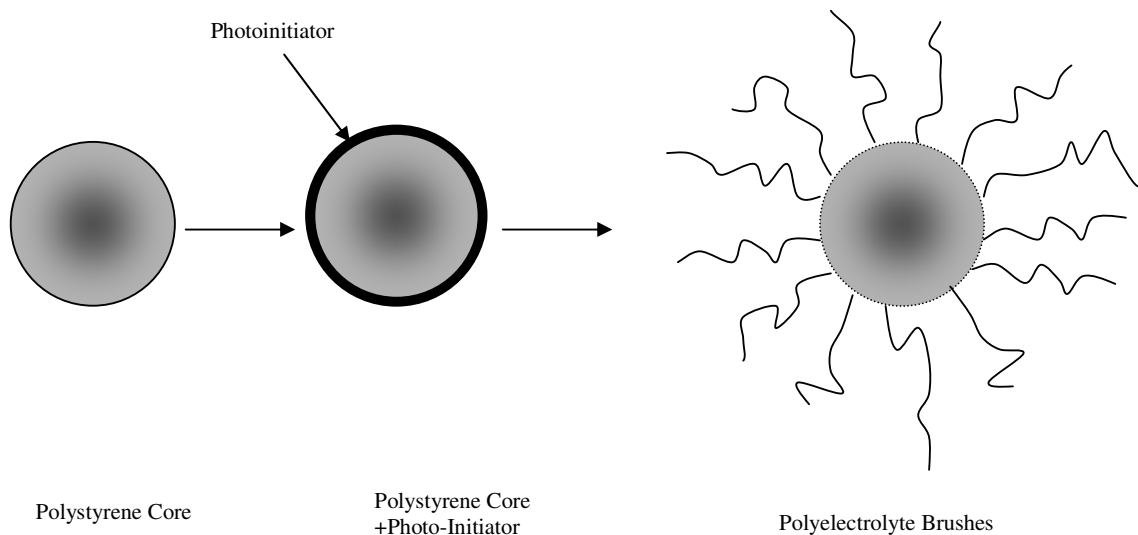


*Fig. 7.2 shows the schematic representation of the synthesis of colloidal polyelectrolyte brushes. In the first step the polystyrene core is synthesized, followed by attaching a thin layer of photoinitiation and subsequent photo-initiated emulsion polymerization.*



## 7.5 Synthesis of Star Polyelectrolytes

The star-shaped polyelectrolytes were synthesized and kindly provided by Mr. Felix Plamper (MC II, University of Bayreuth). The core-first technique was employed for the synthesis of the star polymers. The synthetic route described in literature [Haddleton et al. 1999] was slightly modified for the Initiator synthesis with 5, 8 or 21 arms by using Glucose, Sucrose or  $\beta$ -Cyclodextrins. The initiator is generated by the esterification of the respective molecule by treating with 2-Bromo-2-methylpropanoylbromide with pyridine as base. The star polymers were then synthesized by ATRP process with tert-butyl acrylate in the presence of CuBr and PMDETA as a ligand at 60°C in 10% decane. The conversion of the uncharged polymer to a polyacid follows by subsequent acidic elimination of isobutylene in strictly anhydrous conditions with trifluoroacetic acid and dichloromethane is used as a solvent to form the corresponding acrylic acid. For the scattering experiments, the star polymers with polyacrylic acid chains were then titrated with RbOH solution to generate the polyelectrolyte with Rubidium counterions, as in the case of spherical polyelectrolyte brushes.

## **8 Experimental Section**

### **8.1 Membrane Osmometer**

The osmotic coefficient measurements were carried out using the Gonotec membrane osmometer OSMOMAT 090, which is suitable for measurements with aqueous and organic solvents. The stainless steel cell is thermostatted and is separated in two parts by a semi-permeable membrane. The upper open half of the measurement cell is filled with the polymer solution to be measured and the lower half of the cell which is closed to the outer side is filled with the solvent (water) which gives the negative osmotic pressure corresponding to the osmolal concentration of the solution. A stainless steel membrane fitted to the lower half of the measurements cell becomes slightly curved by this automatically adjusting negative pressure and this movement is registered by an electronic pressure measuring system and is converted into an electrical signal. The concentration of the solution to be measured should be between 0.2 and 2g/100 ml of solvent. The osmotic cell can be thermostatted for temperature within the range of 5 degrees Celsius above the ambient temperature and 130 degree Celsius can be set in intervals of 1 degree Celsius.

### **8.2 Calibration of Osmometer**

The membrane osmometer is calibrated with the help of a special device based on the principle of the hydrostatic pressure difference of the used solvent (in this case water). In first instant the device is placed above the osmometer, this results in a hydrostatic pressure over the water column. The differential hydrostatic pressure acts through the semi-permeable membrane to affect the pressure measuring system in the lower half of the cell, which is about 15 cm of the water column. After the stabilization of the pressure the zero point of the apparatus was adjusted. After controlling the base line stability on the recorder, the bottle is then placed on the table plate. The osmometer is then reset, which then displays the pressure value which is approximately 1.500 (1digit=0.1mm height of the column).

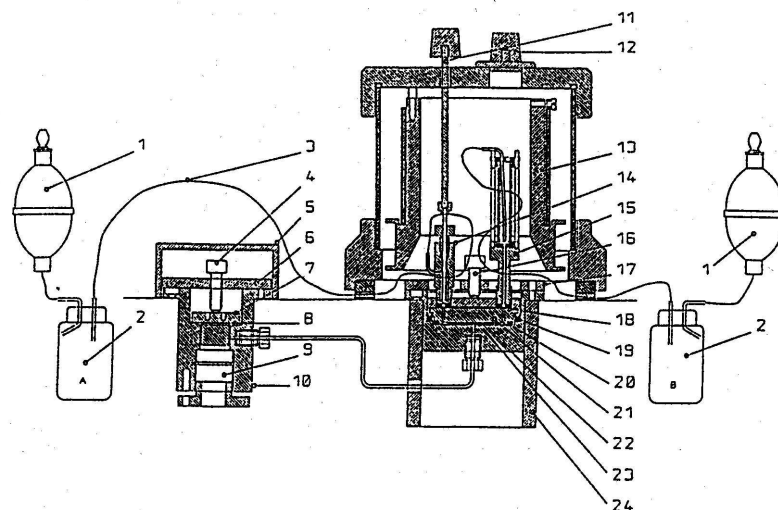


Fig. 8.1 shows a schematic representation of the membrane osmometer Gonotec Osmomat-090B 1. Suction bulb, 2. Suction bottles, 3. Teflon tubes, 4. Compression screw, 5. Cover of the pressure measuring system (pms), 7. Lid of the “pms”, 8. Seal of the “pms”, 9. Pressure transducer, 10. Stainless steel chamber (pms), 11. Extension bar for the valve, 12. Lid, 13. Thermostatted head, 14. Outlet valve, 15. Inlet funnel, 16. Compression screw, 17. compression disk (measuring cell), 18. Universal seal, 19. Large Teflon seal, 20. Small Teflon seal, 21. Upper half of the cell with the meandering channel system, 22. Lower half of the measuring cell, 23. Semi-permeable membrane, 24. Cell thermostat.

### 8.3 Density Measurements

The density measurements were carried out using a densitometer coupled with a digital analyser DMA60 and an external measurement cell DMA 602 (Anton Paar AG, Graz, Austria). The densities obtained were then used to calculate the partial specific volumes of the polyelectrolyte solutions.

## 8.4 Anomalous Small Angle X-ray Scattering (ASAXS)

### ID02/ESRF/Grenoble

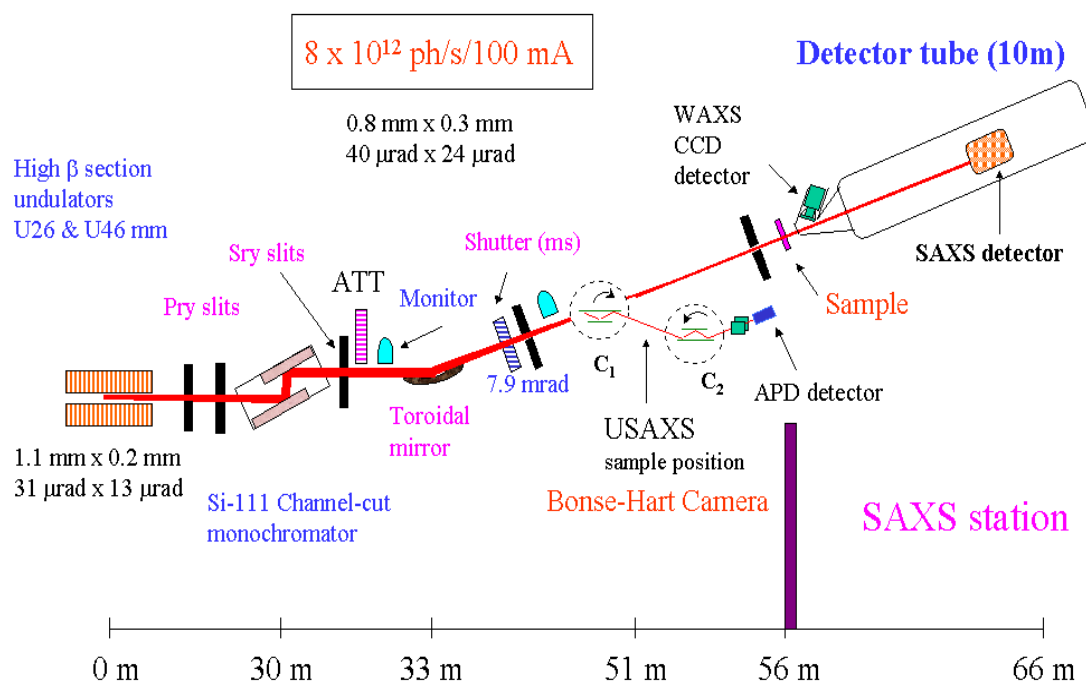


Fig. 8.2 Schematic Representation of ID02 beamline at ESRF, Grenoble France

The ID02 beamline at European Synchrotron Radiation Facility (ESRF) at Grenoble France, was used to carry out Anomalous small-angle X-ray scattering experiments. The optics of the beamline are optimized for experiments using a fixed wavelength around 0.1 nm (12.4 keV), but a wavelength range between 0.073 nm and 0.155 nm is accessible (8-17 KeV), which is necessary to carry out ASAXS experiments. A cryogenically cooled monolithic Si(111) double-crystal is used as a monochromator. A closed liquid-nitrogen loop provides automatic operation of the cooling system. To reduce background radiation from the storage ring, beam is vertically displaced by 30 mm. The Si (111) crystal can select energies between  $\lambda = 0.155$  nm and  $\lambda = 0.073$  nm. (8-17 KeV), and the bandwidth is of the order of  $\Delta E/E = 2 \cdot 10^{-4}$ . An uncooled Rh-coated double-focusing toroidal mirror follows the monochromator. The mirror has a fixed shape and can only be used with wavelengths longer than 0.073 nm. The design of the beamline includes the possibility of installing a horizontally reflecting mirror. In both

directions the maximum reflection angles are 12 mrad. Because of the small beam-divergence the focusing parameters can be kept fixed for all experiments. The mirror characteristics were chosen to minimize the beam size at the detector position when it is moved to the end of the SAXS station (65m). The small-angle scattering camera consists of three slits, two collimation slits, one after the mirror at 34 m in the optical hutch and the other at 50 m in the experimental hutch. Two guard slits in the experimental hutch are located at 52m and directly before the sample at 54 m in the experimental hutch. Usually the slit apertures are set to twice the full width at half maximum ( $2 \times \text{FWHM}$ ) of the focused monochromatic beam. The slits confine the region around the primary beam in which diffuse parasitic scattering from the optics is visible. This defines the minimum size of the beamstop and the minimum observable scattering angle. The sample position is fixed and the detector can be moved from 0.75m to 10m from the sample. The main SAXS detector is an image intensified FRELON CCD system. This detector can acquire up to 10 images / sec of size 1024 x 1024 pixels with 14 bit dynamic range. The full resolution of the CCD is 2048 x 2048 corresponding to an effective pixel size  $\sim 84 \mu\text{m}$ . The photon flux is monitored before and after the sample with silicon PIN diodes. In the standard setup, the transmitted intensity is measured by a PIN diode embedded in the beamstop.

Source: (<http://www.esrf.fr/UsersAndScience/Experiments/SCMatter/ID02/>)



## Patents and Publications

### Patents:

- Cold Water Soluble Tea, Ganesan, V.; Patel, M.; Garg, K.; Subramanian, N.; Ganguli, S.; Sinkar, V.; U.S. Pat. Nr. US6589575; Equivalents: WO0170038; U.S. Pat. Appl. Nr. US2001033880; U.S. Pat. Appl. Nr. US2003203071; Aus. Pat. Appl. Nr. AU5216701; Eur. Pat. Appl. Nr. EP1265492; Can. Pat. Appl. Nr. CA2403396

### Publications:

- Synthesis, Characterization and Aqueous Solution Behaviour of Star-shaped Poly(acrylic acid), Plamper, F.; Becker, H.; Lanzendoerfer, M.; Patel, M.; Wittemann, A.; Ballauff, M.; Mueller, A H.E., *Macromolecular Chemistry and Physics*, Accepted, 2005
- Analysis of the Correlation of Counterions to Macroions by Anomalous Small Angle Scattering, Ballauff, M.; Patel, M.; Rosenfeldt, S.; Dingenouts, N.; Narayanan, T.; Müller, AHE.; Plamper, F., *Polymeric Materials: Science & Engineering*, (93), in Press, 2005
- Analysis of the Correlation of Counterions to Rod-like Macroions by Anomalous Small-Angle X-ray Scattering, Patel, M.; Rosenfeldt, S.; Ballauff, M.; Dingenouts, N.; Pontoni, D.; Narayanan, T. *Phys. Chem. Chem. Phys.*, 2004, (6), 2962
- Counterion Distribution around a Spherical Polyelectrolyte Brush Probed by Anomalous Small-Angle X-Ray Scattering, Dingenouts, N.; Patel, M.; Rosenfeldt, S.; Pontoni, D.; Narayanan, T.; Ballauff, M. *Macromolecules*, 2004, (37), 8152
- Analysis of Spherical Polyelectrolyte Brushes by Anomalous Small-angle X-ray Scattering, Ballauff, M.; Patel, M.; Rosenfeldt, S.; Dingenouts, N.; Pontoni, D.; Narayanan, T. *Polymer Preprints (American Chemical Society, Division of Polymer Chemistry) (2004)*, 45(2), 271





## Lebenslauf

Zur Person		Mushtaq Patel geboren am 06.Januar 1975, Pune, Indien Staatangehörigkeit: Indisch Familiestand: ledig
Schulausbildung	1980-1990	All Saints High School (Pune Divn. Board), Pune, Indien
	1990-1993	Poona College (Pune Divn. Board), Pune, Indien
Studium	1994-1997	Bachelor of Science (Chemistry) Poona College (University of Pune)
	1997-1999	Master of Science (Organic Chemistry) Dept. of Chem (University of Pune)
Berufserfahrung	1999-2000	Research Officer (Unilever Research Centre, Bangalore, Indien)
Promotion	01/01-04/05	Doktorarbeit bei Prof. Dr. M. Ballauff Thema: Counterion Distribution around a Macroion in Polyelectrolytes Probed by Anomalous Small-Angle X-Ray Scattering



## **Erklärung**

Hiermit erkläre ich, dass ich die Arbeit selbständig verfasst und keine anderen als die angegebenen Quellen und Hilfsmittel benutzt habe.

Ferner erkläre ich, dass ich nicht anderweitig mit oder ohne Erfolg versucht habe, eine Dissertation einzureichen oder mich einer Doktorprüfung zu unterziehen.

Bayreuth, den 03. 08. 05

Mushtaq Patel